A Study on Growth Technology of Novel Materials for Absorption Layers of Infrared Sensors by Molecular Beam Epitaxy Method on InP Substrates

A Study on Growth Technology of Novel Materials for Absorption Layers of Infrared Sensors by Molecular Beam Epitaxy Method on InP Substrates

Kohei Miura

February 2013

Doctoral Thesis at Osaka Prefecture University

Table of contents

Chapter 1 Introduction

1.1 Background

1.1.1 Importance of sight

“百聞は一見に如かず(*Hyakubun ha ikken ni shikazu*)” This phrase is a Japanese translation of a sentence which appears in an old Chinese book “*Kanjo*” edited in around 82 A.D. [1] The meaning is “Listening one hundred times is inferior to seeing once.” Today, the phrase is widely known as a proverb in Japan. The fact that such saying has been remained for nearly two thousand years evidences that sight is especially important among the five senses of human beings. It is said that 80% of the stimulus human beings gain is sensed by eyes [2].

How do human beings see? The inside of the eyeball is covered by retina, where many photoreceptors are arranged. Many objects emit light with particular wavelength composition. Light incident on the eye is detected by the photoreceptors. The light is transferred to electric signal by the photoreceptors and sensed as an image by the brain. The wavelength compositions of the light are recognized as the colors of the things. Even objects which do not emit light by themselves reflect light from other light sources, such as the Sun, fire, fluorescent lamps, light emitting diodes, and so on. Moreover, light can penetrate objects with relatively high transparency. The reflected or penetrating light also has peculiar wavelength compositions because of the absorption of the objects. In such cases, the wavelength compositions of the light are also recognized as colors of the objects.

1.1.2 Infrared light

However, information via human eyes is limited because they can sense only light within a restricted wavelength region (380~780nm). Light with longer wavelength is called infrared light, which is invisible. Detecting infrared light is useful in many categories because of the following reasons;

• In infrared region with wavelength between 1 and 10μm, a lot of kinds of materials have absorption band because many chemical bonding such as H-O, C-H, C=O absorb infrared light (Fig. 1.1) [3, 4].

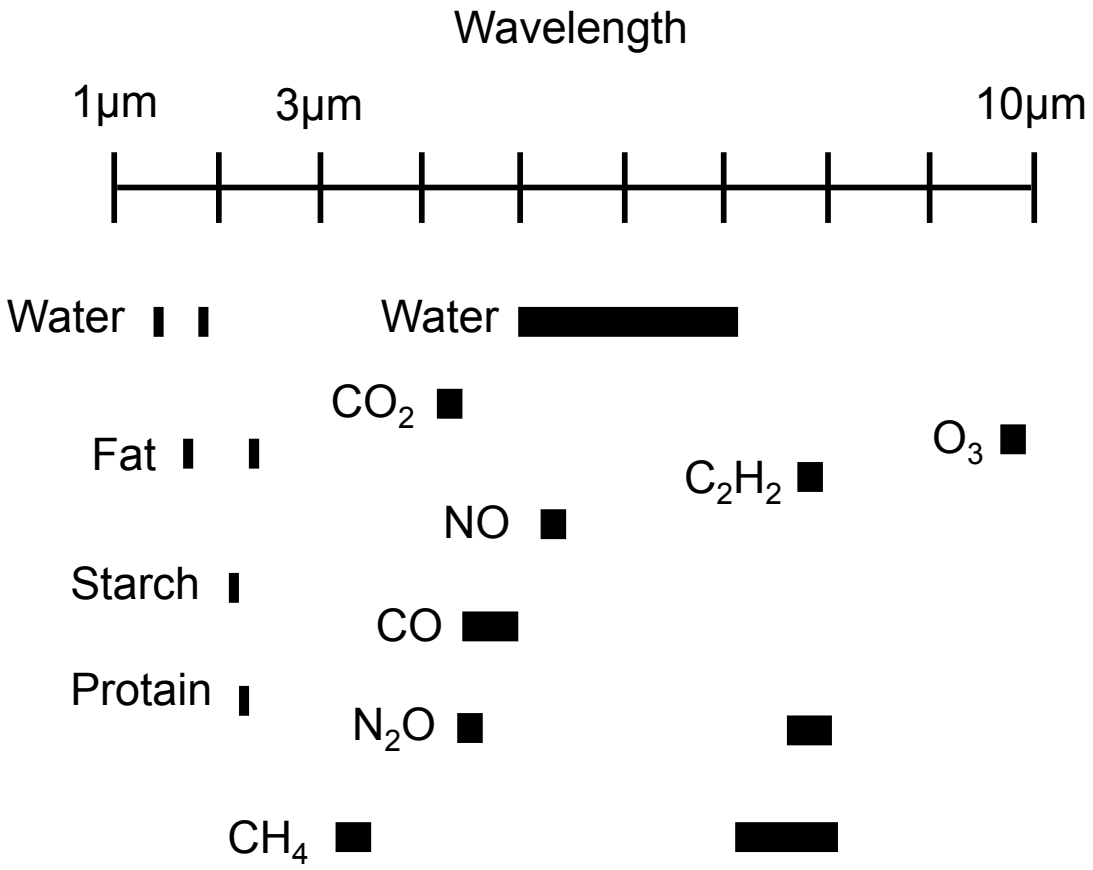

Fig. 1.1 Absorption band in infrared region

These absorptions are derived from the fact that frequency of vibration of electrically polarized bonding (i.e. vibration with electrical dipole moment) coincides that of infrared light [5].

Detecting infrared light can be used for recognizing materials, which human eyes cannot distinguish.

• Detecting infrared light allows to recognizing things in darkness. Objects with heat emit infrared light. Planck discovered that spectrum of light radiated by a black body at absolute temperature T (K) is expressed in the following formula (Plank's law of radiation);

$$M_{e,\lambda}(\lambda) = \frac{c_1 \lambda^{-5}}{\{exp(c_2/\lambda T) - 1\}} \quad (\mathrm{Wcm^{-2}\mu m^{-1}}) \tag{1.1}$$

where

$$c_1 = 2\pi hc^2 = 3.7415 \times 10^5 \quad (\mathrm{Wcm^2})$$

$$c_2 = h\,c/k = 1.4388 \times 10^4 \quad (\mathrm{cmK})$$

(h; Plack constant, c; Speed of light in vacuum, k; Boltzmann constant)

Spectra of black body radiation at several temperatures are shown in Fig. 1.2. Even objects at room temperature radiate infrared light with wavelength of several μm. Detecting infrared light enables us to distinguish invisible objects at different temperature compared to the surrounding (a person in darkness, for example).

In the sense of absorption mechanism, infrared light can be roughly classified in several categories by the wavelength. In the wavelength region shorter than 2.5μm, absorptions are derived from overtones and combination tones of fundamental vibration [6]. On the other hand, fundamental vibrations are dominant in the wavelength region longer than 2.5μm. In this thesis, the wavelength region shorter than 2.5μm and 2.5~10μm are called near infrared (NIR) region and mid-infrared (MIR) region, respectively, although they are not defined formally. The author focused on the two regions.

In the NIR region, the absorption coefficient is not high because it originates from overtones and combination tones of fundamental vibration. In other words, the transparency is high. It can be utilized to non-destructive examination. In the MIR region, the absorption is high because it originates from fundamental vibration. It is suitable for gas detection.

1.2 Infrared sensor

1.2.1 Advantages of infrared sensors

Infrared sensors work in place of human eyes in infrared region. Especially, focal plane arrays

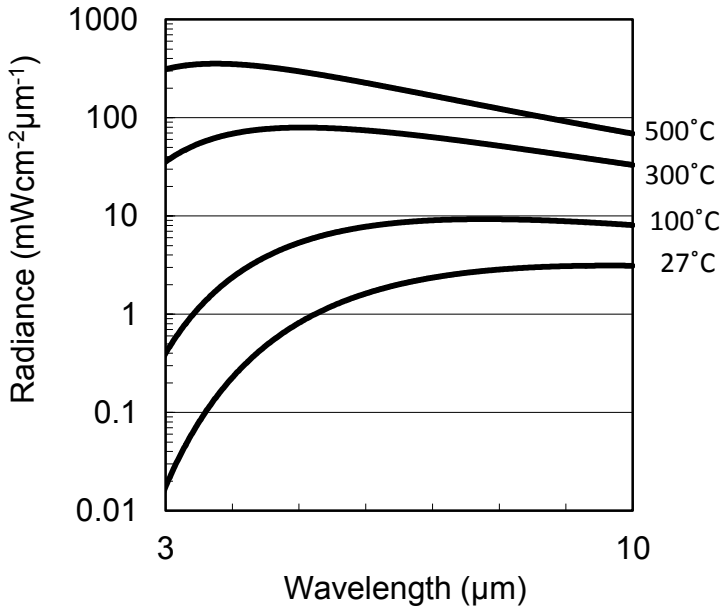

Fig. 1.2 Spectra of black body radiation at several temperatures

(FPAs) are expected to be applied in many ways. Schematic of FPA is shown in Fig. 1.3. It is consisted of a sensor chip and a readout integrated circuit (ROIC). Minute sensors (corresponding to pixels) are arrayed on the sensor chip one- or two-dimensionally. The sensors are isolated with each other by means of such as mesa etching. The ROIC is made of Si. It reads out the electric signals from the sensors. All the sensors are bonded to ROIC by bump made of metal such as In. The sensor chip and the ROIC are packaged in a ceramic case (with a cooling system if necessary). By equipping FPAs in cameras, we can capture infrared images like conventional digital cameras. This sensor enables us to recognize distribution of infrared light easily in real time in a nondestructive and contactless manner [7].

A simple example of FPA usage is described. Both sugar and salt look white powder for human eyes. However, sugar placed in shapes of scripts “SEI” on salt was observed utilizing an infrared imaging system, which is equipped with infrared camera using FPA and infrared light source to capture infrared images (Fig. 1.4) [8]. The reason of this phenomenon is almost the same as that of human beings’ seeing mentioned in 1.1.1. Sugar and salt have extremely different infrared absorption bands. Sugar is composed of sucrose ($C_{12}H_{22}O_{11}$), which contains large amount of chemical bonds absorbing infrared light. On the other hand, salt is known for high transparency in infrared region [9]. The real-time infrared images are shown on a display of a personal computer. In this case, the positions with stronger infrared light appear clearer. Although sugar on salt is not recognized in the image taken by ordinary camera, it is easily recognized as shown in Fig. 1.5. Similar to this way, FPAs are applied or expected to be applied in many categories. Several examples are given below [10-12];

- Process check in chemical plants (e.g. pharmacy)
- Bio-diagnostics
- Food inspection
- Pollution monitoring
- Thermal imaging

However, there are big challenges in infrared sensors as mentioned in 1.2.3. In this study, the author struggled to solve the challenges.

1.2.2 Basic of infrared sensors

There are many kinds of infrared sensors. They are roughly classified in two groups [11, 13]: photon and thermal. The characteristics of the two types are summarized in Table 1.1. In the photon sensor,

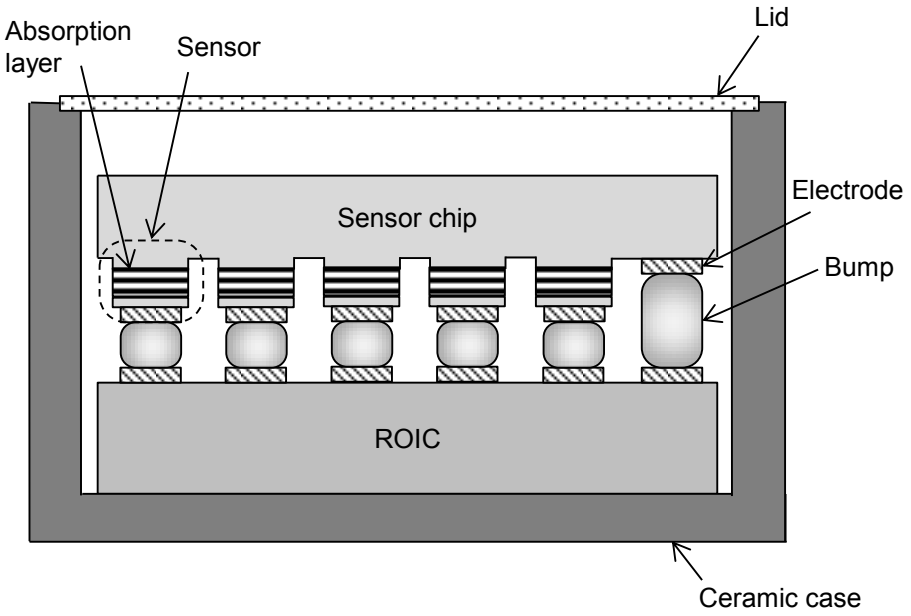

Fig. 1.3 Schematic of an FPA

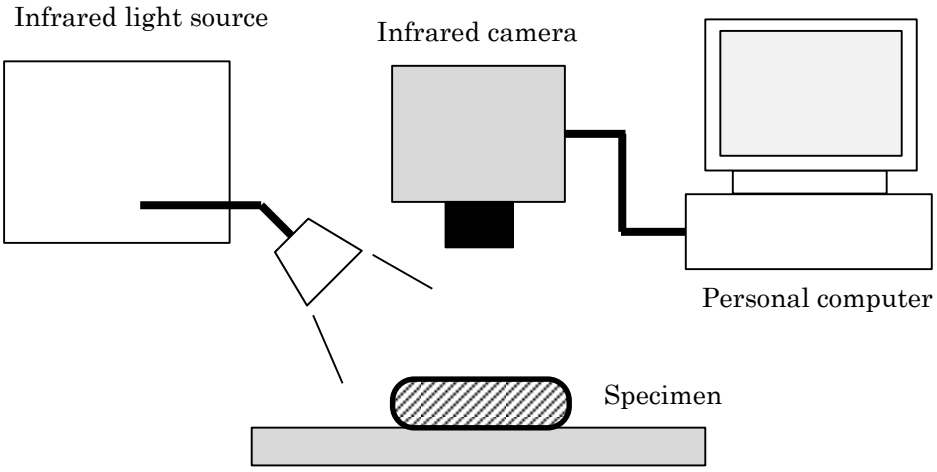

Fig. 1.4 Schematic of infrared imaging system

(a) Image taken by ordinary camera

(b) Image taken by infrared camera

Fig. 1.5 Image of sugar on salt captured by infrared imaging system

Table 1.1 Characteristics of sensors in two groups

	Photon sensor	Thermal sensor
Responsivity	High	Low
Response speed	Fast	Slow
Cooling system	Sometimes necessary	Not necessary
Kinds of sensors	PbS, MCT, InSb	Thermistor, Bolometer, Thermopile, TGS

light is transferred to electric signal. Photons are absorbed and free carriers are generated, which are sensed by an electric readout circuit. On the other hand, the thermal sensor utilizes the change of parameter such as resistivity of dielectric constant. The incoming IR photons are absorbed by a thermally isolated sensor element, resulting in an increase in the temperature of the element, which is sensed by monitoring a parameter. In this study, the author focused on pin-photodiodes (pin-PDs), one of photon sensors because photon sensors exhibit higher sensitivity and faster response speed, and the fabrication technology of pin-PDs with InGaAs absorption layers for optical fiber communication can be applied.

Pin-PDs are photovoltaic sensors. The principle of pin-PDs operation is as follows; An example of structure of pin-PD is illustrated in Fig. 1.6. The buffer layer, the absorption layer and the cap layer are grown on the substrate. In this example, the buffer layer is n-type and the cap layer is p-type. This structure is called p-on-n. In this study, many of the sensors are fabricated using this structure, with some exceptions using n-on-p structure. The absorption layer is not doped, i.e. i-type. The sensor is operated at a certain reverse bias. The band structure of the sensor is shown in Fig 1.7. A depletion region is formed due to low carrier concentration of the absorption layer. The n-type and p-type regions consist of materials with higher band gaps than the absorption layer because absorption by n-type and p-type regions reduces sensor responsivity. Electron-hole pairs are generated in the absorption layer by absorbing photons with higher energy than the band gap of the absorption layer. Due to the inclination of the band of the absorption layer, electrons and holes move toward the n-type region and the p-type region, respectively. The carriers which reach the n-type and p-type regions are sensed by the readout circuit as electric signal.

Important sensor figures of merit are described below;

Cutoff wavelength; Only photons with higher energy than the band gap of the absorption layer are detected. The wavelength of the light is in inverse proportion to photon energy. The longest wavelength of light which the sensor can detect is called cutoff wavelength:

$$\lambda_{\mathrm{cutoff}} = \frac{hc}{E_{\mathrm{g}}} = \frac{1240}{E_{\mathrm{g}}\,(\mathrm{meV})} \quad (\mu\mathrm{m}) \tag{1.2}$$

where E_{g} denotes the band gap of the absorption layer.

Dark current; Sensors with pin structures transfer optical input to electric signal i.e. photocurrent at a certain reverse bias. Therefore, sensors which exhibit no currents with no optical input are ideal. However, real sensors exhibit current due to several reasons (diffusion of carriers, carrier generation via lattice defects, tunneling, and so on) even if no light is input. The current is called dark current.

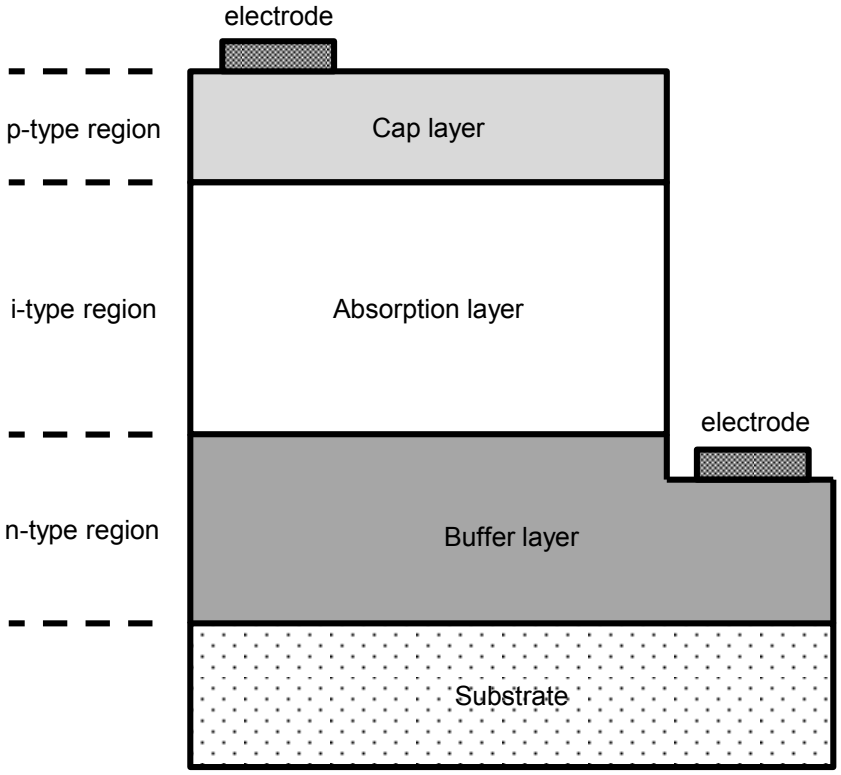

Fig. 1.6 Example of infrared sensor structure

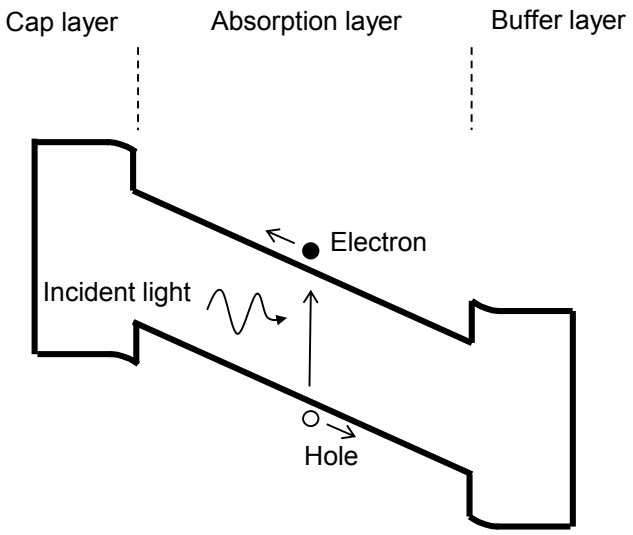

Fig. 1.7 Band structure of infrared sensor

Lowering dark current is important in order to realize high sensitivity.

Quantum efficiency; Quantum efficiency η is the ratio of electron-hole pairs generated and incident photons [14];

$$\eta = \frac{I_{\mathrm{p}} h\nu}{q P_{\mathrm{opt}}} \tag{1.3}$$

where I_{p}, ν, q and P_{opt} denote the photocurrent, frequency of light at a wavelength λ, elementary charge and optical power at a wavelength λ, respectively.

Responsivity; Responsivity R is a ratio of the photocurrent to the optical power [14];

$$R = \frac{I_{\mathrm{p}}}{P_{\mathrm{opt}}} = \frac{\eta q \lambda}{hc} = \frac{\eta \lambda\ (\mu\mathrm{m})}{1.24} \qquad (\mathrm{A/W}) \tag{1.4}$$

Noise equivalent power; Noise equivalent power (NEP) is the incident power on the sensor generating signal output equals to the rms noise output [11];

$$\mathrm{NEP} = \frac{I_{\mathrm{n}}}{R} \qquad (\mathrm{W}) \tag{1.5}$$

NEP stands for the lower limit of incident power which the sensor can detect.

Detectivity; Detectivity D is the reciprocal of NEP [11];

$$D = \frac{1}{\mathrm{NEP}} \qquad (\mathrm{W}^{-1}) \tag{1.6}$$

Both NEP and D depend on the square root of sensor area, A and the bandwidth, Δf. Therefore, normalized detectivity D^* is often used [11];

$$D^* = D(A\Delta f)^{1/2} = \frac{(A\Delta f)^{1/2}}{\mathrm{NEP}} \qquad (\mathrm{cmHz^{0.5}/W}) \tag{1.7}$$

Practical limit of D^* of photovolatic sensor such as pin-PDs can be expressed in the following equation [11, 14];

$$D^* = \frac{c\exp(\zeta/2)}{\sqrt{2\pi kT}\nu^2(1 + 2/\zeta + 2/\zeta^2)^{1/2}} \qquad (\mathrm{cmHz^{0.5}/W}) \tag{1.8}$$

where $\zeta \equiv h\nu/kT$. Dependence of D^* on λ at 300K and 77K is illustrated in Fig. 1.8. In the wavelength region between 1 and 10μm, D^* decreases as λ increases. Therefore, sensors with long cutoff wavelength should be cooled.

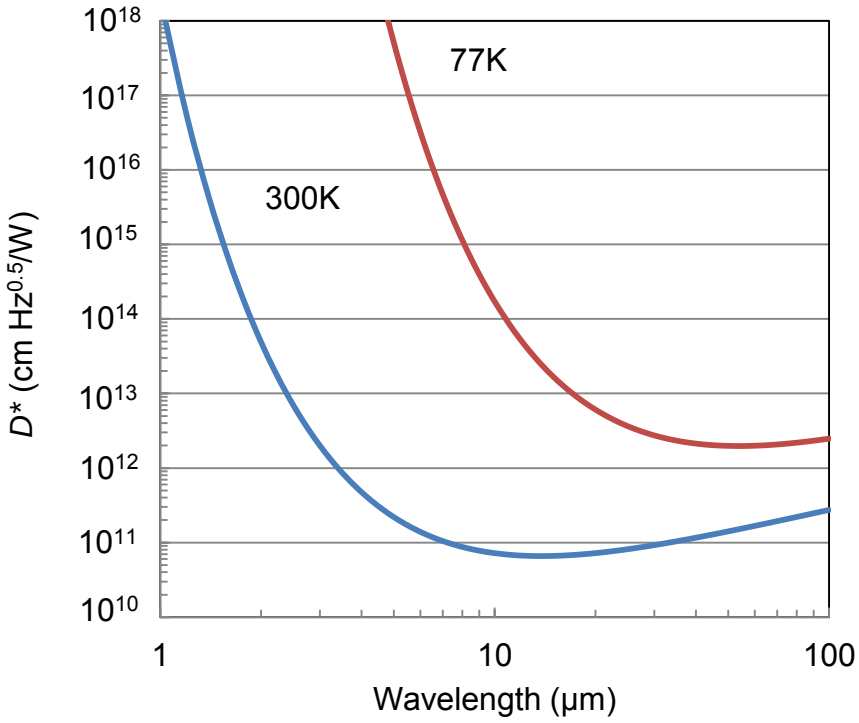

Fig. 1.8 Dependence of limit of normalized detectivity on wavelength

1.2.3 Current infrared sensors

Characteristics of infrared sensors depend of absorption layer materials. In this subsection, details of absorption layer materials used currently are explained.

(1) Si (NIR)

Si is the most important material in semiconductor industries. Today, most of the semiconductor devices are made of Si. However, the use of Si is limited for infrared sensors due to the narrow wavelength region. Cutoff wavelength is as short as 1.1μm at room temperature because the band gap is 1.12eV [14]. Moreover, Si is an indirect band gap semiconductor, which results in low absorption coefficient around cutoff wavelength [15]. Therefore, Si sensors are mainly used to detect visible light.

(2) InGaAs (NIR)

InGaAs is a ternary alloy of GaAs and InAs. The band gap of $In_xGa_{1-x}As$ changes with the In composition x as the following equation;

$$E_{\mathrm{g\_InGaAs}} = xE_{\mathrm{g\_InAs}} + (1-x)E_{\mathrm{g\_GaAs}} - cx(1-x) \tag{1.9}$$

where $E_{\mathrm{g\_InAs}}$, $E_{\mathrm{g\_GaAs}}$ and c are band gap of InAs, band gap of GaAs and bowing parameter (0.477eV for InGaAs), respectively [16]. Therefore, cutoff wavelength can be varied by adjusting In composition. Since infrared sensors with InGaAs absorption layers grown on InP substrates were reported in the 1980s, fabrication technology of infrared sensors with InGaAs absorption layers has been developed rapidly accompanied with explosive prevalence of optical communication. The sensors with $In_{0.53}Ga_{0.47}As$ absorption layers lattice-matched to InP substrates has cutoff wavelength of 1.7μm. They can detect infrared light with wavelength of a 1.3μm and 1.55μm, which can be transmitted with low loss in optical fibers [14].

However, there is a tradeoff between cutoff wavelength and detectivity. Higher In composition result in not only narrower band gap, but also larger lattice constant. It is well-known that the lattice constant of alloy is proportional to the composition (Vegard's law) [17]. The lattice constant of $In_xGa_{1-x}As$ changes with the In composition x as the equation following;

$$a_{\mathrm{InGaAs}} = xa_{\mathrm{InAs}} + (1-x)a_{\mathrm{GaAs}} \tag{1.10}$$

where a_{InAs} and a_{GaAs} denote lattice constants of InAs and GaAs, respectively. The relation between the lattice constant and the band gap of InGaAs is shown in Fig.1.9 [16]. Sensors with InGaAs absorption layers lattice-matched to InP substrates exhibits low dark current because of excellent crystalline quality, but the cutoff wavelength is short. Sensors with cutoff wavelength up to 2.6μm have been fabricated using In-rich lattice-mismatched InGaAs absorption layers. But the

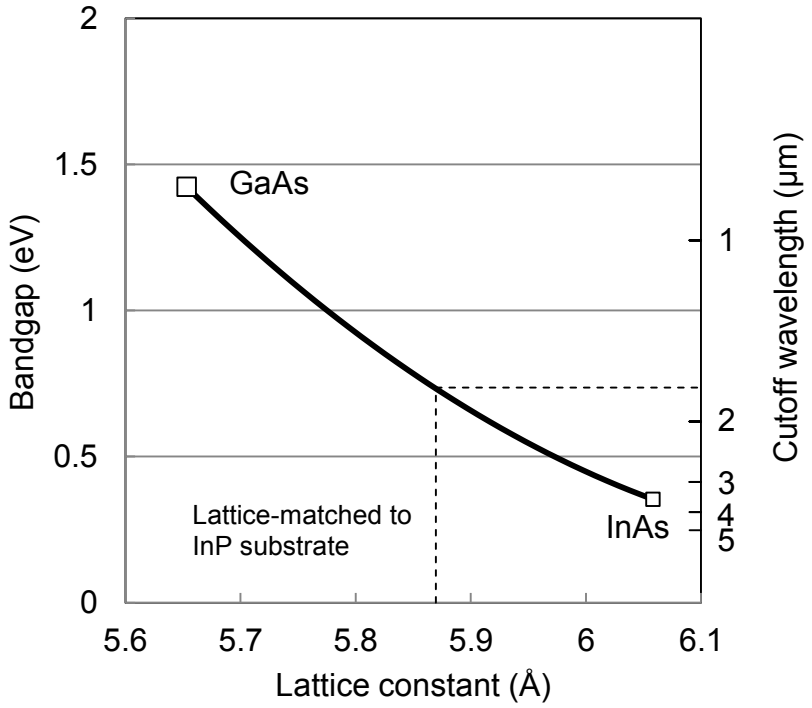

Fig. 1.9 Lattice constant and bandgap of InGaAs

sensors require cooling system which increases power consumption, size, and cost because of high dark currents derived from poor crystalline quality [18].

(3) Mercury-cadmium-tellurium (NIR+MIR)

Mercury-cadmium-tellurium (HgCdTe, MCT) is ternary alloy of HgTe and CdTe, which are II-V compound semiconductors. MCT has been studied since approximately 1970 [19]. Today, MCT is widely used for mainly MIR sensors. The band gap of MCT is reported to be expressed in the following equation [20];

$$E_{\mathrm{g}} = -0.302 + 1.93x - 0.81x^2 + 0.832x^3 + 5.35(1-2x)10^{-4}\left(\frac{-1822 + T^3}{255.2 + T^2}\right) \text{ (eV)} \quad (1.11)$$

where x and T denote Cd composition and temperature, respectively. Dependence of the band gap on Cd composition is plotted in Fig. 1.10 (a). Narrow band gap can be obtained by using low Cd composition.

However, there are big issues for applying to MIR FPAs. The first issue is that control of cutoff wavelength becomes difficult as cutoff wavelength becomes longer. Dependence of the cutoff wavelength on Cd composition is plotted in Fig. 1.10 (b). In order to obtain cutoff wavelength 5±0.5μm, Cd composition must be controlled within 0.289~0.321. But Cd composition must be controlled more accurately within 0.222~0.230 to obtain cutoff wavelength 10±0.5μm. The second issue is involved in substrate for epitaxial growth. CdZnTe substrates, lattice matched to MCT, are used [19]. However, substrates with only small area are available. Although alternate substrates, such as sapphire [21] and Si [22], are studied, the issue of control of cutoff wavelength would remain.

(4) Type-II InAs/GaSb superlattice (MIR)

Type-II InAs/GaSb superlattices (SLs) are attractive materials for alternative material for MCT. By stacking several nm-thick InAs and GaSb alternately, broken band structure as illustrated in Fig. 1.11 is obtained. The bottoms of conduction bands of InAs layers are lower than those of GaSb layers. The values of band gaps and band offsets are based on the report by G. A. Sai-Halasz et al [23]. A miniband of electron is formed between the bottoms of conduction band of InAs and GaSb layers [24]. Similarly, a miniband of hole is formed between the tops of valance band of InAs and GaSb layers [24]. By using such band structure, long cutoff wavelength which InAs or GaSb single layers cannot realize can easily obtained. Recently, this material attracts many researchers because it is promising for alternative to MCT for the following reasons;

• The cutoff wavelength is controlled between 3-30μm by changing thickness of GaSb and InAs layers because the heights of the minibands of electron and hole depend on the thickness of GaSb and InAs

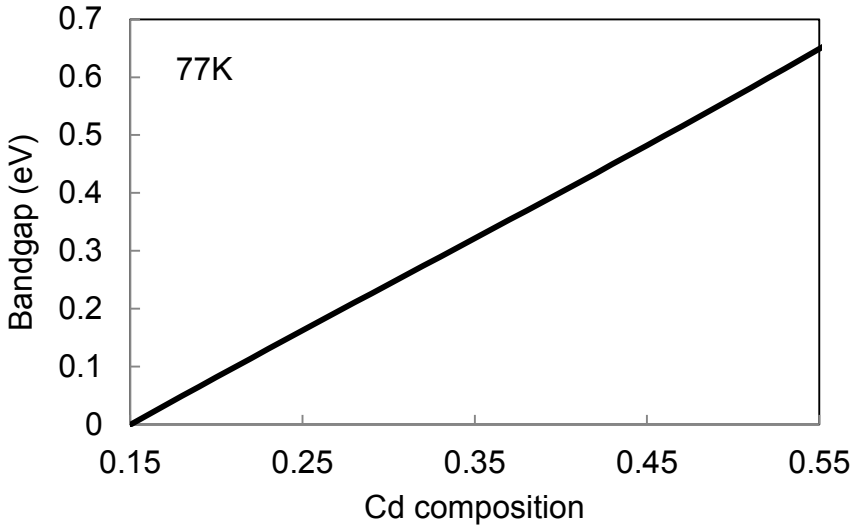

(a) Band gap

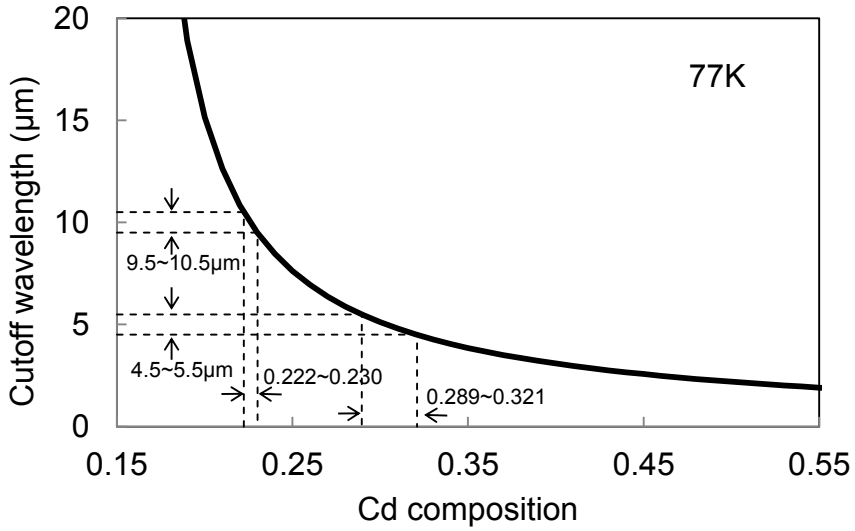

(b) Cutoff wavelength

Fig. 1.10 Dependence of Bandgap and cutoff wavelength of MCT on Cd composition

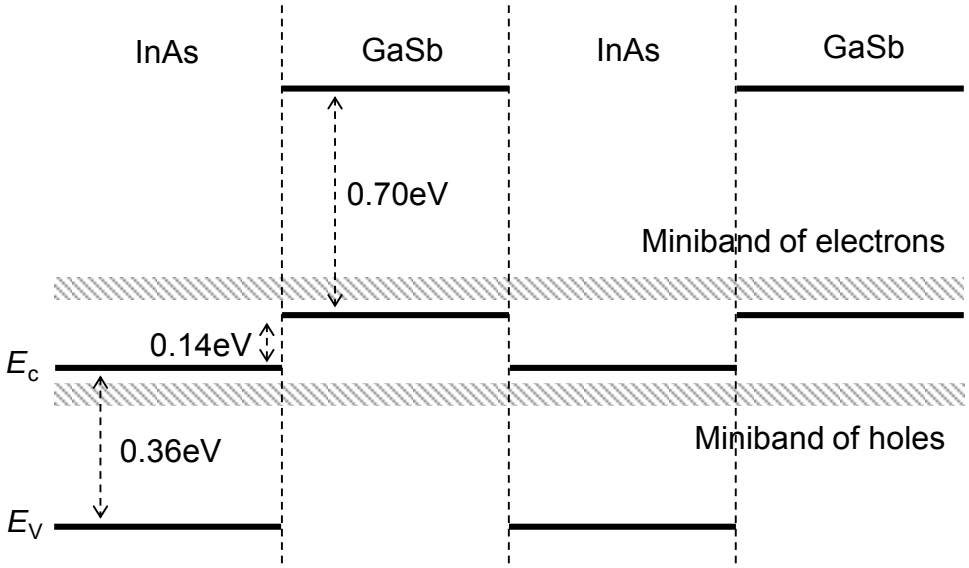

Fig. 1.11 Band structure of type-II InAs/GaSb SL

layers [25]. This characteristic enables us to control the cutoff wavelengths of the sensors with higher in-plane uniformity and reproducibility [26].

• Type-II InAs/GaSb SL is theoretically predicted to realize higher detectivity compared to MCT. This is due to long minority carrier lifetime resulting from suppressed band-to-band Auger recombination rates [27, 28], and relatively large effective masses of carriers [29].

Since M. J. Yang and B. R. Bennett reported sensors with inAs/GaSb SL absorption layers operating at 77K in 1994 [30], many sensors including FPAs have been demonstrated [31-34].

However, there are some problems concerning substrates. GaSb substrates are generally used for the epitaxial growth of this type-II SL because the SL can be grown lattice-matched. Large absorption coefficient in mid-infrared region diminishes the external quantum efficiency of sensors with back-illuminated structures such as FPAs. Although the band gap of GaSb is larger than photon energy of mid-infrared light, free carrier in GaSb seem to absorb the infrared light [35]. GaAs substrates with higher transparency are proposed instead of GaSb substrates [36]. But the epitaxial growth is difficult owing to the large lattice mismatch between GaAs and GaSb (7.8%) [37, 38]. Furthermore, the difference of thermal expansion coefficient between GaSb substrate and ROIC, which are bonded to each other with indium bumps, makes the reliability of bonding poor, because the FPAs are used by cooling down to the temperature lower than 100K [16, 39].

The challenges of NIR and MIR sensors seem to be integrated into the following two facts;

NIR; New materials for absorption layers are necessary to realize both long cutoff wavelength (~2.5μm) and low dark current enough to be used at room temperature.

MIR; Although promising material (type-II InAs/GaSb SL) for absorption layer is proposed, appropriated substrates for epitaxial growth should be searched.

1.3 Novel InP-based NIR and MIR sensors

In order to solve the challenges of NIR and MIR sensors, the author focused on InP-based sensors. InP wafers with larger diameter and lower cost are available than CdZnTe and GaSb. Fabrication

technology of InP-based NIR sensors is developed as mentioned in the last subsection. These merits would be favorable for fabricating FPAs. Moreover, InP-based sensor is expected to have following advantage;

NIR

Two novel materials, lattice-matched to InP substrates and expected to realize cutoff wavelength ~2.5μm, are able to grow on InP substrates. Details of the materials are described below;

• **InGaAsN**; Alloy of III-N and III-As is reported to exhibit narrow band gap due to large bowing parameter [40]. $In_{0.77}Ga_{0.23}As_{0.92}N_{0.08}$ lattice-matched to InP substrate is predicted to realize cutoff wavelength of 2.5μm [41]. InGaAsN quantum wells with PL wavelength longer than 2μm are already reported [40, 42]. However, two challenges should be solved. (I) Thick InGaAsN layers (several μm-thicks) grown on InP substrates are necessary for sensor absorption layers. Although InGaAsN quantum wells are studied for activation layers of laser diodes [43, 44], there are few reports about thick InGaAsN layers on InP substrates. Basic knowledge of thick InGaAsN layers is needed. (II) Narrow band gap corresponding to cutoff wavelength of 2.5μm is required. High N composition, which might be technically difficult, is necessary to realize such band gap.

• **Type-II InGaAs/GaAsSb SL**; GaAsSb is a ternary alloy of GaAs and GaSb. The band gap of $GaAs_{0.511}Sb_{0.489}$, lattice matched to InP substrate, is almost equal to that of lattice-mached InGaAs. However, by stacking several nm-thick lattice-matched InGaAs and GaAsSb alternately, narrower band gap can be realized by the staggered band structure as illustrated in Fig. 1.12 [45]. The author applied the value reported by J. Hu et al for InGaAs/GaAsSb conduction band offset [46]. In this band structure, excited electrons and holes are separated spatially. Electrons and holes localize in InGaAs and GaAsSb, respectively. But the wavefunctions of electron and hole overlap with each other due to penetration into potential barrier, resulting in narrower band gap and longer cutoff wavelength than bulk InGaAs or GaAsSb. Low dark current is also expected because it can be grown lattice-matched. Moreover, even longer cutoff wavelength is theoretically predicted by introducing strain-compensated structure [47]. NIR sensors with type-II InGaAs/GaAsSb SL absorption layers are already reported [47-49]. However, analysis of basic characteristics of GaAsSb for sensors is necessary.

MIR

InP substrates seem to be more favorable for fabrication of FPA with InAs/GaSb SL absorption layers compared to GaSb and GaAs substrates. The author has proved InP:Fe substrates exhibit high

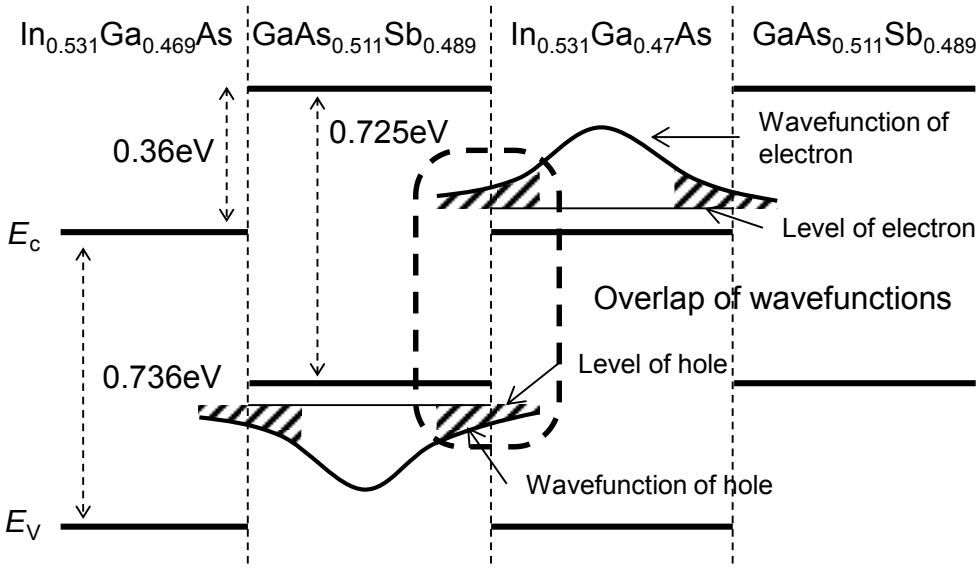

Fig. 1.12 Band structure of type-II InGaAs/GaAsSb SL

transparency in mid-infrared region. The detail is described in Chapter 5. The lattice mismatch between InP and GaSb is smaller than that between GaAs and GaSb as listed in Table 1.2(a) [16]. Moreover, InP has a closer thermal expansion coefficient to that of Si than GaAs and GaSb (Table 1.2(b)) [16, 39]. However, there are no reports about type-II InAs/GaSb SLs grown on InP substrates. Before fabricating sensors, it must be tested whether type-II InAs/GaSb SLs with good crystalline quality can be grown on InP substrates.

Table 1.2 Parameters of GaSb, GaAs and InP

(a) Lattice constant

	Lattice constant (Å)	Lattice mismatch with GaSb
GaSb	6.096	-
GaAs	5.653	7.8%
InP	5.870	3.9%

(b) Thermal expansion coefficient

	Thermal expansion coefficient (10^{-6} K^{-1})
Si	3.34
GaSb	7.74
GaAs	6.86
InP	4.75

1.4 Outline of this thesis

The outline of this thesis is as follows;

• In chapter 2, details of the experiments in this study are described.
• In chapter 3, the study on InGaAsN layers on InP substrates for NIR sensor is described.
• In chapter 4, the study on type-II InGaAs/GaAsSb SLs on InP substrates for NIR sensor is described.
• In chapter 5, the study on type-II InAs/GaSb SLs on InP substrates for MIR sensor is described.
• In chapter 6, this study is concluded.

References

[1] Hanko, *Kanjo* 6 (~82)

[2] N. Ota, *Color Engineering Second Edition* (2001)

[3] *The Aldrich Library of FT-IR Spectra* Vol.1 (1985)

[4] S. Kono, *Handbook of Food Non-destructive Measurement* (2003)

[5] K. Takada, Y. Egawa, H. Sasaki, *Far Infrared Ray*

[6] Y. Ozaki, *Near Infrared Spectroscopy* (1998)

[7] *Brochure of Sumitomo Electric Industries Ltd., Research & Development* (2012)

[8] http://www.sei.co.jp/news/press/09/prs737_s.html

[9] http://www.internationalcrystal.net/ti_sec1.htm

[10] D. A. Burns, E. W. Ciruczak, *Handbook of Near-Infrared Analysis Third Edition* (2007)

[11] A. Rogalski, *Infrared Detectors Second Edition* (2011)

[12] K. K. Choi, *The Physics of Quantum Well Infrared Photodetectors* (1997)

[13] T. Oomori, *Tales of Infrared light*

[14] S. M. Sze, *Physics of Semiconductor Device Second Edition* (1981)

[15] S. Gonda, M. Kawasima, *Electric and Optical Characteristics of Compound Semiconductors, The Newest Handbook of Compound Semiconductors* (1982)

[16] I. Vurgaftman, J. R. Meyer, L. R. Ram-Mohan, J. of Appl. Phys., Vol. 89, 5815 (2001)

[17] H. Nagai, S. Adachi, T. Fukui, *III-V Compound Semiconductor Alloy* (1988)

[18] M.Wada and H.Hosomatsu: Appl. Phys. Lett., Vol. 64, 1265 (1994)

[19] M. Henini, M. Razeghi, *Handbook of Infrared Detector Technologies* (2002)

[20] J. R. Lowney, D. G. Seiler, C. L. Littler, I. T. Yoon, J. Appl. Phys., 71, 1253 (1992)

[21] E.R. Gertner, W.E. Tennant, J.D. Blackwell, J.P. Rode, J. of Cryst. Growth, Vol. 72, 462 (1987)

[22] W. E. Tennant, D. Lee, M, Zandian, E. Piquette, M. Carmody, J. of Electron. Mater., 37 (2008)

[23] G. A. Sai-Halasz, R. Tsu, L. Esaki, Appl. Phys. Lett., Vol. 30, 651 (1977)

[24] C. J. Hill, A. Soibel, S. A. Keo, J. M. Mumolo, S. D. Gunapala, Proc. of SPIE, 6940, 69400C (2008)

[25] S. d. Das, S. L. Tan, S. Zhang, Y. L. Goh, C. H. Tan, J. David, EMRS Proc., B Vol. 7 (2009)

[26] Y. Wei, A. Gin, and M. Razeghi, G. J. Brown, Appl. Phys. Lett., Vol. 80, 3262 (2002)

[27] C. H. Grein, H. Cruz, M. E. Flatté, H. Ehrenreich, Appl. Phys. Lett., Vol. 65, 2530 (1994)

[28] E. R. Youngdale, J. R. Meyer, C. A. Hoffman, and F. J. Bartoli, C. H. Grein, P. M. Young, H. Ehrenreich, R. H. Miles and D. H. Chow, Appl. Phys. Lett., Vol. 64, 3160 (1994)

[29] M. Razeghi, S. A. Pour, E. K. Huang, G. Chen, A. Haddadi, B. M. Nguyen, Opto-Electronics Rev.,

Vol. 19, 46 (2011)

[30] M. J. Yang, B. R. Bennett, Electron. Lett., Vol. 30, 1710 (1994)

[31] Y. Wei, A. Gin, M. Razeghi, G. J. Brown, Appl. Phys. Lett., Vol. 81, 3675 (2002)

[32] B.-M. Nguyen, D. Hoffman, P.-Y. Delaunay, and M. Razeghia, Appl. Phys. Lett., Vol. 91, 163511 (2007)

[33] M. Walther, J. Schmitz, R. Rehm, S. Kopta, F. Fuchs, J. Fleißner, W. Cabanski, J. Ziegler, J. of Cryst. Growth, Vol. 278, 156 (2005)

[34] H. S. Kim, E. Plis, J. B. Rodriguez, G. D. Bishop, Y. D. Sharma, L. R. Dawson, S. Krishna, J. Bundas, R. Cook, D. Burrows, R. Dennis, K. Patnaude, A. Reisinger, M. Sundaram, Appl. Phys. Lett., Vol. 92, 183502 (2008)

[35] H. Matsunami, *Semiconductor engineering* (1996)

[36] B.-M. Nguyen, D. Hoffman, E. K. Huang, S. Bogdanov, P.-Y. Delaunay, M. Razeghi, M. Z. Tidrow, Appl. Phys. Lett., Vol. 94, 223506 (2009)

[37] B. Brar, and D. Leonard, Appl. Phys. Lett., Vol. 66, 463 (1995)

[38] P. M. Thibado, B. R. Bennett, M. E. Twigg, B. V. Shanabrook, and L. J. Whitman , J. Vac. Sci. Technol., A Vol. 14, 885 (1996)

[39] W. M. Yim, R. J. Paff, J. of Appl. Phys., Vol. 45, 1456 (1974)

[40] M. Kondow, K. Uomi, A. Niwa, T, Kitatani, S. Watahiki, Y. Yazawa, Jpn, J. of Appl. Phys., Vol. 35, 1273 (1996)

[41] M. R. Gokhale, J. Wei, H. Wang, S. R. Forrest, Appl. Phys. Lett., Vol. 74, 1287 (1999)

[42] J.-X. Fu, S. R. Bank, M. A. Wistey, H. B. Yuen, J. S. Harris, Jr., J. of Vac. Sci, and Technol., B Vol. 22, 1463 (2004)

[43] M. Kondow, S. Nakatsuka, T. Kitatani, Y. Yazawa, M. Okai, Jpn. J. of Appl. Phys., Vol. 35, 5711 (1996)

[44] M. Kondow, T. Kitatani, K. Nakahara, T. Tanaka, Jpn. J. of Appl. Phys., Vol. 38, L1355 (1999)

[45] A. Yamamoto, Y. Kawamura, H. Naito, N. Inoue, J. of Cryst. Growth, 201/202, Vol. 872 (1999)

[46] J. Hu, X. G. Xu, J. A. H. Stotz, S. P. Watkins, A. E. Curzon, and M. L. W. Thewalt, N. Matine, C. R. Bolognesi, Appl. Phys. Lett., Vol. 73, 2799 (1998)

[47] R. Sidhu, N. Duan, J. C. Campbell, A. L. Holmes, Jr., IEEE Photon. Technol. Lett., Vol. 17, 2715 (2005)

[48] R. Sidhu, L. Zhang, N. Tan, N. Duan, J.C. Campbell, A.L. Holmes, Jr., C.-F. Hsu, M.A. Itzler, Electon. Lett., Vol. 42, 181 (2006)

[49] B. Chen, W. Jiang, J. Yuan, A. L. Holmes, Jr., B. M. Onat, IEEE J. of Quantum Electron., Vol. 47, 1244 (2011)

Chapter 2 Experimental details

In this chapter, Experimental details in this study are described such as epitaxial growth, characterization of crystalline quality of epitaxial layers, device process and characterization of device.

2.1 Epitaxial growth method

The author used solid source molecular beam epitaxy (SS-MBE) method for epitaxial growth of absorption layers of the sensors for these advantages;

• Sources can be easily handled (AsH_3 gas or metalorganics are not needed).

• Growing InGaAsN layers on InP substrates with high N composition is expected to be relatively easy. It is reported that incorporation of N is negligible in InGaAsN layer with In composition 0.5 grown by MOVPE method [1]. On the other hand, there are several reports about InGaAsN(Sb) with In composition > 0.5 and N composition ≥ 0.01 grown by MBE method [2-5].

• Surface reconstruction of substrate, which is extremely important for confirmation of removal of residual oxide as mentioned later, can be observed in situ by reflection of high energy electron diffraction (RHEED).

For NIR sensor, InP window layer is preferable because of more stable surface passivation [6]. However, growing InP by SS-MBE method is difficult due to possibility of toxic products and fire during opening the growth chamber. So InP window layers were re-grown by metalorganic vapor phase (MOVPE) method after growing absorption layers by MBE method.

2.1.1 MBE growth system

The author used MBE system produced by Epiquest Co. Ltd,. The image of the system is shown in

Fig. 2.1. Details of the system are described below;

• Basic construction

The MBE system mainly consists of growth chamber and load-locked chamber (Fig. 2.2). Both chambers are equipped with pumping systems, although the pumping system is abbreviated in Fig. 2.2.

• Pumping system

For pumping the growth chamber, an ion pump (IP) and a diffusion pump (DP) are equipped. The IP always pump the chamber except for growing InGaAsN layers. During the growth, DP and shroud filled with liquid nitrogen were used. While this study, the DP and the shroud were replaced by a turbo molecular pump (TMP) in order to improve exhausting power.

In the growth chamber, liquid nitrogen shrouds are located to adhere residual gas and excess growth materials. The lower limit of the pressure in the growth chamber is almost 1×10^{-8}Pa.

• Substrate heating

The substrate was heated by radiant heat of a carbon heater from the backside. In order to control the heater temperature, a thermocouple was allocated in the center of the heater, being separated from the substrate by approximately 1mm. The substrate temperature was measured by a pyrometer through a window.

A RHEED gun and a screen are equipped to characterize the surface reconstruction of the substrate before the growth.

• Material supply

As mentioned above, solid sources were used for the growth materials except N. Each material was supplied by a suitable cell.

- The group-III materials (Al, Ga, and In) were supplied by conventional effusion cells.

- As was supplied by a needle-valve cracking cell, which equipped with two heating zone. The schematic of the cell is figured in Fig. 2.3. The solid As source was stored in the crucible in the bulk zone (BZ). When As flux was needed for growth or thermal cleaning of InP substrate, the BZ was heated to evaporate the As source. In this stage, the As flux was composed of tetramer (As_4) [8]. The As flux passed through a long tube, which was also equipped with a heater. This

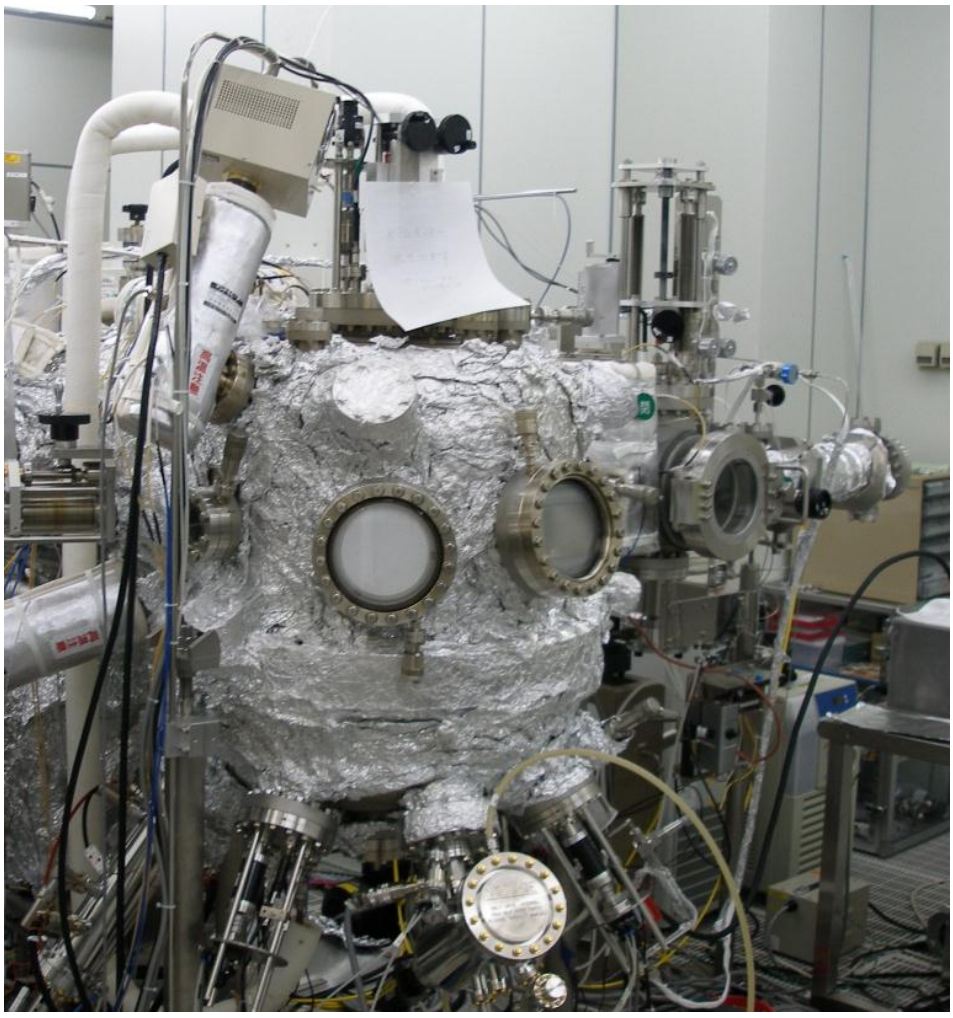

Fig. 2.1 Image of the MBE system

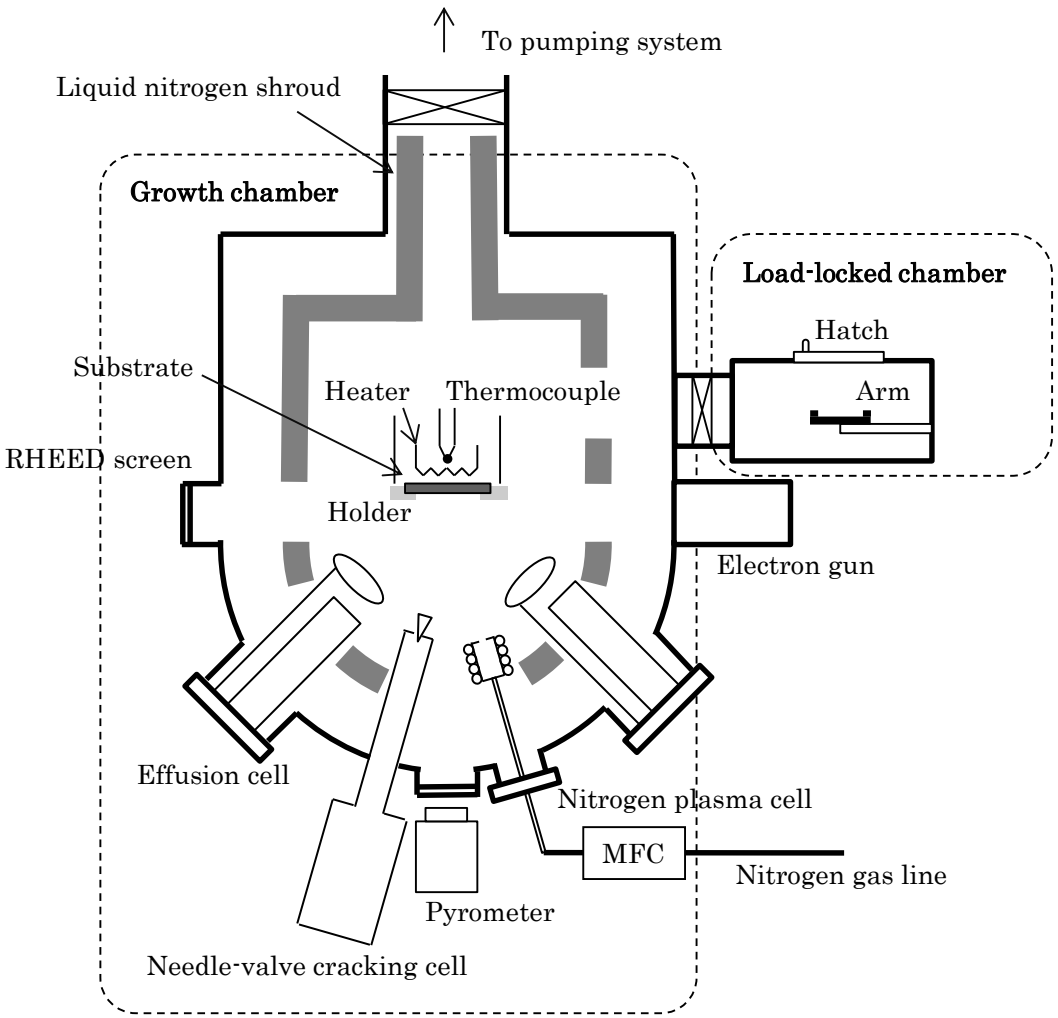

Fig.2.2. Structure of MBE system

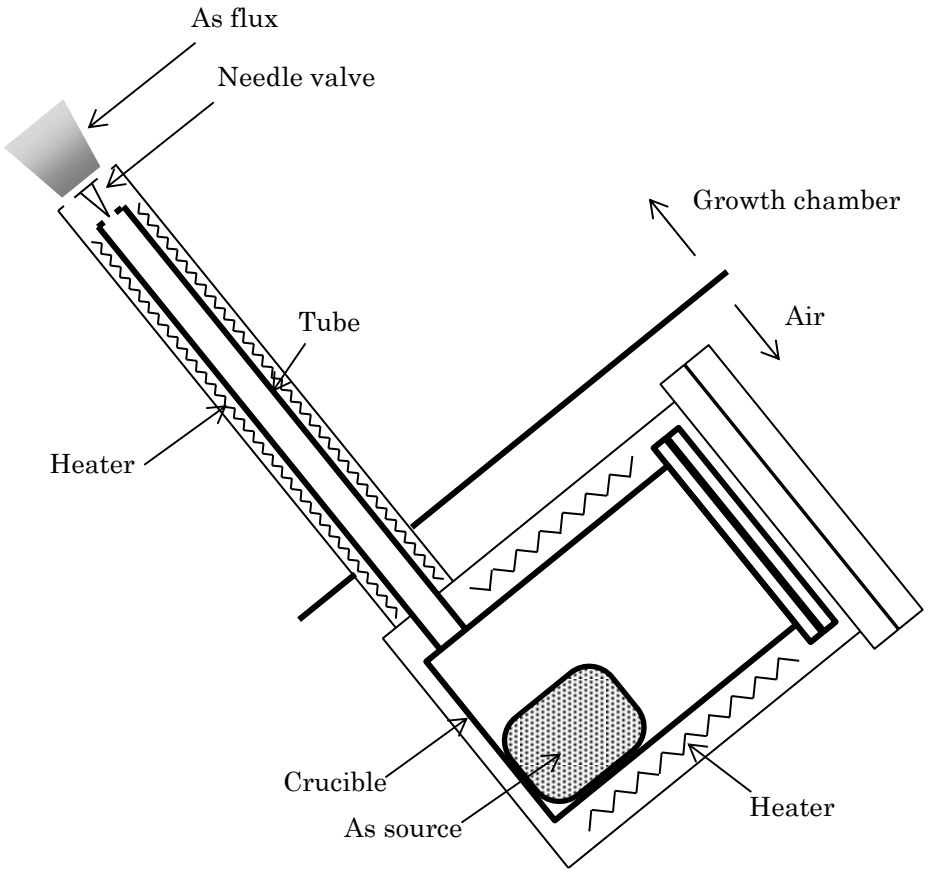

Fig. 2.3 Structure of the As needle-valve cracking cell

tube is called cracking zone (CZ). By heating the As flux in CZ sufficiently, the tetramers (As_4) was resolved into dimers (As_2). This process is called "cracking." By keeping the CZ at relatively low temperature, As_4 can be also used for growth. It is reported that using As_2 improved optical property of InGaAs [7]. In this study, effects of As cracking on the epitaxial layers were researched. The CZ was kept at 600 ºC and 900 ºC for As_4 and As_2, respectively [8]. The CZ must be kept at higher temperature than the BZ to avoid clogging of As in the tube.

- Sb was supplied with an effusion cell at first because it was used only for surfactant in InGaAsN growth. However, it is reported using cracked Sb also improves the crystalline quality of epitaxial layers [9]. An Sb needle-valve cracking cell was newly introduced in the studies of type-II InGaAs/GaAsSb and InAs/GaSb SLs because Sb is one of the main compositions. The Sb needle-valve cracking cell has similar construction to that of the As needle-valve cracking cell. In this study, the cell was operated with CZ at 800 or 900 ºC. At 800ºC, the Sb flux was composed of Sb_1 and Sb_2 with almost equal composition, while approximately 90% of the Sb is dissociated into Sb_1 at 900 ºC [9].

- N was supplied using an electron cyclotron resonance (ECR) plasma cell and radio frequency (RF) plasma cell.

All the supplies of the materials except N were controlled by beam equivalent pressure (BEP) measured by an ion gauge. The supply of N was controlled by gas flow rate and plasma power. A mass flow controller (MFC) is equipped on the nitrogen gas line to control the gas flow.

• Load-locked chamber

The load-locked chamber is directly connected to the air via a hatch and usually vacuumed. During loading and taking out substrates, the load-lock chamber is filled with nitrogen gas to the air pressure.

2.1.2 Growth procedure

The MBE growth was performed in the following procedure;

• The 2"ϕ or 17mm□ substrate is set on the In-free holder made of Mo in the air. The holder is put in the load-locked chamber. All the substrates used in this study are epi-ready.

• After the load-locked chamber is vacuumed for longer than 8 hours to ~5×10^{-6}Pa, the substrate is heated at 100ºC for 1.5 hours to desorb H_2O on the substrate.

• Liquid nitrogen was poured in the shrouds in the growth chamber. After the shrouds were filled, the cells but the nitrogen plasma cells were heated up to operating temperature.

• An ion gauge was put where the substrates were set during growth to measure the material supplies. The effusion cell temperatures were adjusted until desired BEPs were obtained. The BEPs of As and Sb by the needle-valve cracking cells were controlled by valve opening.

• The substrate is transferred to the growing chamber and cleaned thermally to desorb surface oxide. The way of cleaning is different by the substrate material;

- InP substrate needs to be heated until the RHEED pattern is transformed from ×2 to ×4 along the [011] azimuth, which indicates desorption of surface oxide [10]. The substrate is heated under As pressure until the RHEED pattern is changed from x2 to x4 (Fig 2.4(a)). The substrate temperature at which the pattern changes is around 530ºC.

- GaSb substrate needs to be heated until RHEED ×3 pattern appears along the [01-1] azimuth, which indicates desorption of surface oxide [11]. The substrate is heated under Sb pressure until the RHEED ×1 pattern appears. The substrate temperature where the pattern appears is around 560ºC. The substrate was heated at the temperature for 15min. Then, the RHEED pattern changes to ×3 (Fig. 2.4(b)).

• The substrate temperature is lowered to the prescribed temperature to start the growth. The substrate temperature, the temperatures of the effusion cells, valve opening of the needle-valve cracking cells, and the cell shutters are controlled by a computer. In order to improve the uniformity of characteristics of the epitaxial layers (layer thickness, composition of compound, defect density and so on), the substrate is rotated in 10 rpm during growth, because the characteristics are severely affected by the distributions of substrate temperature and material supply.

• After the growth is finished, the substrate is taken out in the air through the load-locked chamber.

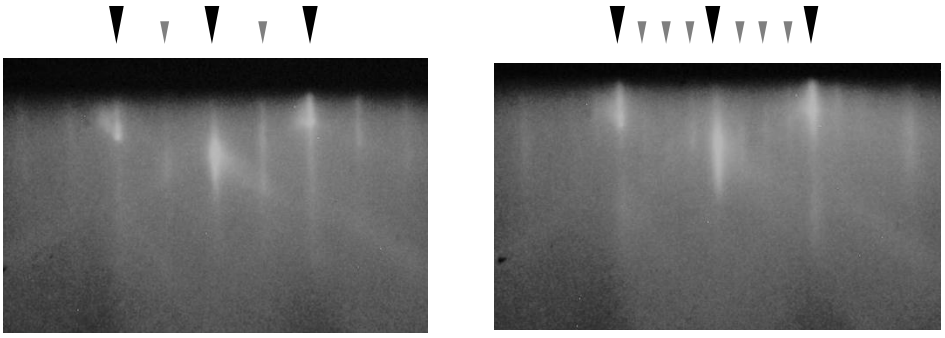

x2 x4

(a) InP substrate along the [011] azimuth

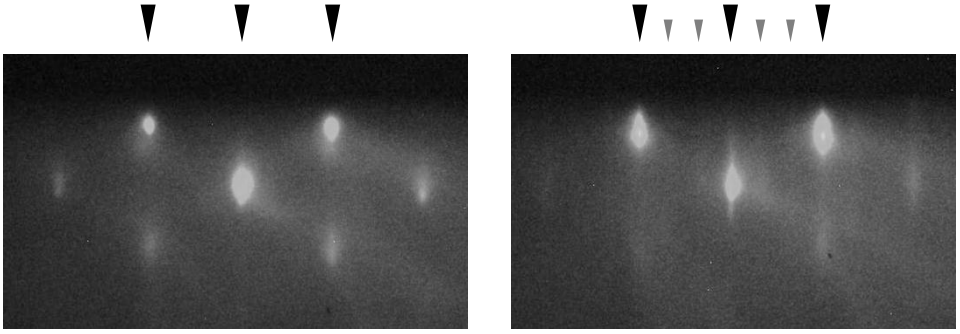

x1 x3

(b) GaSb substrates along the [01-1] azimuth

Fig.2.4 Typical RHEED patterns of (a) InP and (b) GaSb substrate during thermal cleaning

2.2 Characterization of crystalline quality

2.2.1 Optical microscopy

Surface morphology of the sample was observed by optical microscopy. Outstanding defects, such as crosshatch, defects with cores, boat-shaped defects, are observed. It was also checked whether the surfaces are smooth or rough.

2.2.2 Atomic force microscopy

Tapping mode atomic force microscopy (AFM) was used to observe more detailed surface morphology. Root mean square (Rms) roughness was measured.

2.2.3 X-ray diffraction

Four-crystal $2\theta/\omega$ X-ray diffraction (XRD) was used to measure the lattice constants of the epitaxial layers, $\Delta a/a$ between the epitaxial layers and the substrates, compound compositions (such as InGaAs), and periods of SLs. Full-width at half-maximums (FWHMs) of $2\theta/\omega$ x-ray rocking curves (XRCs) of the epitaxial layers were also measured as a parameter of crystalline quality. Cu $K\alpha_1$ (λ=1.54056Å) was used. The parameters of the epitaxial layers were calculated in the following methods;

• Lattice constant

All the materials discussed in this study have zinc blende structure (Fig. 2.5), which can be considered as two interpenetrating face-centered cubic lattices of the elements of III-column and V-column [12].

Lattice constants normal to the plane ($a_\perp$) of epitaxial layers were measured by conventional Bragg's diffraction (Fig 2.6). Plane (400) was used in this study. In that case, the lattice constant is calculated by this equation;

$$a_\perp = 4d = \frac{2\lambda}{\sin\theta} \tag{2.1}$$

where d and θ stand for distance between neighboring plane, and angle of Bragg's diffraction, respectively.

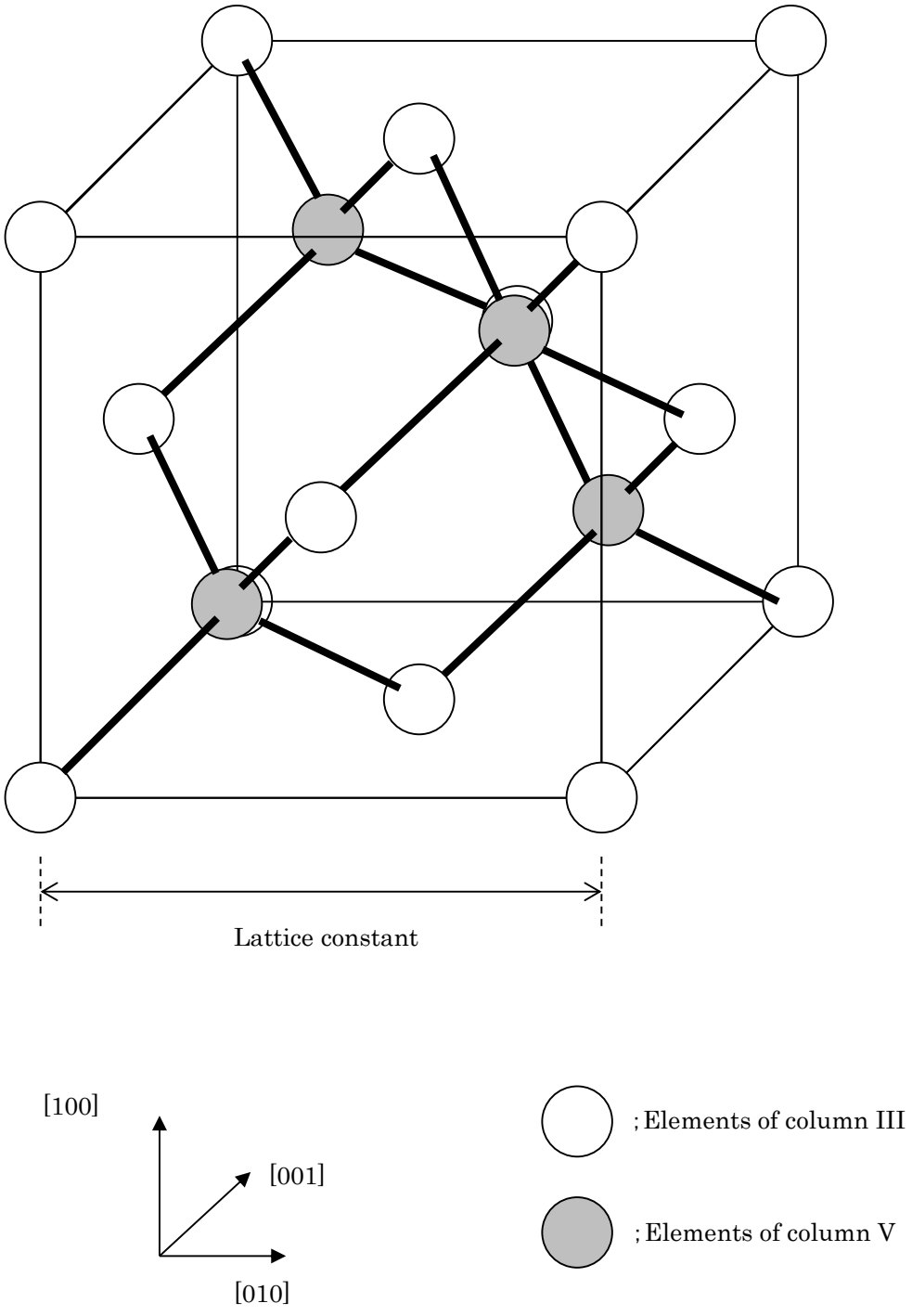

Fig. 2.5 Zinc blende structure

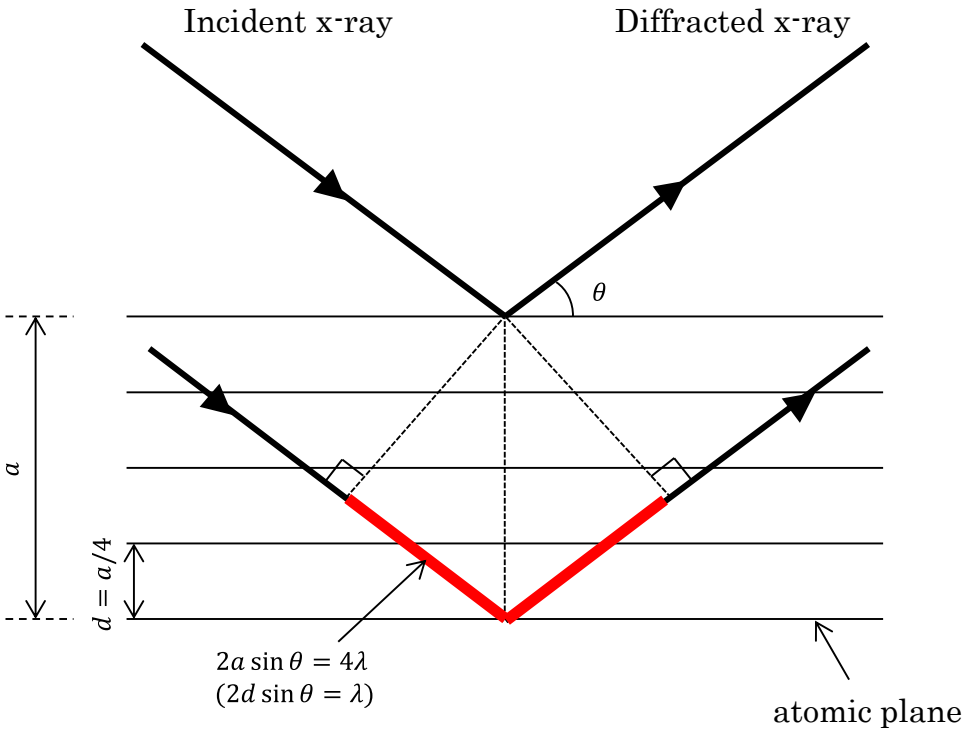

Fig. 2.6 Schematics of Bragg's diffraction

• $\Delta a/a$

$\Delta a/a$ is a popular parameter to express the difference of the lattice constant of the epitaxial layer from that of the substrate. It is usually calculated with the following equation;

$$\frac{\Delta a}{a} = \frac{a_{\mathrm{epi}} - a_{\mathrm{sub}}}{a_{\mathrm{sub}}} \tag{2.2}$$

where a_{epi} and a_{sub} denote lattice constants of the epitaxial layer and the substrates, respectively. However, small $\Delta a/a$ can be calculated approximately by the result of XRD. Differentiating the equation 2.1 by θ gives following equation;

$$\frac{\Delta a}{\Delta \theta} = -\frac{2\lambda \cos\theta}{\sin^2\theta} = -a\cot\theta \tag{2.3}$$

Because $\Delta\theta$ equals $\Delta\omega$, the equation 2.4 can be changed in this form;

$$\frac{\Delta a}{a} = -\Delta\omega \cot\theta \tag{2.4}$$

This equation suggests that $\Delta a/a$ is proportional to $\Delta\omega$.

• Compound composition of alloy

As mentioned in Chapter 1, the lattice constant of the freestanding ternary compound semiconductor alloy is proportional to the composition. However, lattice constants of epitaxial layers of compound semiconductor alloys are more or less different from those of substrates, even if they were intended to grow lattice-matched. Therefore, the lattice constants of compound semiconductor epitaxial layers should be evaluated considering strain.

At the initial stage of epitaxial growth, the epitaxial layer is grown psuedomorphically to the substrate (Fig. 2.7(a)), i.e. the lattice constant of the epitaxial layer parallel to the plane ($a_{\parallel}$) is fitted to that of the substrate. Compressive strain is added in the case that the lattice constant of the epitaxial layer is larger than that of the substrate. And tensile strain is added in the case that the lattice constant of the epitaxial layer is smaller than that of the substrate. Lattice constants of strained epitaxial layers normal to the plane ($a_{\perp}$) are changed in a complicated manner mentioned later. When the thickness of the epitaxial layers exceeds the critical thickness, the strain begins to be relaxed by introduction of defects, such as dislocations (Fig. 2.7(b)). In 1974, Mattews and Blakeslee proposed that the critical thickness h_{c} of the single epitaxial layer grown on the substrate with infinite thickness is given by the following equation [13];

$$h_{\mathrm{c}} = \frac{b}{8\pi f}\frac{(1-\nu\cos^2\alpha)}{(1+\nu)\cos\lambda}\left(\ln\frac{h_{\mathrm{c}}}{b}+1\right) \tag{2.6}$$

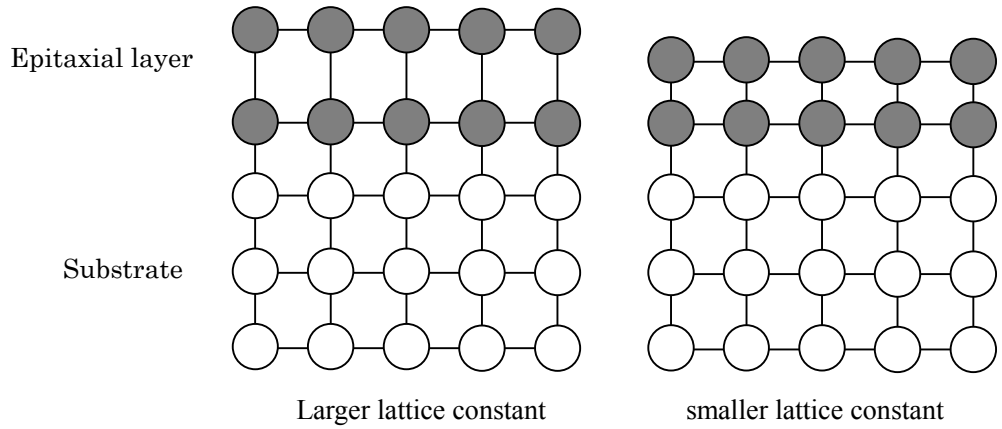

(a) Within critical thikness

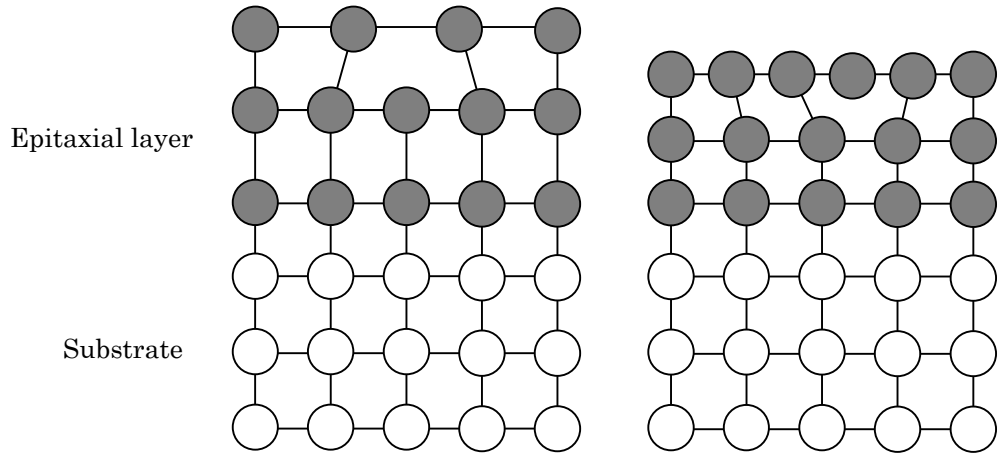

(b) Over critical thikness

Fig. 2.7 Epitaxial growth of layers with lattice mismatch

where b, f, ν, α, and λ denote length of Burger's vector of dislocation derived from strain relaxation, lattice mismatch between the epitaxial layer and the substrate, Poisson's ratio, the angle between the dislocation line and its Burgers vector, and the angle between the slip direction and that direction in the film plane which is perpendicular to the line of intersection of the slip plane and the interface. The value of h_c for layers in a multilayer is four times as great as the critical thickness given by equation (2.6) due to the two factors; the shared elastic misfit strain in a multilayer, and the fact that the motion of a dislocation makes misfit dislocations not only at the interface below the epitaxial layer but also at the interface above the epitaxial layer [13]. Assuming b, ν, α and λ equal 5Å, 0.333, 60°, 0°, respectively, the relations between the lattice mismatch and the critical thickness of single layer and multilayer are given as Fig. 2.8. The critical thicknesses obviously become smaller with larger lattice mismatch.

The samples characterized in this study are roughly classified into two sets in terms of thickness; thick single layers (1μm or thicker), and multilayers with several-nm periods. The critical thickness for single layers is only 190nm even if the lattice mismatch is as small as 0.05%. Therefore, the samples of the former set are assumed to be fully relaxed. In this case, the composition of the alloy can be calculated simply by $a_\perp$ of the epitaxial layer measured by XRD because $a_\perp$ varies linearly by the composition. On the other hand, the critical thickness for multilayers exceeds 10nm even if the lattice mismatch is as large as 2%. Therefore, the samples of the latter set are assumed to be grown psuedomorphically. In this case, $a_\perp$ of the epitaxial layer is calculated by Hooke's law. In cubic system, the relation of stress tensor and strain tensor are expressed as below;

$$\begin{bmatrix} T_{xx} \\ T_{yy} \\ T_{zz} \\ T_{yz} \\ T_{zx} \\ T_{xy} \end{bmatrix} = \begin{bmatrix} c_{11} & c_{12} & c_{12} & 0 & 0 & 0 \\ c_{12} & c_{11} & c_{12} & 0 & 0 & 0 \\ c_{12} & c_{12} & c_{11} & 0 & 0 & 0 \\ 0 & 0 & 0 & c_{44} & 0 & 0 \\ 0 & 0 & 0 & 0 & c_{44} & 0 \\ 0 & 0 & 0 & 0 & 0 & c_{44} \end{bmatrix} \begin{bmatrix} e_{xx} \\ e_{yy} \\ e_{zz} \\ e_{yz} \\ e_{zx} \\ e_{xy} \end{bmatrix} \tag{2.7}$$

where $\{T_{xx},\ T_{yy}, \cdots\}$, $(c_{11},\ c_{12},\ c_{44})$ and $\{e_{xx},\ e_{yy}, \cdots\}$ stand for stress tensor, elastic stiffness and strain tensor, respectively. Assuming uniform strain in plane ($e_{xx} = e_{yy} = e$) and no other stress ($T_{zz} = 0$), the tensors can be changed as below;

$$e_{zz} = -\frac{2c_{12}}{c_{11}} e \tag{2.9}$$

This equation can be changed by using Poisson's ratio ($\nu = c_{12}/(c_{11} + c_{12})$);

$$e_{zz} = -\frac{2\nu}{1-\nu} e \tag{2.10}$$

From this equation, the relation between $a_\perp$ and $a_\parallel$ is given in the following equation;

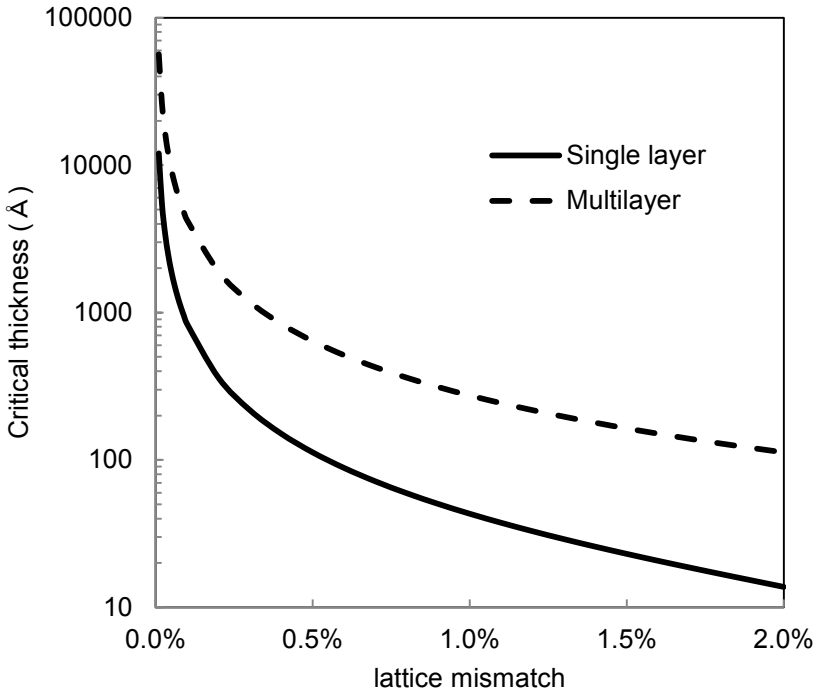

Fig. 2.8 Relation between the lattice mismatch and the critical thickness

$$\left(a_{\perp} - a_{\text{freestanding}}\right) = -\frac{2\nu}{1-\nu}\left(a_{\parallel} - a_{\text{freestanding}}\right) \tag{2.11}$$

where $a_{\text{freestanding}}$ denotes the lattice constant of freestanding epitaxial layer. If the epitaxial layer is grown psuedomorphically to the substrate, a_{sub} is substituted for $a_{\parallel}$ in the equation (2.11).

The composition of alloy was evaluated by finding an appropriate composition which gives a simulated XRC fitted to the measured XRC. Poisson's ratio of the alloy is essentially calculated using c_{11} and c_{12}, which are known to vary linearly with the alloy [14]. However, the author calculated Poisson's ratio of the alloy using a linear variation of Poisson's ratio with composition, because it was confirmed that Poisson's ratios calculated in the two ways were sufficiently close.

• Period of SL

In 2θ/ω XRCs of a periodic SL, satellite peaks appear around the main diffraction peak of the SL. In (400) measurement, the diffraction peak angle $\theta_{\text{satellite}}$ is expressed in this equation;

$$\sin\theta_{\text{satellite}} = \frac{2\lambda}{a_{\text{SL}}} + \frac{2n\lambda}{d_{\text{SL}}} \tag{2.12}$$

where a_{SL} and d_{SL} denote lattice constant and period of SL, respectively. n stands for index number (0, ±1, ±2, …). If n equals 0, $\theta_{\text{satellite}}$ equals the angle of main peak of the SL.

An example of SL period calculation is described. An XRC of an InAs/GaSb SL on a GaSb substrate is shown in Fig. 2.9 (a). The main peak and some satellite peaks are seen (The main peak position coincides with that of the GaSb substrate, probably due to incorporation of Sb in InAs layers.). The index number and the corresponding $\sin\theta_{\text{satellite}}$ are plotted in a graph (Fig. 2.9 (b)). The period of the SL is calculated using the slope of the graph (0.0092973 in this case) because it equals $2\lambda/d_{\text{SL}}$. The period is 82.8Å.

The parameters used in this study are summarized in Table 2.1 [15].

Table 2.1 Parameters used in this study

Material	Lattice constant (Å)	Elastic stiffness (Gpa)		Poisson's ratio
		c_{11}	c_{12}	
InP	5.8697	-	-	-
GaAs	5.65325	1221	566	0.317
InAs	6.0583	832.9	452.6	0.352
GaSb	6.0959	884.2	402.6	0.313
InSb	6.4794	684.7	373.5	0.353

(300K)

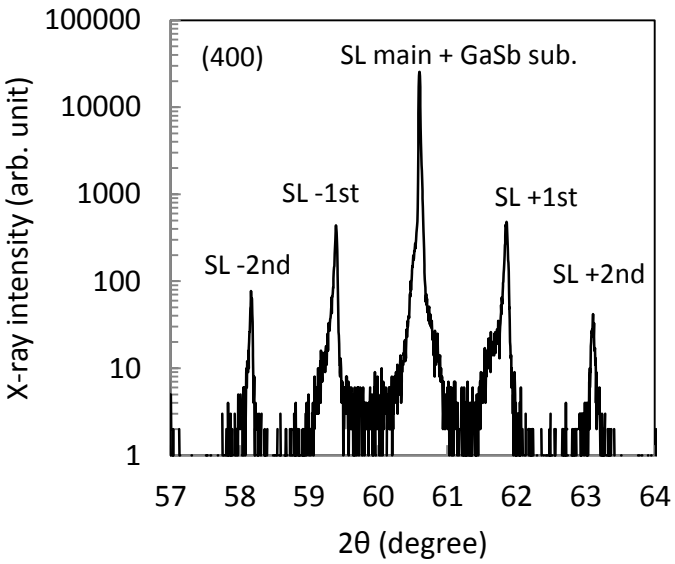

(a) XRC of the InAs/GaSb SL

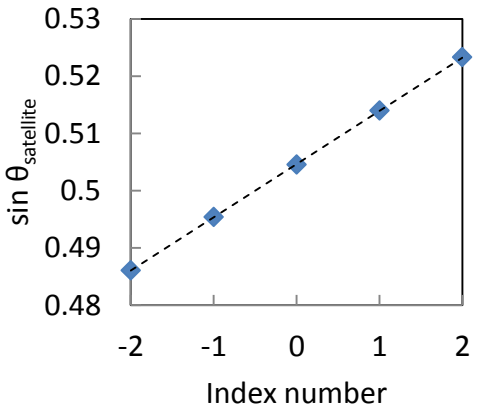

(b) Relation of the index number and sin $\theta_{satellite}$

Fig. 2.9 Calculation of the SL period by XRD

2.2.4 Photoluminescence

In order to characterize optical properties of the epitaxial layers, photoluminescence (PL) measurements were performed using several systems. For simple measurement of single layers (emission wavelength of around 2μm) at room temperature, systems with the following light sources and detectors were used;

- Ar ion laser (514nm) and PbS detector
- YAG laser (1064nm) and InGaAs detector (lattice-matched and extended)
- YAG laser (1064nm) and MCT detector

The spectra were measured by monochromator in the systems.

For more detailed measurement such as excitation power dependence and temperature dependence, a system with a Fourier transform infrared spectrometer (FT-IR) instead of monochromator, a YAG laser (1064nm) and a MCT detector was used. The FT-IR enabled us to measure samples with long emission wavelength (several-μm). The inside of the system was filled with nitrogen gas during measurement in order to prevent absorption by molecules in the air, such as H_2O and CO_2.

2.2.5 Photoreflectance

Photoreflectance (PR) measurements were carried out to estimate the band gap of epitaxial layers. Light from a 100W tungsten lamp was used, which was focused through a monochromator onto the surface of the sample. A YAG laser (1064 nm) was used as the modulation beam. The band gap was estimated by fitting the PR spectra with the Aspnes third derivative functional form (TDFF) [16]

$$\frac{\Delta R}{R} = \mathrm{Re}\left(\frac{Ce^{i\theta}}{\left(E - E_{\mathrm{g}} + i\Gamma\right)^{n}}\right) \tag{2.13}$$

where C, θ, E, E_{g} and Γ denote the line shape amplitude, the phase angle, the photon energy, the band gap and the broadening parameter, respectively. The term n refers to the type of optical transition, and is assumed to be 3 in this study.

2.2.6 Transparency spectrum measurement

Transparency spectra of epitaxial layers and substrates were measured at room temperature. Two kinds of systems were used. The schematic of the systems is illustrated in Fig. 2.10.

The one system for measurement of wavelength around 2.5μm was equipped with a

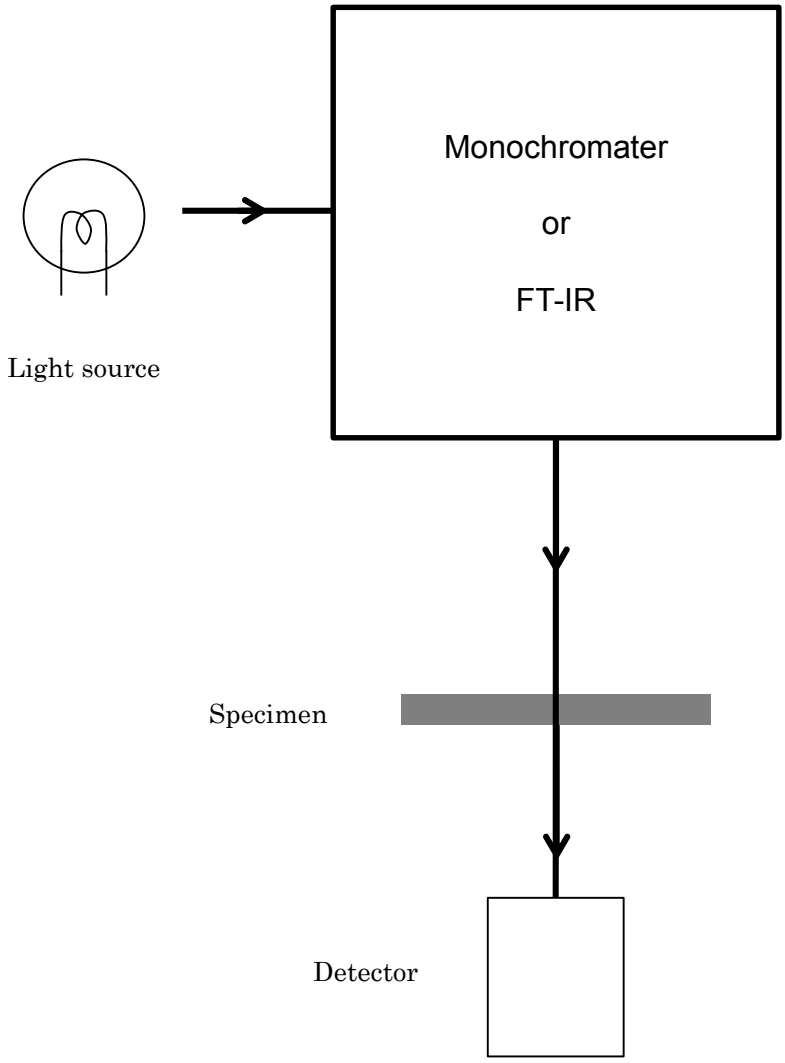

Fig. 2.10 Schematic of systems for transparency spectrum measurement

monochromator.

The light from light source penetrated the specimen and was detected by a detector. The transparency spectrum is calculated by the intensity ratio of the light penetrating the specimen and the light without penetrating the specimen.

The other system for measurement of wavelength longer than 3μm utilized a FT-IR instead of a monochromator. The system shared the light path with the PL measurement system mentioned in the last subsection.

2.2.7 Hall measurement

To evaluate the electric property of epitaxial layer (carrier-type, carrier concentration and mobility), Hall measurements were performed by conventional Van der Paw method, using about 6mm□ specimen with In solder electrodes on the corners.

2.2.8 Secondary ion mass spectroscopy

The depth profiles of the N in InGaAsN (D_{N}) and the Sb density in InGaAsNSb (D_{Sb}) were measured by utilizing the secondary ion mass spectroscopy (SIMS) with Cs^{+} primary ion. $^{14}N+^{75}As$, and ^{121}Sb were detected to measure the depth profiles of D_{N} and D_{Sb}, respectively. As markers, ^{69}Ga in the InGaAsN(Sb) and $^{27}Al+^{27}Al$ in AlInAs buffer layer under the InGaAsN(Sb) layer were also detected to measure the depth profiles of Ga and Al, respectively. The compositions of N and Sb were evaluated by D_{N} and D_{Sb}, and the densities of V-column elements. The compositions are expressed in the following equation, because 4 elements are contained in a zinc blende unit cell, and the InGaAsN(Sb) layers are assumed to be fully relaxed as mentioned in 2.2.4;

$$x_{\mathrm{N,Sb}} = \frac{D_{\mathrm{N,Sb}}}{4/{a_{\mathrm{InGaAsN(Sb)}}}^3} = \frac{D_{\mathrm{N,Sb}}}{4/\{a_{\mathrm{InP}}(1+\Delta a/a)\}^3} \tag{2.13}$$

2.2.9 Transmission electron microscopy

In order to observe distributions of threading dislocations in the epitaxial layers, cross sectional transmission electron microscopy (TEM) was utilized. The specimens with thickness of around 100nm were prepared by focused ion beam (FIB) method.

2.3 Device process and characterization

2.3.1 Device process

In this study, three kinds of devices are fabricated and characterized; NIR discrete sensors, NIR FPAs, and MIR discrete sensors. Details of those device processes are described;

NIR discrete sensors

NIR discrete sensors were fabricated to examine the characteristics of the absorption layer materials. Planar type p-on-n structure was adopted because thermal diffusion technique can be applied. Schematic of the typical NIR discrete sensor structure is illustrated in Fig. 2.11. The device was fabricated by the following procedure;

• 100nm-thick SiN is deposited on the surface of the epitaxial layer for passivation by plasma enhanced chemical vapor deposition (PE-CVD).

• The window for selective thermal diffusion of zinc is formed by conventional photolithography and HF etching.

• The p-n junction is formed in the absorption layer by selective thermal diffusion of Zn.

• 180nm-thick SiON is deposited by PE-CVD for anti-reflection (AR) coating layer.

• The Au-Zn p-type electrode was evaporated on the surfaces of the Zn-diffused regions and metallized in nitrogen atmosphere in a rapid thermal annealing (RTA) furnace. The annealing temperature is 390~420°C and the annealing duration is 1min.

• The Au-Ge-Ni n-type electrode was evaporated on the backside of the InP substrate and metallized in nitrogen atmosphere in the RTA furnace. The annealing temperature is 340°C and the annealing duration is 1min.

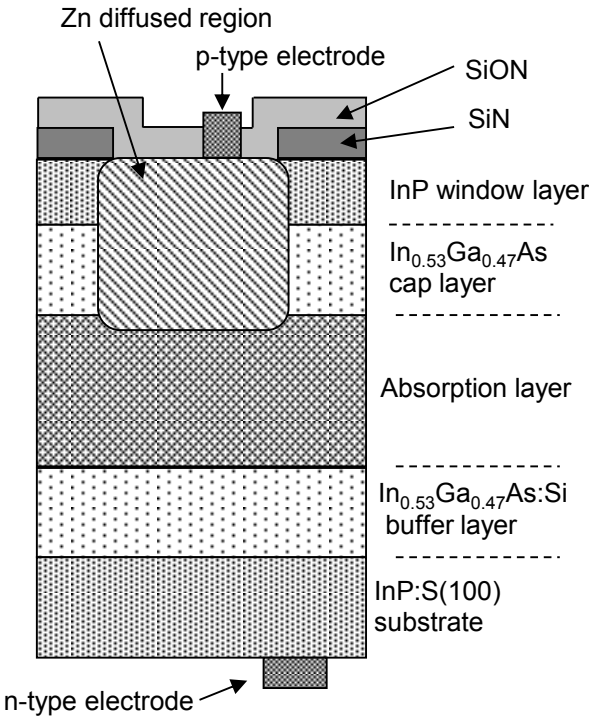

Fig.2.11Schematic of a typical NIR discrete sensor structure

NIR FPAs

Schematic of the NIR FPA is illustrated in Fig. 2.12. The FPA has 320×256 pixels and consists of the PD array and the readout-integrated circuit (ROIC) bonded to each other. Each pixel of the PD array is 15μm diameter and 30μm pitch. The isolation between neighboring PDs is experimentally confirmed. The device was fabricated by the following process;

• PD array is fabricated by basically the same procedure as the discrete PDs. Before the n-type electrode was evaporated on the backside of the InP substrate, the backside was polished and covered by a SiON AR-coating layer in order to receive incident light.

• Bump (made of Au or In) is deposited on each pixel of PD array by using lift-off technique.

• PD array is matched to the ROIC, then the two are bonded together under controlled pressure and temperature.

• The integrated device was assembled in ceramic package with Si lid.

MIR discrete sensors

MIR discrete sensors were also fabricated to examine the characteristics of the absorption layer materials. Schematic of the typical MIR discrete sensor structure is illustrated in Fig. 2.13. The structure is different from NIR discrete sensors in several respects. Although forming n-type region in GaSb by thermal diffusion of Te is reported [17, 18], the author experimentally found that diffusion of Te is difficult due to surface accumulation of Te. Therefore, mesa structures were adopted to isolate the sensors. N-on-p structure was adopted because only p-type GaSb can be used for buffer layer. Ohmic contact on n-type GaSb is difficult [19], and InAs with sufficient thickness cannot be grown due to the lattice mismatch. P-type electrodes are formed on etched surface of buffer layer because n-type GaSb:Te or semi-insulating InP:Fe substrates are often used. The devices were fabricated by the following procedure;

• The mask for mesa etching is formed by photolithography. The masks are made of resin, SiN, or SiON.

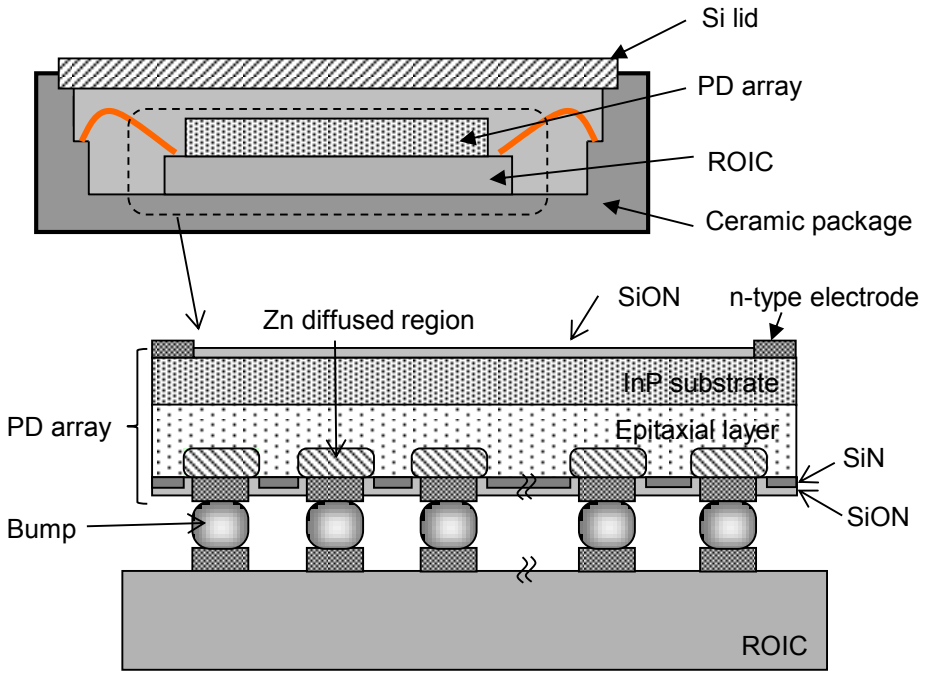

Fig.2.12 Schematic of NIR FPA structure

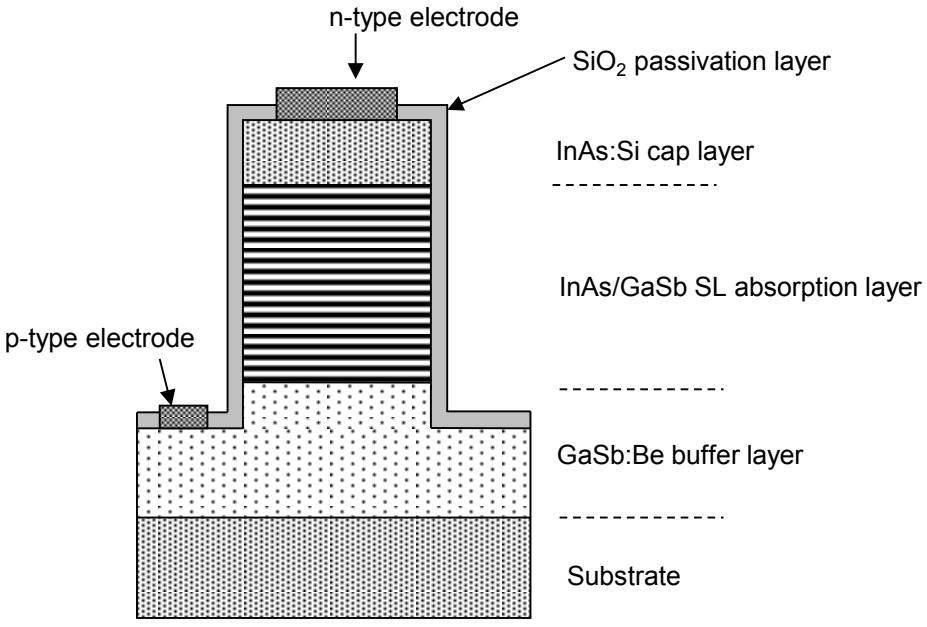

Fig.2.13 Schematic of a typical MIR discrete sensor structure

• The mesa structure is formed by wet chemical etching. The etchant contains H_2O, H_3PO_4, citric acid ($C_6H_8O_7$) and H_2O_2 (250ml:12ml:30g:25ml).

• The SiO_2 layer is deposited on sidewall of mesa by PE-CVD for passivation.

• The p-type and n-type electrodes, which consist of Au-Pt-Ti, are evaporated on top of the mesa and the etched surface of the buffer layer, respectively. The electrodes were not metalized.

2.3.2 Device characterization

Two important characteristics of discrete sensors, dark current and responsivity, were evaluated by current-voltage measurement and responsivity spectrum measurement, respectively.

Current-voltage measurement

Current-voltage measurements were performed by mounting the sensors on a prober and connecting the p-type and n-type electrodes of the sensors to a parameter analyzer.

Responsivity spectrum measurement

For responsivity spectra measurement of NIR discrete sensors and MIR discrete sensors, sensors with different structures were used;

NIR discrete sensors were equipped with ring-shaped p-electrodes (diameter; 1000μmϕ) on the tops to receive the incident light and mounted on cans. The n-electrodes were bonded on the cans, and the p-electrodes were connected to isolated pins by Au wires (Fig.2.14).

Each MIR discrete sensor had mesa structure where two circles were combined in plane. The one circle was equipped with n-electrodes (diameter; 800μmϕ), while the other was covered with only SiO2 passivation layer to receive incident light (diameter; 120~800μmϕ). The sensors are mounted in ceramic packages and the p-electrodes and n-electrodes were connected to electrodes of the ceramic packages (Fig. 2.15).

The schematic of the measurement system is illustrated in Fig. 2.16. The light from the light source was radiated to the discrete sensors through a monochromator. The outputs of the sensors were detected by a lock-in amplifier.

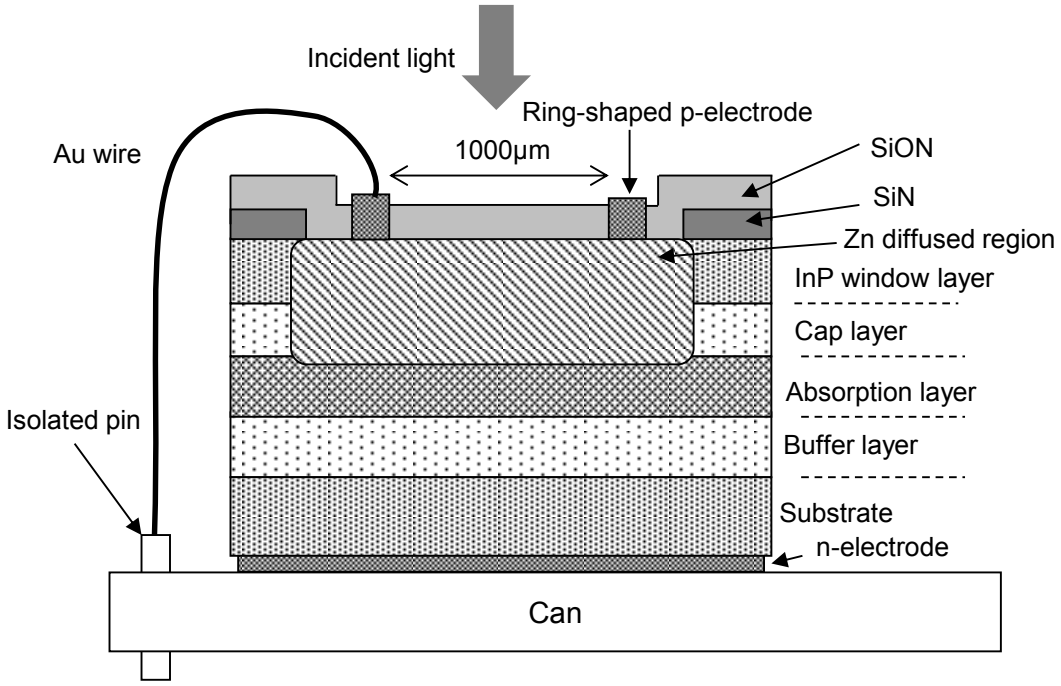

(a) Structure of a sensor

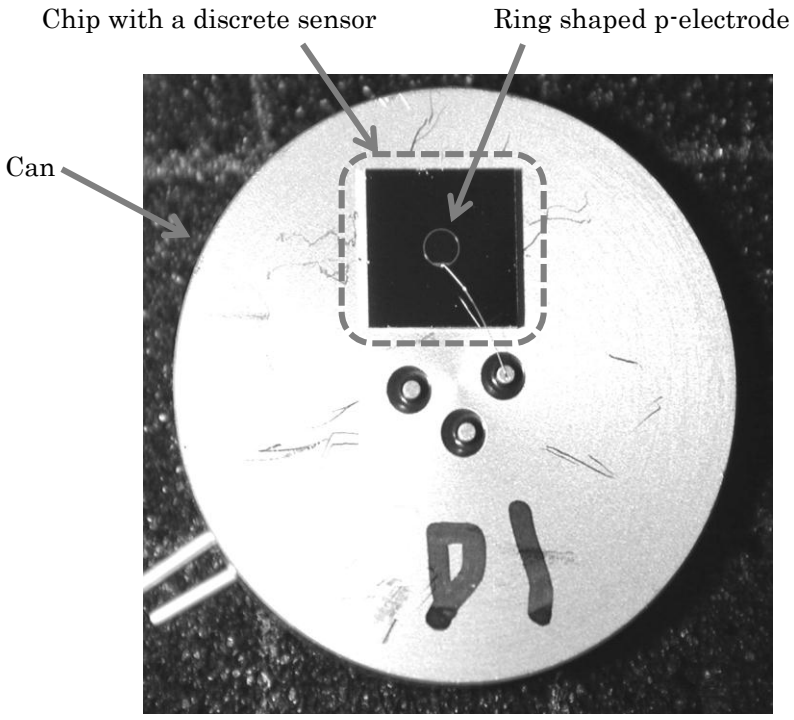

(b) Image of a sensor

Fig.2.14 NIR discrete sensors for responsivity spectrum measurement

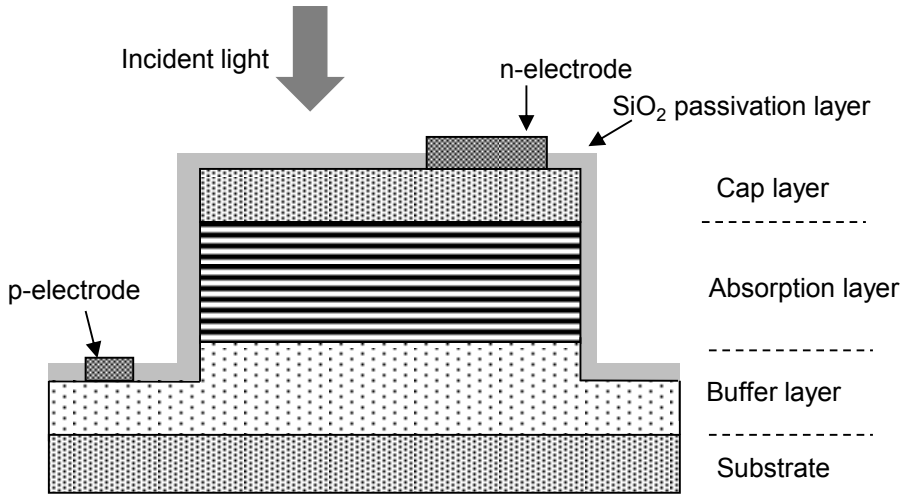

(a) Structure of a sensor

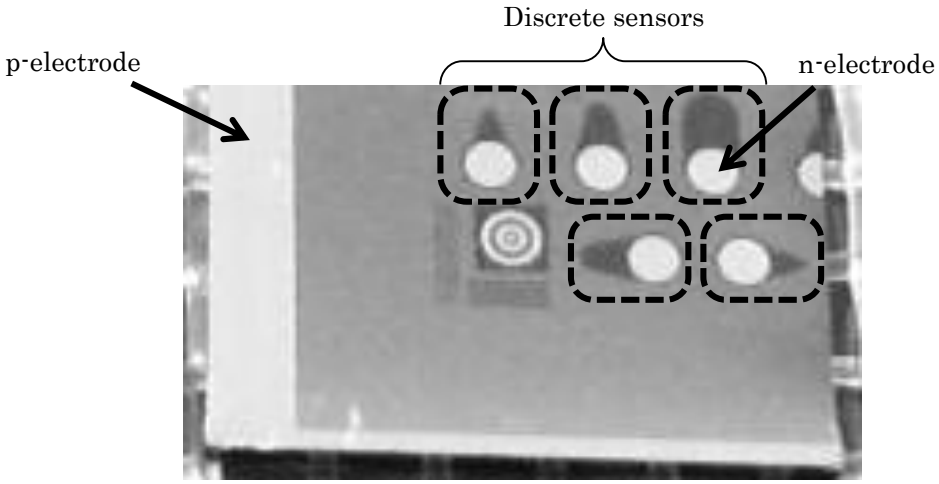

(b) Image of sensors (before mounting in a ceramic package)

Fig.2.15 MIR discrete sensors for responsivity spectrum measurement

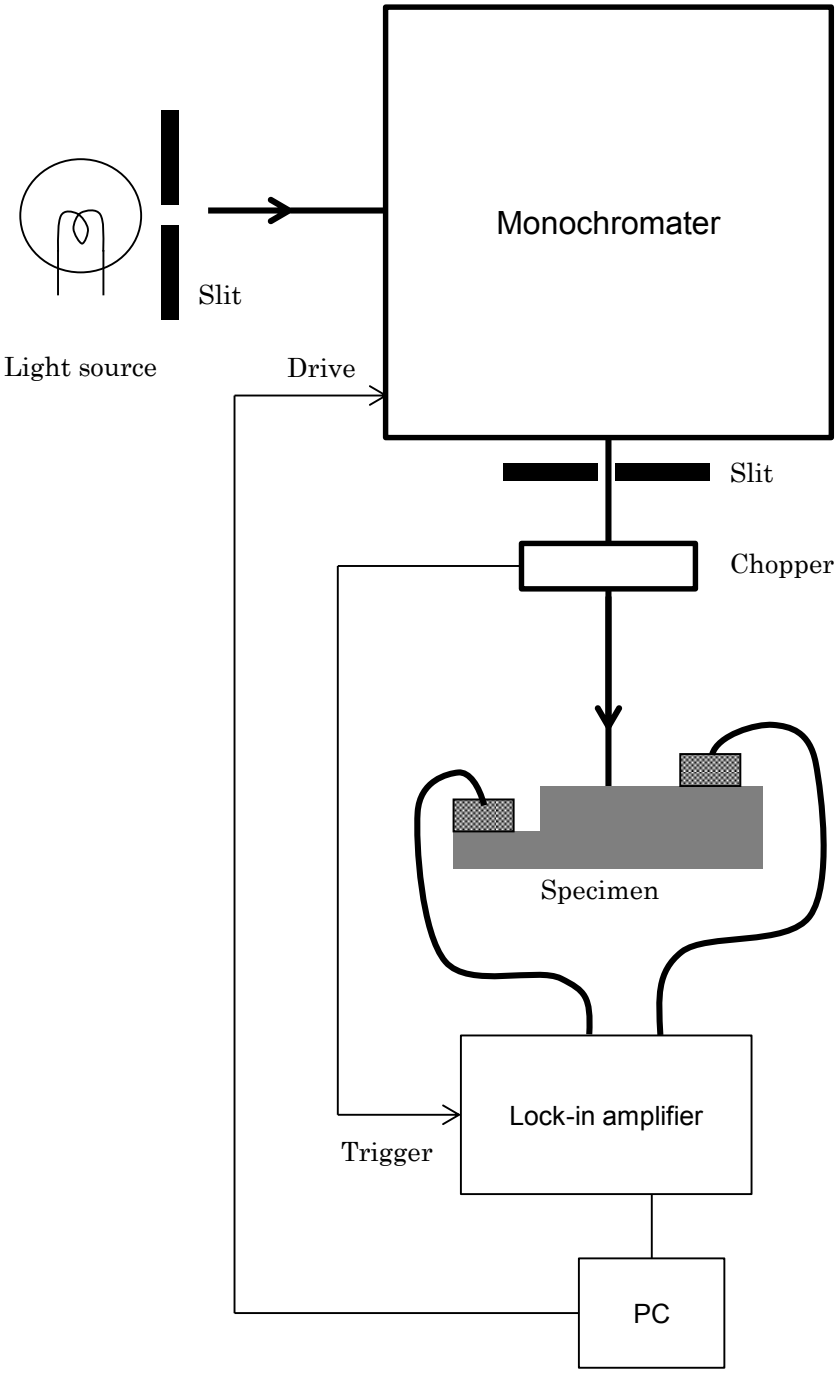

Fig. 2.16 Schematic of system for responsivity spectrum measurement

References

[1] D. J. Friedman, J. F. Geisz, S. R. Kurtz, J. M. Olson, and R. Reedy, J. Cryst. Growth Vol. 195, 438 (1998)

[2] M. R. Gokhale, J. Wei, H. Wang, S. R. Forrest; Appl. Phys. Lett., Vol. 74, 1287 (1999)

[3] Y. Kawamura, T. Nakagawa, N. Inoue, Jpn. J. of Appl. Phys., Vol. 44, 6000 (2005)

[4] Y. Kawamura, T. Nakagawa, N. Inoue, Jpn. J. of Appl. Phys., Vol. 45, 3453 (2006)

[5] J.-X. Fu, S. R. Bank, M. A. Wistey, H. B. Yuen, J. S. Harris, Jr., J. Vac. Sci. Technol. B Vol. 22, 1463 (2004)

[6] N. Susa, H. Kanbe, H. Ando, Y Ohmachi, Japanese J. of Appl. Phys. Vol.19, L675 (1980)

[7] D. Huet, M. Lambert, D. Bonnevie, D. Dufresne, J. of Vac. Sci. and Technol. B, Vol. 3 823 (1985)

[8] *Manual of the As needle-valve cracking cell*

[9] P. D. Brewer, D. H. Chow, and R. H. Miles, J. of Vac. Sci. and Technol. B, Vol. 14, 2335 (1996)

[10] S. F.Yoon, H. Q. Zheng, Materials Science and Engineering B, Vol. 55, 187 (1998)

[11] W. T. Tsang, T. H. Chiu, D. W. Kisker, J. A. Ditzenberger, Appl. Phy. Lett., Vol. 46 283 (1985)

[12] *S. M. Sze, Physics of semiconductor devices, 2nd edition* (1981)

[13] J. W. Mattews and A. E. Blakeslee, J. of Cryst. Growth Vol. 27 118 (1974)

[14] H. Nagai, S. Adachi, T. Fukui, *III-V Compound Semiconductor Alloy* (1988)

[15] I. Vurgaftman, J. R. Meyer, L. R. Ram-Mohan, J. of Appl. Phys., Vol. 89, 5815 (2001)

[16] D. E. Aspnes, Surf.Sci., Vol. 37, 418 (1973)

[17] P. S. Dutta, B. Méndez J. Piqueras, E. Diequez, H. L. Bhat, J. of Appl. Phys. Vol. 80, 1112 (1996)

[18] R. Rajavel, B. Nosho, S. Terterian, S. Bui, Y. Royter, T. de Lyon, Proc. of SPIE Vol. 7298, 72981S (2009)

[19] E. Plis, J. B. Rodriguez, H. S. Kim, G. Bishop, Y. D. Sharma, L. R. Dawson, S. Krishna, S. J. Lee, C. E. Jones, V. Gopal, Appl. Phys. Lett., Vol. 91, 133512 (2007)

Chapter 3 Growth and characterization of thick InGaAsN layers for near-infrared sensors

In this chapter, growth of thick InGaAsN layers is discussed. For absorption layers of NIR sensors, several-μm thick InGaAsN layer with high N composition is needed. The process of this study is mentioned below;

• At first, the author studied basic characteristics of thick InGaAsN layers using ECR plasma source because Kawamura et al. have utilized the ECR plasma cell to obtain laser diodes with dilute nitride active regions [1-4].

• Next, growth condition of InGaAsN is discussed in order to obtain InGaAsN layers with longer cutoff wavelength. An RF plasma cell was introduced because less ion damage at higher power levels might result in improved crystalline quality of epitaxial layers [5]. Growth temperature and As/III ratio were optimized [6, 7].

• Finally, NIR discrete sensors with InGaAsN absorption layers were fabricated and characterized.

3.1 Basic characteristics of thick InGaAsN

In this section, the author focused on the following items;

• Dependence of band gap of thick InGaAsN on N composition

The change of band gap of thick InGaAsN layers with increasing N composition was investigated by PL and PR measurement [7].

• Depth profile of N

Many reports discussed the homogeneity of InGaAsN crystal on GaAs substrates [8-10]. But there are only few reports about InGaAsN on InP substrates [11]. Therefore, the homogeneity of thick InGaAsN layer on InP was investigated [12].

• Post-growth annealing

In InGaAsN/GaAs-SQW structure it is reported that thermal annealing enhances the migration of nitrogen atoms and makes the spatial distribution of nitrogen homogeneous [8]. Effect of post-growth annealing on thick InGaAsN layers was studied [12].

• Arsenic species

In lattice-matched InGaAs on InP system, it is reported that photoluminescence efficiency was increased and dark currents of pin-PDs became lower by using dimeric molecules of arsenic (As_2) instead of tetrameric molecules (As_4) [13]. Effect of arsenic cracking on InGaAsN was studied [12]. Detailed optical characterization of InGaAsN layers grown using As_2 was also carried out using PL and PR measurements [7].

• Adding antimony

There are many reports about the effects of adding Sb in InGaAsN QWs. It is reported that adding Sb in InGaAsN/GaAs QWs grown on GaAs substrates improves interface quality by suppressing three-dimensional growth [14]. Furthermore, it is reported that increasing Sb composition in the InGaAsSbN QWs grown on InP substrates resulted in red shift of the emission wavelength of laser diodes at 2μm region and a reduction in lasing threshold current density [15]. However, there are few reports about the effects of adding Sb in the thick InGaAsN layers. The effect of adding Sb in 1-μm-thick InGaAsN layers grown on InP was investigated [16, 17].

3.1.1 Growth condition

After the Fe-doped (100) InP substrates were thermally cleaned under As vapor pressure, 0.3μm-thick $In_{0.52}Al_{0.48}As$ buffer layers or 0.15μm-thick InGaAs buffer layers were grown. $In_{0.55}Ga_{0.45}As_{1-x}N_x$ layers (1μm-thick) were followed. The growth temperature was 470ºC. The growth rates of InGaAs(N) and InAlAs layers were 1.45μm/h. The arsenic source was controlled by needle-valve cracking cell, and As_2 or As_4 were used. The As beam intensity was kept constant at 2.2×10^{-3}Pa. The nitrogen was supplied by an ECR plasma source and the nitrogen gas flow rate was

0.7sccm with an ECR power of 5~40W.

3.1.2 Dependence of band gap of thick InGaAsN on N composition

Several InGaAsN layers with different N composition of 0.2~1.1% were grown by varying the ECR power from 5 to 40W using InGaAs buffer layers. As a reference, a single InGaAs layer (i.e. N composition of 0%) was also grown and characterized. Fig. 3.1 shows the PL spectra of the InGaAsN layers and the InGaAs layer measured at 300K. PL peaks of the InGaAsN layers were clearly seen beside those of InGaAs buffer layers. A marked red-shift of the InGaAsN layers was observed with increasing N composition. Moreover, the PL spectral full width half maximum increased with the increase of N composition, which might be due to an increase in composition fluctuation.

To confirm the PL peak energy shift shown in Fig. 3.1, corresponds to the band gap reduction by N introduction, PR measurements were also carried out. Fig. 3.2 shows the PR spectra of the InGaAsN layers and the InGaAs layer measured at 300K. Arrows in the Fig. 3.2 indicate the E_g obtained by fitting the data with the Aspnes third derivative functional form described in Chapter 2. It can be seen that known that the E_g shifts toward lower energy side with increasing N composition. In addition, the PR spectra of the samples with higher N compositions are found to be broader. This result corresponds to the spectral broadening of the PL spectrum shown in Fig. 3.1, and is probably due to the increase in composition fluctuation with the increase of N composition.

Fig. 3.3 shows the comparison of the E_g determined by PR measurement and the PL peak energy. In this figure, open circles are the data for PL and closed squares are those for PR measurements. As is known from the figure, the PL peak position is very close to the E_g obtained by PR measurement, indicating that the observed red-shift of the PL peak is really induced by the change of E_g of the InGaAsN layer.

3.1.3 Depth profile of N

The depth profile of the nitrogen concentration in an InGaAsN layer was measured by SIMS. As shown in Fig.3.4, it was confirmed that the nitrogen concentration is uniform in InGaAsN layer. The nitrogen composition was calculated at approximately 2%.

3.1.4 Post-growth annealing on InGaAsN layers

Rapid thermal annealing (RTA) was applied to the InGaAsN layers grown using As_4 in nitrogen

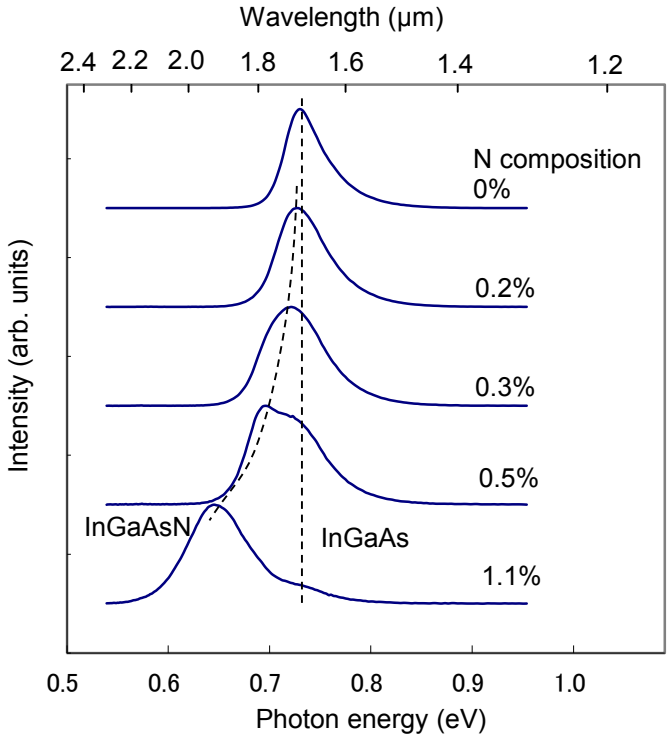

Fig. 3.1 PL spectra of the InGaAsN layers and the InGaAs layer

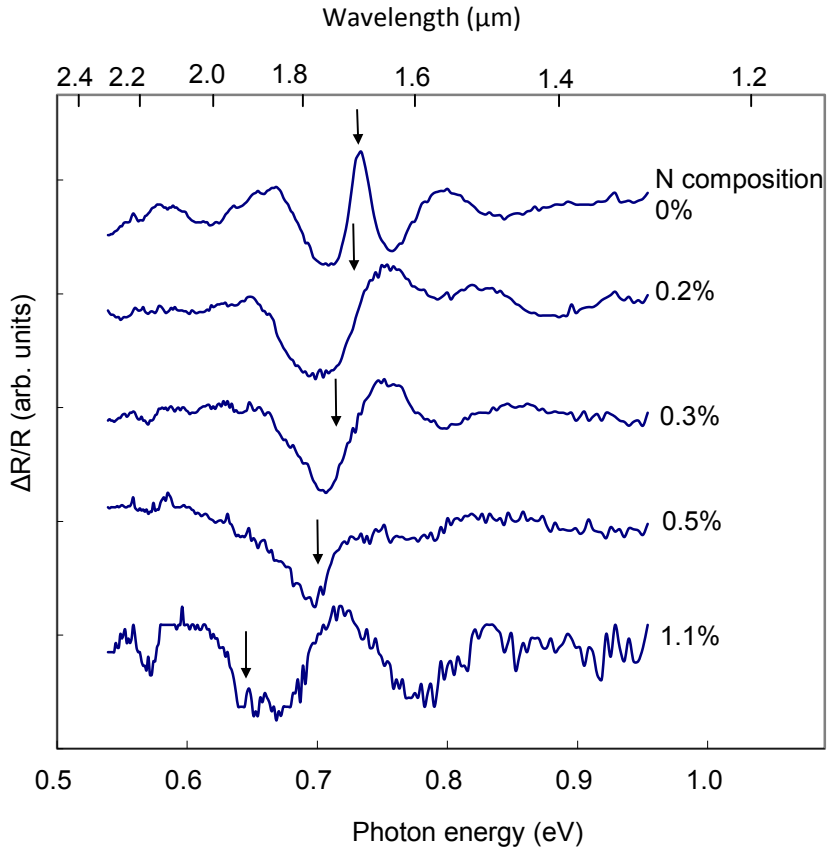

Fig. 3.2 PR spectra of the InGaAsN layers and the InGaAs layer

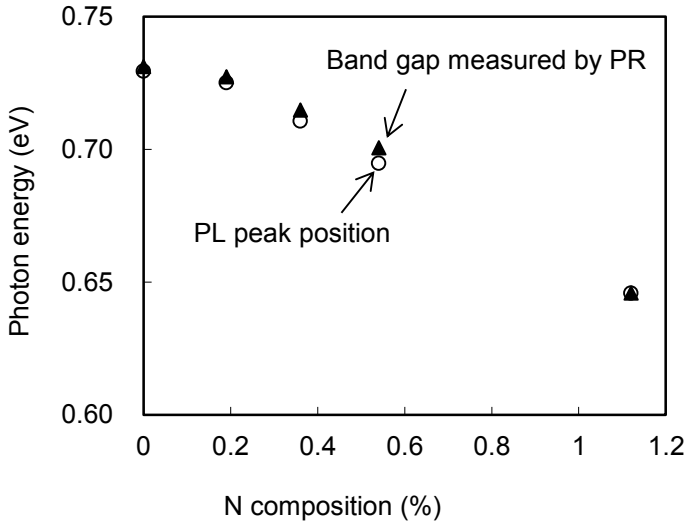

Fig. 3.3 Dependence of PL peak position and band gap measured by PR of InGaAsN layers on N composition

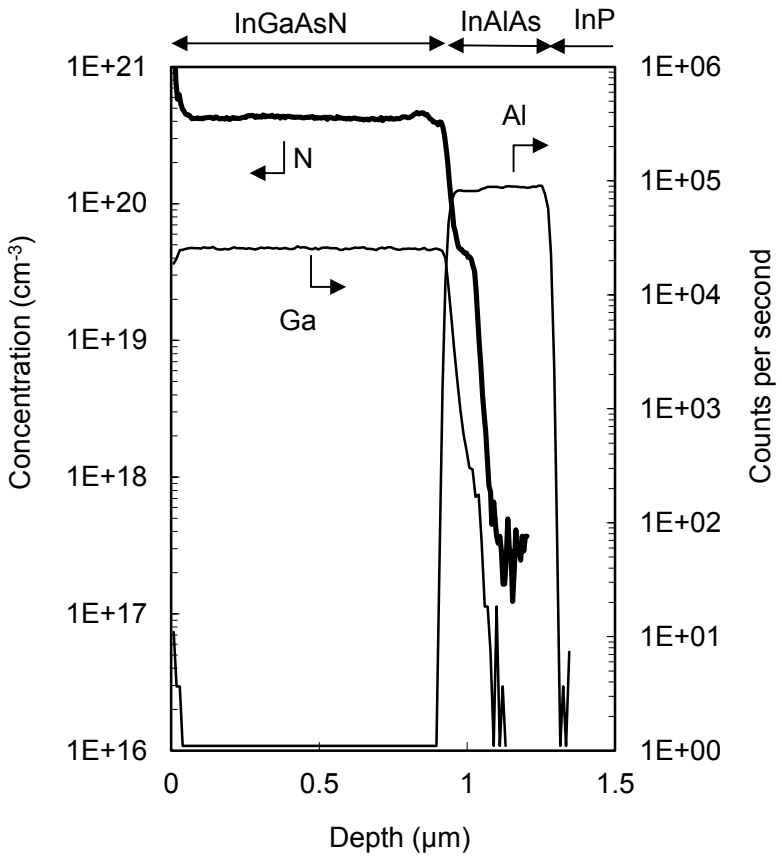

Fig. 3.4 Depth profile of the nitrogen concentration of an InGaAsN layer.

atmosphere. The author focused on annealing temperature and annealing time.

Annealing temperature

In Fig. 3.5, XRCs of InGaAsN layers annealed in different temperatures are shown. The annealing time was fixed to 15sec. The lattice mismatch between InGaAsN layer and InP substrate is approximately -0.20%, which was not changed by annealing. Annealed at 700ºC or lower, the FWHM of XRC of InGaAsN layer becomes narrower than that of the as-grown InGaAsN layer as the annealing temperature becomes higher (Fig. 3.6). On the other hand, at 750ºC the XRC of InGaAsN layer showed no clear diffraction peak. This indicates that the InP substrate was damaged seriously by annealing. These results suggest that the crystalline quality of InGaAsN layer can be improved by annealing at a proper temperature.

Annealing time

Secondly, the effect of annealing time on InGaAsN layers was investigated. XRCs of InGaAsN layers annealed at 600ºC and 650ºC for different time are shown in Fig. 3.7. As shown in Fig. 3.8, the XRC FWHM of InGaAsN layer becomes narrower gradually at both 600ºC and 650ºC as the annealing time becomes longer.

3.1.5 Arsenic species

The crystalline quality of InGaAsN layers grown using As_4 and As_2 were compared. An InGaAsN layer grown using As_2 had good crystalline quality because the XRC FWHM was as narrow as 35.9 arc-sec without annealing (Fig. 3.9). The XRC FWHM was not improved by post-growth annealing at 650ºC for 120sec, which suggests using As_2 suppresses defects which might exist in as-grown InGaAsN layer using As_4 and disappear after post-growth annealing.

The diffraction angle of the InGaAsN layer grown using As_2 is higher than that of the InGaAsN layer using As_4, which means that the lattice constant of the InGaAsN layer using As_2 is smaller.

The absorption spectra of InGaAsN layers using As_2 and As_4 measured at room temperature are shown in Fig. 3.10. Because the absorption edges are not clear in the spectra, the absorption edges were evaluated by the first differential curves of the spectra shown in the inset in Fig. 3.10. The absorption edges of InGaAsN layers using As_2 and As_4 are approximately 1.95μm and 1.80μm, respectively. The red-shift by using As_2 instead of As_4 is due to the increase of nitrogen incorporation, because the lattice constant of InGaAsN layer using As_2 is smaller than that of InGaAsN layer using As_4 as mentioned above.

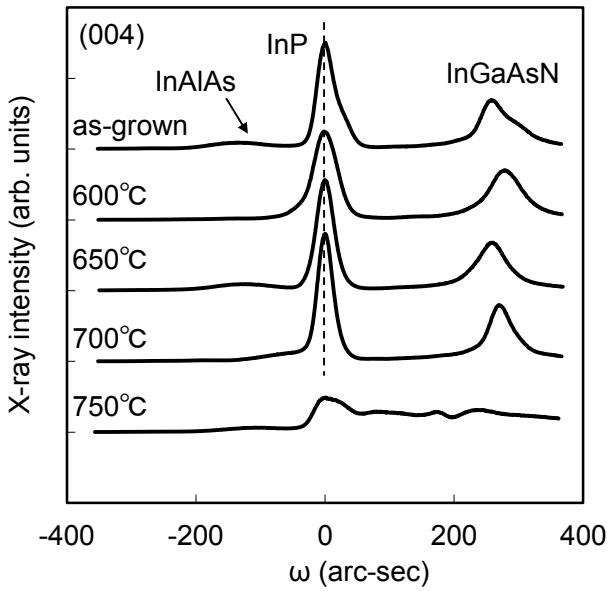

Fig.3.5. XRCs of InGaAsN layers annealed at different temteratures

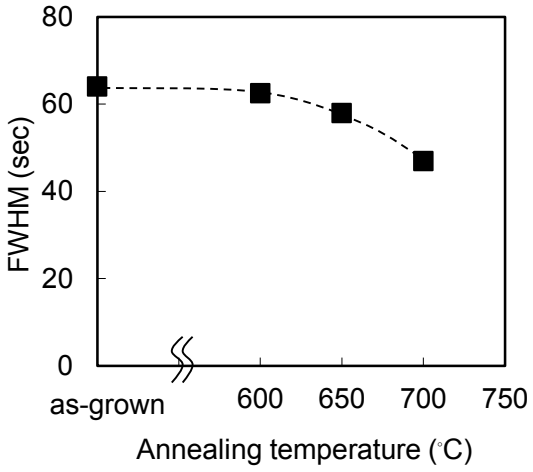

Fig.3.6. XRC FWHMs of InGaAsN layers annealed at different temperatures

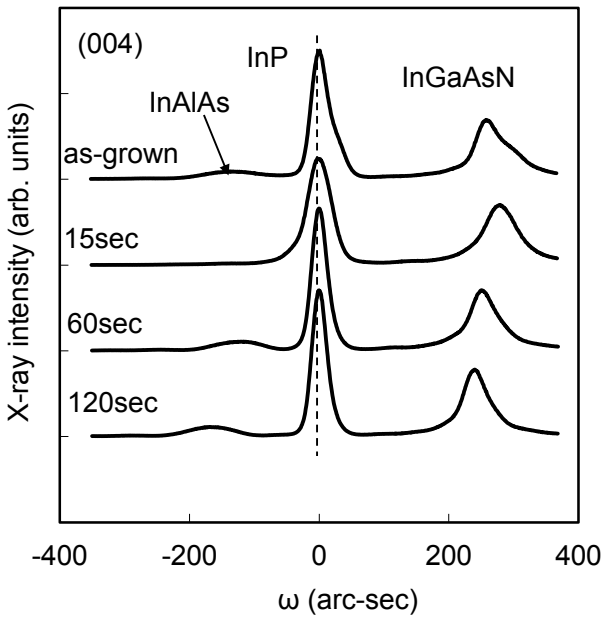

(a) 600ºC

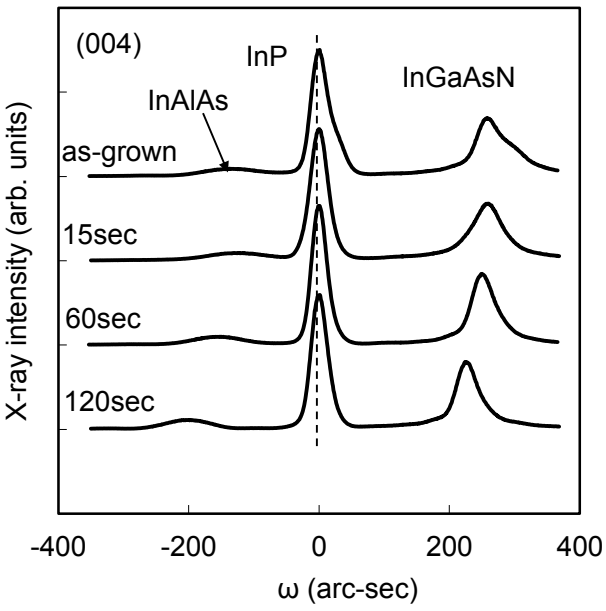

(b) 650ºC

Fig.3.7 XRCs of InGaAsN layers annealed for different time.

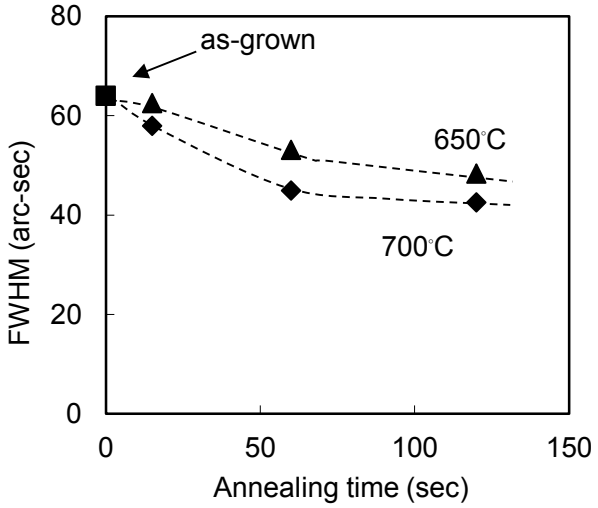

Fig.3.8. XRC FWHM of InGaAsN layers annealed for different time

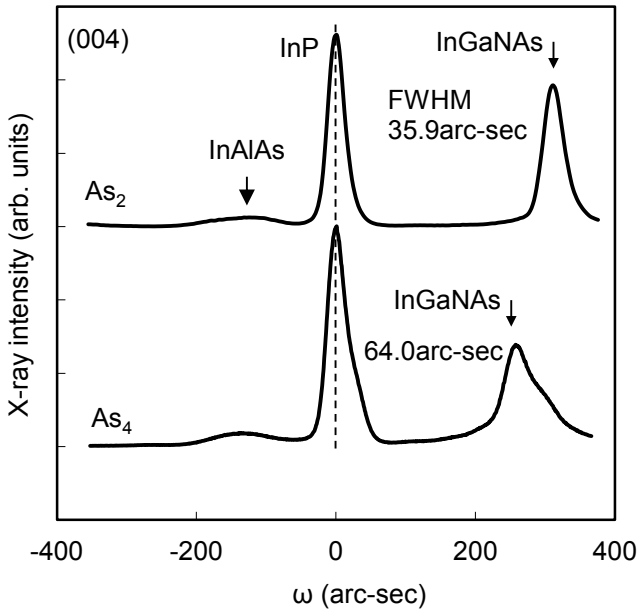

Fig.3.9. XRCs of InGaAsN layer grown using As_2 and As_4

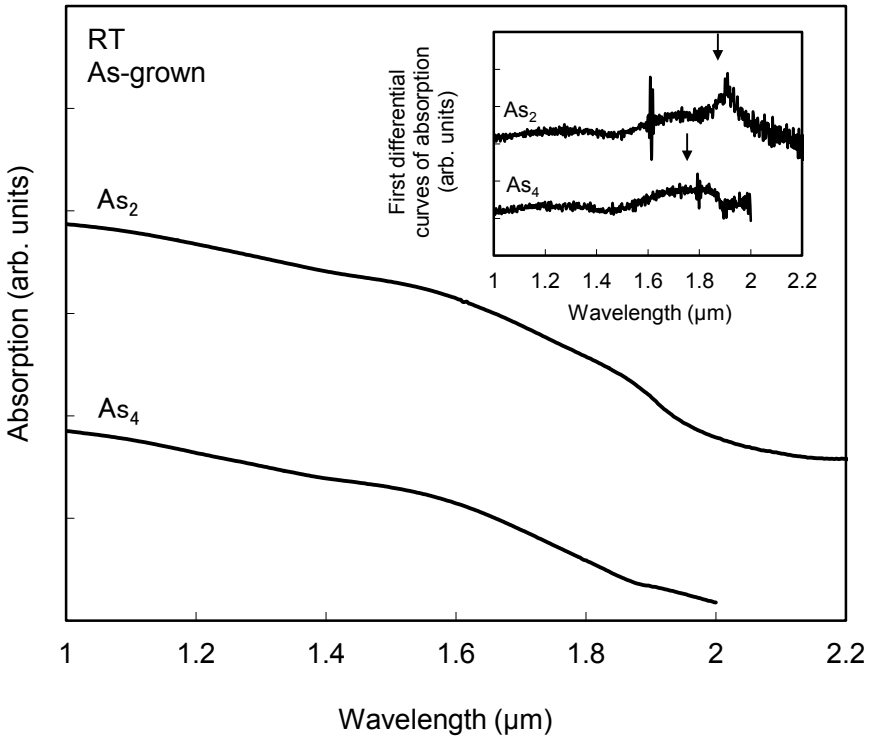

Fig.3.10. Absorption spectra of InGaAsN layers grown using As_2 and As_4.
Inset: First differential curves of the absorption spectra.

Furthermore, the first differential curves of the spectra show that the absorption edge of InGaAsN layer using As_2 is more abrupt than that of InGaAsN layer using As_4, which indicates that the InGaAsN layer using As_2 has a good crystalline quality.

The PL spectra of InGaAsN layer using As_2 and As_4 were measured at room temperature (Fig. 3.11). The spectrum of 2μm-thick InGaAs layer grown directly on an InP substrate is also shown. PL peaks of the InGaAsN layers were observed at room temperature. The PL intensities of the InGaAsN layers are the two thirds as strong as that of the InGaAs layer. Considered that the InGaAsN layers are half as thick as the InGaAs layer, the InGaAsN layers have almost equivalent emission efficiency to that of the InGaAs layer. InGaAsN layers with good crystalline quality were obtained. The emission wavelengths of InGaAsN layers using As_2 and As_4 are approximately 1.91μm and 1.85μm, respectively, which coincide with absorption edges. It is remarkable that the PL intensity of InGaAsN using As_2 became slightly stronger than that of InGaAsN using As_4 although the nitrogen composition increases. This result is contradictory to the fact that the PL intensity of an InGaAsN layer decreased as the nitrogen composition increased [9]. Using As_2 might reduce the nonradiative recombination centers compared with using As_4.

3.1.6 Adding Sb

Growth condition

$In_{0.56}Al_{0.44}As$ buffer layer and $InGaAs_{1-x-y}Sb_xN_y$ layer (x=0, 0.026) were grown on Fe-doped (100) InP substrates. The thickness of the InAlAs buffer layer and the InGaAsSbN layer were 0.24 and 1μm, respectively. The growth temperature was 470ºC. The As source was supplied without cracking. The As flux in the chamber was kept constant at 2.2×10^{-3} Pa. The nitrogen was supplied using the ECR plasma source and the gas flow rate was 0.7 sccm with the power of 40W. Sb were supplied by the effusion cell. The Sb flux was maintained at 1.7×10^{-5} Pa during the $InGaAs_{1-x-y}Sb_xN_y$ layer (x=0, 0.026) growth. The growth rates of InAlAs and InGaAsSbN layers were 1.11 and 1.32μm/h, respectively. After epitaxial growth, the samples were evaluated without post-growth annealing.

Composition measurement of InGaAsSbN

The In compositions of the InGaAsN and InGaAsSbN layers were compared by the Rutherford back scattering (RBS) method in order to confirm that adding Sb does not affect the group-III composition. The In composition of the InGaAsN layer was directly determined to be 54.8±1%. On the other hand, in the case of InGaAsNSb layer, only the total concentration of In and Sb was obtained because Sb could not be distinguished from In. The total concentration of In and Sb was 58.0±1%. As

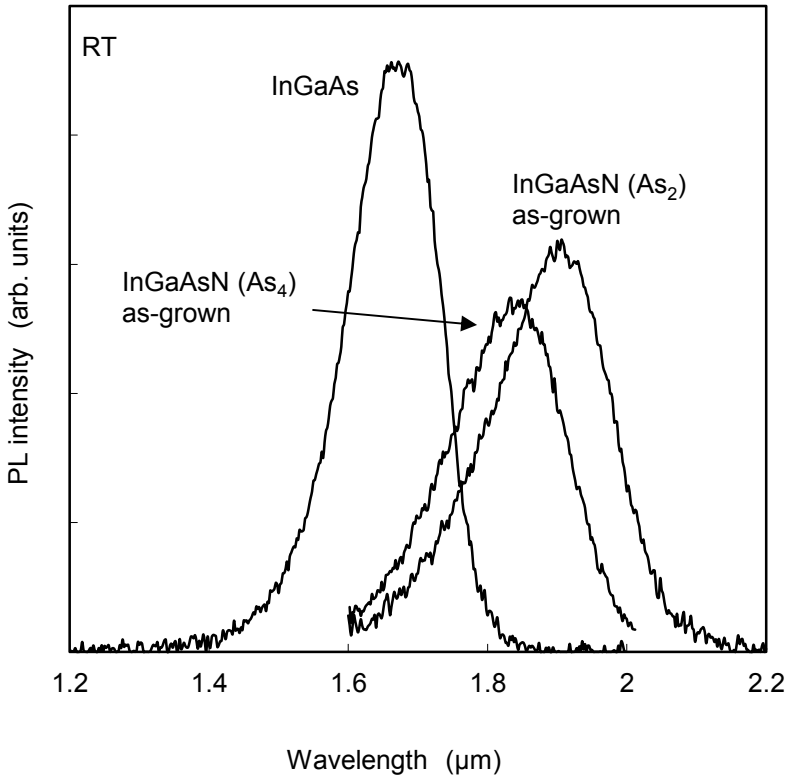

Fig.3.11. PL spectra of InGaAsN layers (grown using As_2 and As_4) and InGaAs layer

mentioned later, the Sb composition of the InGaAsSbN layer was determined to be 2.6% from SIMS analysis. Therefore, the In composition can be estimated at 55.4±1%. It seems that adding Sb does not significantly affect the In composition, because the difference in the In composition is within the margin of error of the RBS measurement.

The depth profile of the nitrogen and the Sb concentration in the InGaAsN and InGaAsNSb layers were measured by SIMS. The depth profiles of N and Sb concentrations in the InGaAsN layer and the InGaAsSbN layer are shown in Figs. 3.12(a) and (b), respectively. To define the epitaxial structures, the depth profiles of Ga and Al are also shown. The nitrogen and Sb concentration are uniform in the growth direction, which shows the MBE growth is performed stably. The nitrogen compositions were estimated at 1.1% and 1.4% in the InGaAsN layer and the InGaAsSbN layer, respectively. The Sb composition of the InGaAsSbN layer was estimated at 2.6%. It can be seen that the InGaAsSbN layer has higher N composition than the InGaAsN layer, because the discrepancy of the N compositions is above the margin of error of the SIMS analysis (approximately ±10%). It seems that the discrepancy of N composition is related with the presence of Sb. It is previously reported that adding Sb enhances incorporation of nitrogen in (In)GaAsN layers grown on GaAs substrates by MBE [18–20]. Although the reason is not clear yet, our data indicate that the same phenomena occurred in the InGaAsSbN layer grown on the InP substrate by MBE method.

Characterization of crystalline quality of InGaAsSbN

Fig. 3.13 shows the XRCs of as-grown InGaAsN and InGaAsSbN layers. The lattice mismatch between the InGaAsN layer and the InP substrate is approximately -0.20%. On the other hand, the lattice mismatch between the InGaAsSbN layer and the InP substrate is approximately -0.15%. The lattice constant became larger because of incorporation of Sb which has larger atomic diameter than N or As. The FWHM of the InGaAsSbN layer became narrower than that of the InGaAsN layer. This result suggests that adding Sb improves the crystallographic quality of the thick InGaAsN layer.

AFM was employed to study the surface quality of the samples. A 2μm-thick lattice-matched InGaAs layer directly grown on InP is also evaluated. Fig. 3.14(b) shows the surface morphology of the InGaAsN layer, which is rough and has oval patterns with the size of several 100 nm. On the other hand, InGaAsSbN layer shows a smoother surface with the same degree as InGaAs layer. The results of surface roughness correspond with the results of the FWHM of XRCs.

The room-temperature PL spectra of as-grown InGaAsN and InGaAsSbN were shown in Fig. 3.15. Both the InGaAsN layer and the InGaAsSbN layer successfully showed the PL emissions at room temperature without thermal annealing. The PL wavelength became longer from 1.85 to 1.96 μm by adding Sb flux. This red shift might be caused by the incorporation of Sb into crystal and/or the

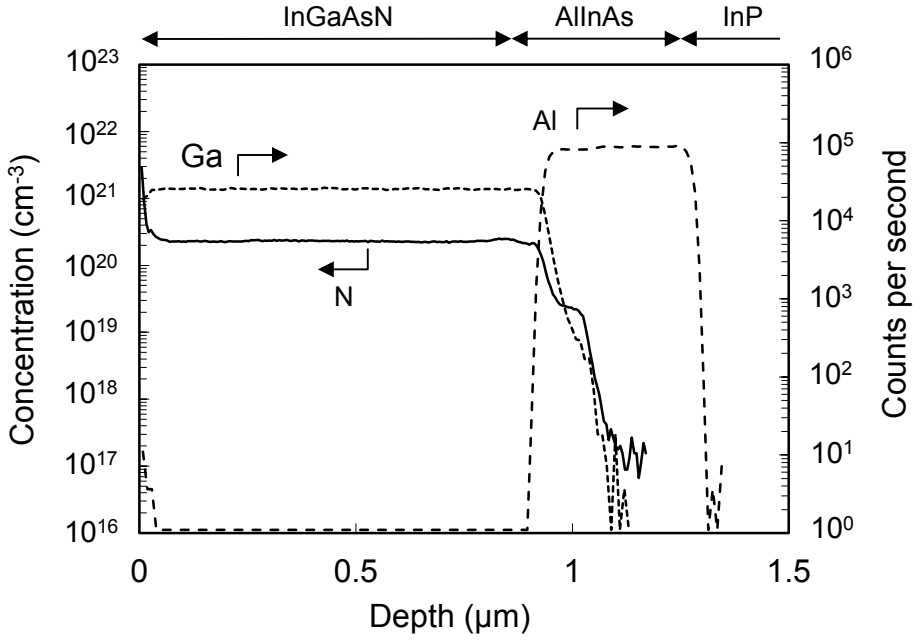

(a) InGaAsN

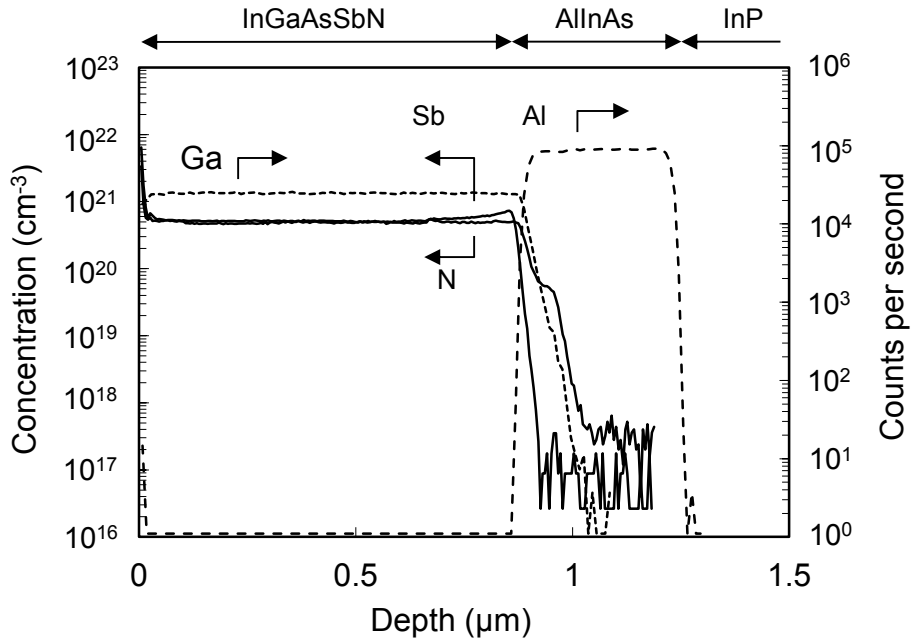

(b) InGaAsSbN

Fig.3.12 Depth profiles of nitrogen and Sb concentration of the InGaAsN layer and the InGaAsSbN layer measured by SIMS

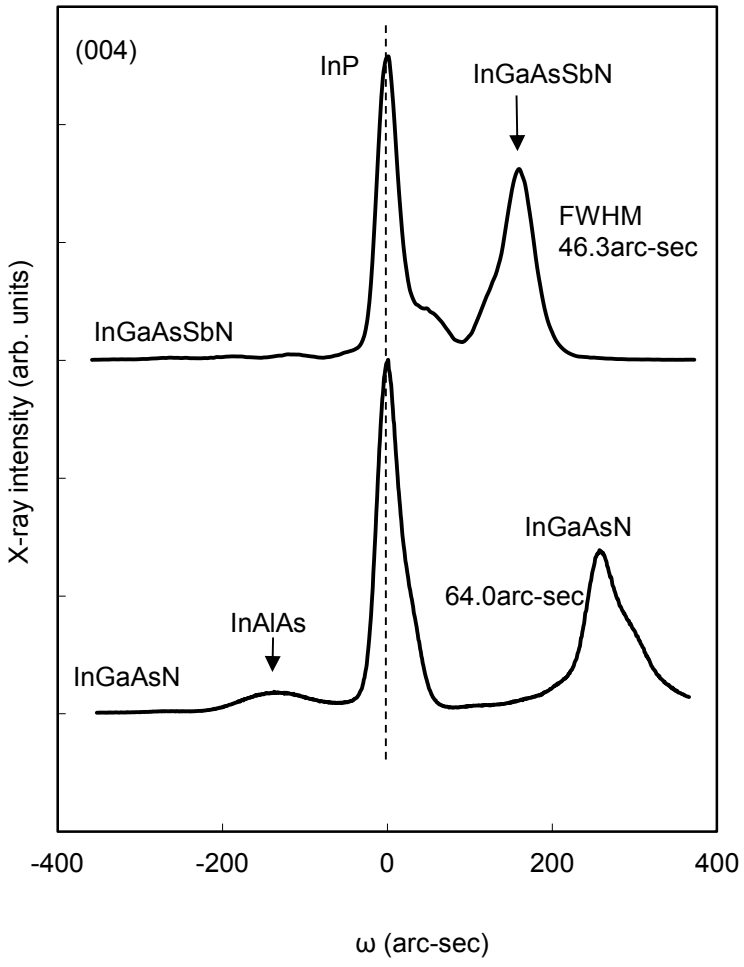

Fig.3.13 XRCs of InGaAsN and InGaAsSbN layers

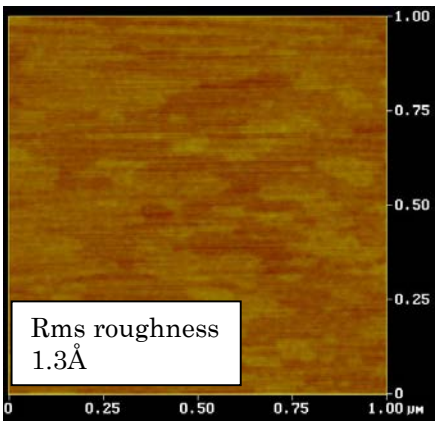

(a)

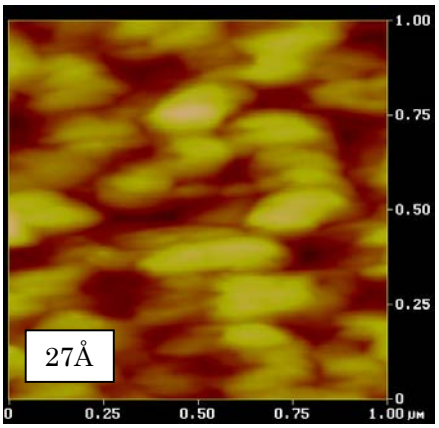

(b)

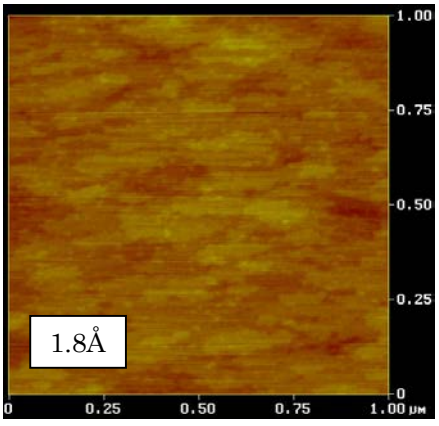

(c)

Fig.3.14 AFM images of the suface morphology of (a) InGaAs, (b) InGaAsN, and (c) InGaAsSbN layers, respectively

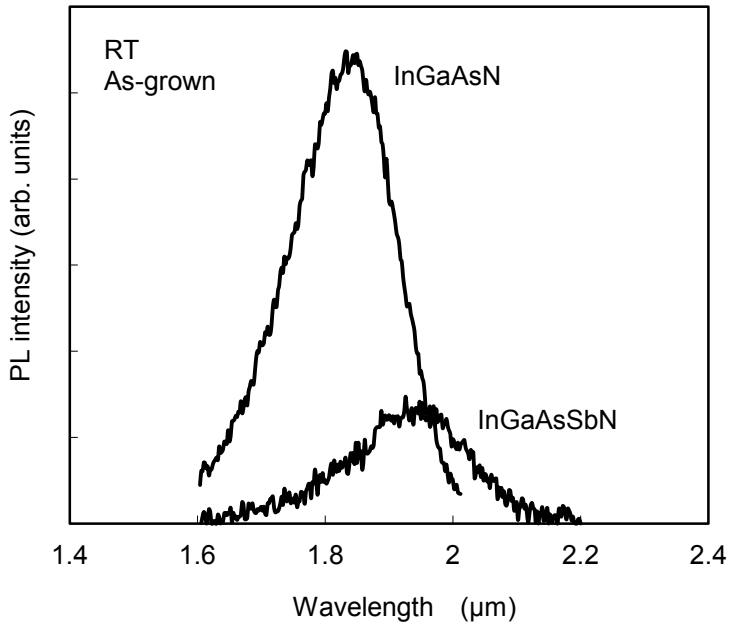

Fig.3.15 PL spectra of InGaAsN and InGaAsSbN layers

increase of nitrogen composition, because the InGaAsN and InGaAsSbN layers have almost same In compositions as mentioned above. The reduction of band gap by adding Sb was confirmed by PR measurement at 300K (Fig. 3.16). On the other hand, the PL intensity of the InGaAsSbN layer decreased by a factor of 5 compared with that of the InGaAsN layer. The degradation of PL intensity by adding Sb is contradictory to the narrowing of FWHM of XRC by adding Sb. The PL intensity of InGaAsN depends on the growth condition such as As flux [21] and growth temperature [22]. The optimum growth condition for optical quality will be changed by adding Sb flux.

Electrical properties were also measured at 77K for both InGaAsSbN and InGaAsN layers using Van der Paw method. Table 3.1 summarizes the obtained results at 77K for both samples. It is clear that the carrier concentration is lower and the electron mobility is higher for the InGaAsSbN layer comparing to those of the InGaAsN layer. These results indicate that electrical properties are also improved by adding Sb atoms.

Table 3.1 Electrical properties of InGaAsSbN and InGaAsN layers at 77K

	InGaAsN	InGaAsSbN
Carrier concentration (cm^{-3})	2.4×10^{17}	2.4×10^{17}
Mobility (cm^2/Vs)	2700	3700

3.2 InGaAsN layers grown using RF plasma cell

In this section, InGaAsN layer growth with the RF plasma cell is described.

3.2.1 Growth condition

$In_{0.57}Ga_{0.43}As$ buffer layer (0.16μm-thick) and $In_{0.57}Ga_{0.43}As_{1-x}N_x$ layer (1μm-thick) were grown on Fe-doped (100) InP substrates. The growth temperature was varied from 461 to 514˚C. Prior to the epitaxial growth, the InP substrate surface was thermally cleaned. At the beginning of InGaAs buffer layer growth, it was confirmed that in-situ RHEED patterns were bright and streak. It indicates that layer by layer growths with smooth surface were proceeding. The growth rates of InGaAsN and InGaAs layers were 1.5μm/h. As_2 was used because the crystalline quality can be improved compared to that of InGaAs layers grown using As_4 as explained in the last section. The As/III flux ratio was varied from 6.6 to 9.8. The nitrogen was supplied using a radio frequency (RF) plasma source and the

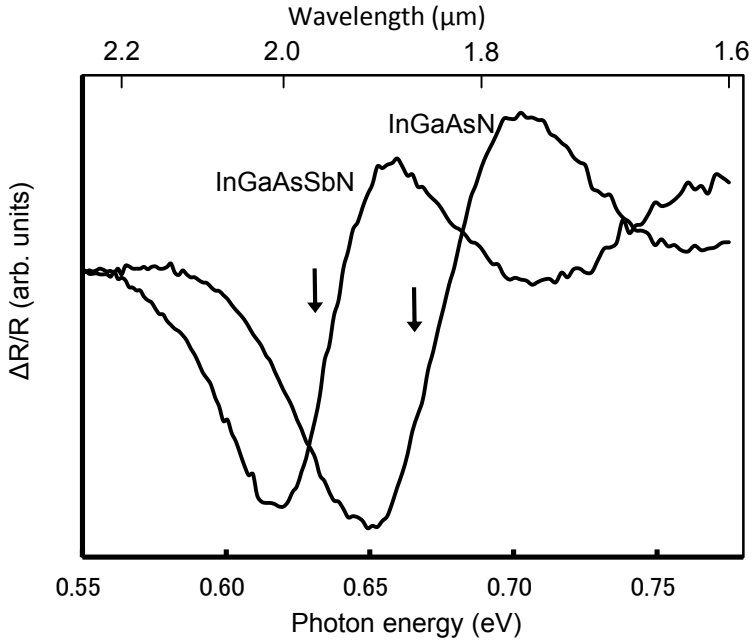

Fig. 3.16 PR spectra of InGaAsSbN and InGaAsN layers measured at 300K

nitrogen gas flow rate was 0.3sccm with an RF power of 90W. After epitaxial growth, the samples were evaluated without thermal annealing.

3.2.2 Optimization of growth temperature

The epitaxial growths were performed at several temperatures with the constant As/III flux ratio of 9.8. Fig. 3.17 shows the dependence of PL wavelength, PL intensity and wavelength corresponding to band bap measured by PR on the growth temperature. The longest PL wavelength (2.01μm) was obtained at 483˚C. The change of PL peak position agreed with band gap measured by PR, indicating that the emission was not induced by defect levels, but by reduction of the band gap energy (i.e. band-edge emission). The PL intensity became strong as the growth temperature increased. The N compositions of the InGaAsN layers measured by SIMS are shown in Table 3.2. At the growth temperature higher than 483˚C, the N composition decreased as the growth temperature increased. It was found that the N incorporation depends on the growth temperature. The shorter PL wavelengths at the higher growth temperatures are due to the decrease of N composition.

The surface images of the InGaAsN layers observed by AFM are shown in Fig. 3.18. While the InGaAsN layers grown at temperatures higher than 483˚C showed relatively smooth surfaces, the InGaAsN layer grown at 461˚C showed much a rough surface. This result is contradictory to the previous reports about InGaAsN/GaAs QWs systems with high In composition which show rough surface morphology at high growth temperatures [23-25]. The reason of rough surface at high growth temperatures is reported as follow; (i) Stranski-Krastanov growth in a lattice-mismatched system, (ii) the effect of local strain derived from the atomic size and ionicity differences in InGaAsN systems [24]. InGaAsN in this study is a lattice-matched system, and Stranski-Krastanov growth was suppressed. Therefore the surface roughness could be improved. Regarding the local strain, the effect is not clear in this study. To clarify the effect, additional investigation may be needed. At lower temperature, it is supposed that the constituent atoms could not migrate enough on the surface, and the surface roughness was enhanced by growing a thicker layer. Fig. 3.19 shows the XRCs of samples grown at different temperatures. The diffraction peak of InGaAsN layer becomes broad at the lower growth temperature. Especially, that of 461˚C-grown sample is very weak and broad, which shows the crystalline quality of InGaAsN grown at 461˚C is poor.

From the viewpoint of optical and crystallographic properties, the lower limit of growth temperature window is about 480˚C. The upper limit is higher than 500˚C.

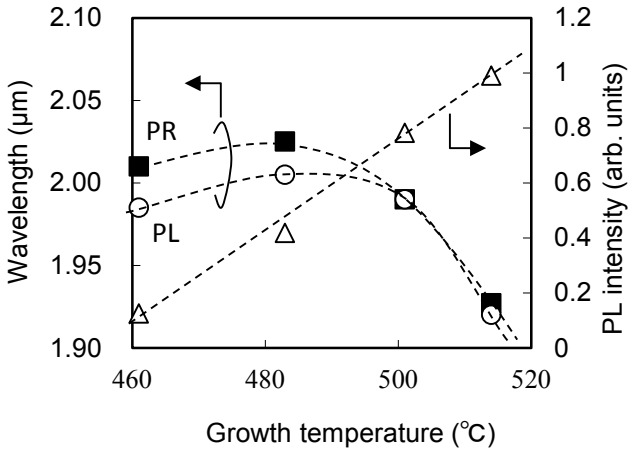

Fig.3.17 PL wavelength, intensity and wavelength corresponding to band gap measured by PR of InGaAsN layers grown at different temperatures with the As/III flux ratio of 9.8.

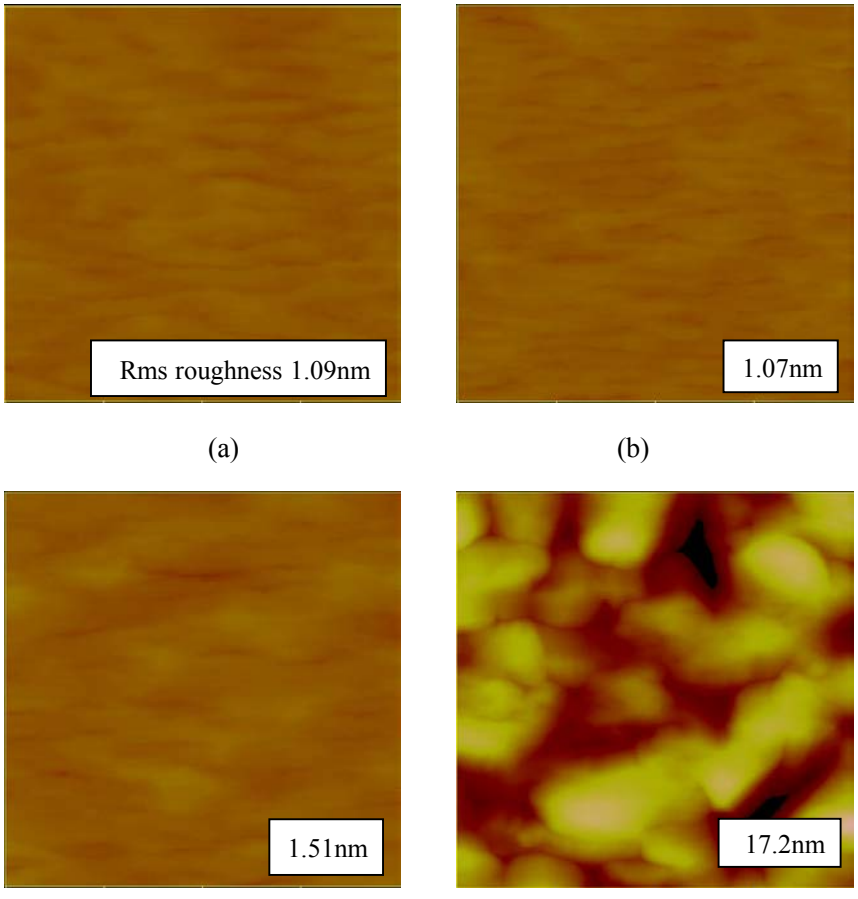

Fig.3.18 AFM images of InGaAsN layers grown at different temperatures at (a) 514˚C, (b) 501˚C, (c) 483˚C and (d) 461˚C, respectively (As/III flux ratio of 9.8).

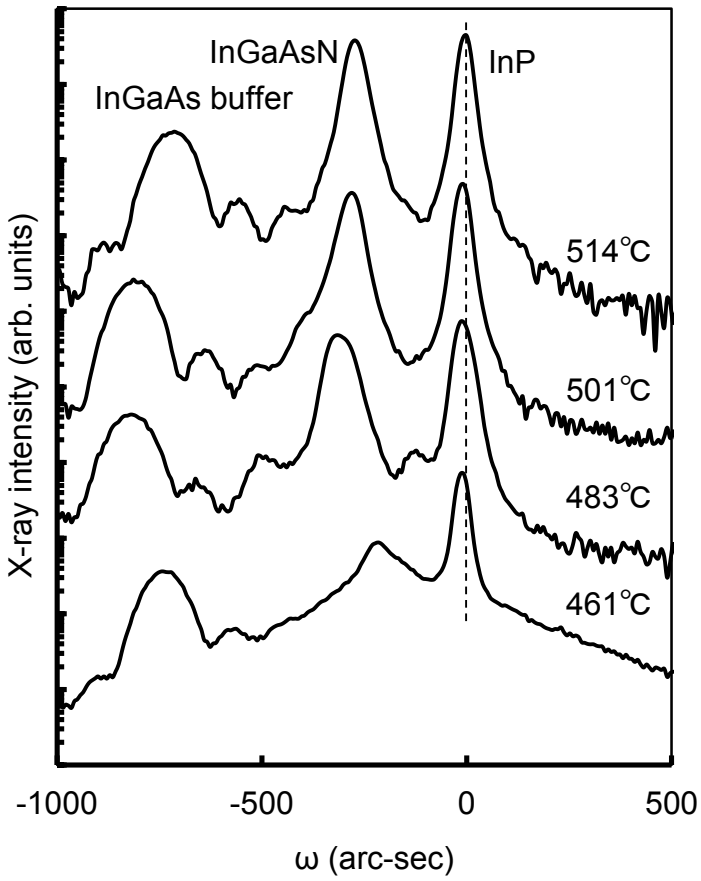

Fig.3.19 XRD curves of InGaAsN layers grown at different temperatures with As/III ratio of 9.8

Table 3.2 N compositions (x) of $In_{0.57}Ga_{0.43}As_{1-x}N_x$ layers grown at several temperatures with the As/III flux ratio of 9.8

Growth temperature (˚C)	N composition (x) (%)
514	1.3
501	1.4
483	1.6
461	1.5

3.2.3 Optimization of As/III flux ratio

InGaAsN layers were grown using the different As/III flux ratios at the growth temperatures of 483 and 501˚C, at which temperatures InGaAsN layers with long PL wavelength and high PL intensity could be obtained. The PL wavelength and intensity are shown in Fig.3.20 (a) and (b), respectively. The PL intensity increased with increasing the As/III flux ratio and the intensity of 501˚C-grown samples are stronger than that of 483˚C-grown samples in the higher As/III flux ratio region. On the other hand, PL wavelength shows the maximum value at the As/III flux ratio of around 8.5 at both growth temperatures. The N concentration by SIMS analysis shows similar As/III-flux-ratio dependence, as shown in Table 3.3. These results show the incorporation of nitrogen into the InGaAsN crystal has the optimum As/III flux ratio. At first, it was supposed that the incorporation of N decreases with increasing the As/III flux ratio, because the coverage of As on the surface decreases the sticking coefficient of N. However, the N concentration decreased not only in the higher As/III flux ratio region but also in the lower region. This tendency was observed at both growth temperatures. This is interesting from the viewpoint of growth mechanism.

Table 3.3 N compositions (x) of $In_{0.57}Ga_{0.43}As_{1-x}N_x$ layers grown at several temperatures with the As/III flux ratio of 9.8.

(a) 483˚C

As/III	N composition (x) (%)
9.8	1.6
8.4	1.9
6.6	1.8

(b) 501˚C

As/III	N composition (x) (%)
9.8	1.4
8.5	1.7
6.7	1.4

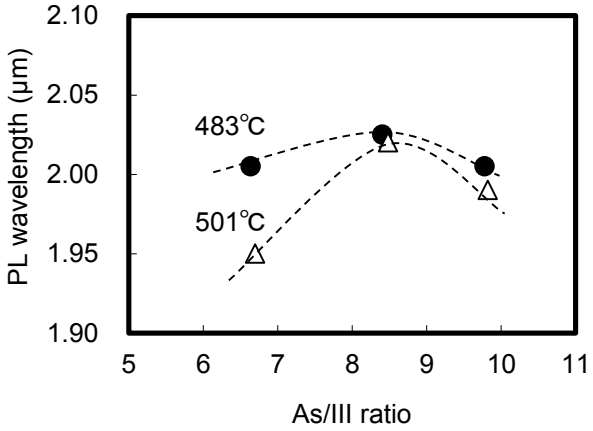

(a) Wavelength

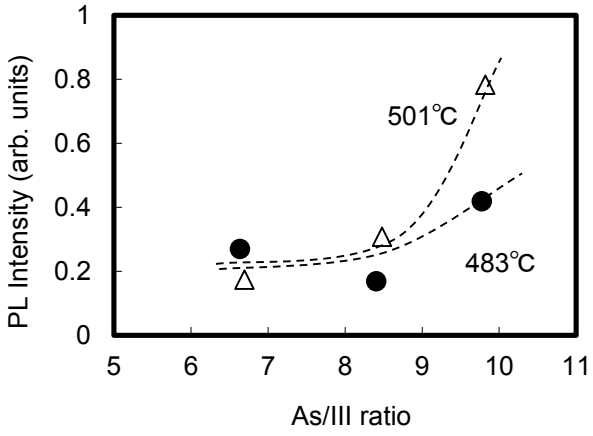

(b) Intensity

Fig.3.20 PL wavelength and intensity of InGaAsN layers grown with different As/III ratios at growth temperatures 483˚C and 501˚C

3.3 Discrete NIR sensors with InGaAsN absorption layers

Although the cutoff wavelength of InGaAsN layer was inadequate, discrete NIR sensors with InGaAsN absorption layers were fabricated and characterized to examine the feasibility of InGaAsN as an absorption layer. As a reference, a sensor with an InGaAs absorption layer was also fabricated.

3.3.1 Fabrication of sensors

N-type InP:S(100) substrates were used because the n-type electrodes were needed on the backside of the substrates. After thermal cleaning of the substrate, 1.5μm-thick $In_{0.53}Ga_{0.47}As$:Si buffer layer, 2.5μm-thick $In_{0.53}Ga_{0.47}As_{1-x}N_x$ absorption layer, $In_{0.53}Ga_{0.47}As$ cap layer were grown. Then 0.8μm-thick InP window layer was re-grown by MOVPE method. As a reference, a sensor with InGaAs absorption layer was also fabricated.

The N supplying conditions and characteristics (N composition measured by SIMS and PL wavelength measured at 300K) of the absorption layers are summarized in Table 3.4. Sample A and the reference with InGaAs absorption layer are grown using As_4. The other samples are grown using As_2.

Sensors were fabricated by processing the 5 epi-wafers. The details of the process are described in Chapter 2.

Table 3.4 Nitrogen supplying conditions of InGaAsN absorption layers

	Plasma cell	Nitrogen gas flow (sccm)	Plasma power (W)	Nitrogen composition	PL wavelength (μm)
Sample A	ECR	1.5	50	1.3	1.823
Sample B	RF	0.3	80	1.4	1.841
Sample C	RF	0.3	90	1.5	1.863
Sample D	RF	0.3	90	1.6	1.874

3.3.2 Current-voltage characteristics

The current-voltage characteristics of the five sensors were measured at room temperature (Fig. 3.21). The sensors with InGaAsN absorption layers exhibited much higher dark current densities than the sensor with InGaAs absorption layer.

Dark current density (Vr=-1V) increased over-exponentially with increasing PL wavelength (Fig. 3.22). This might be due to defects introduced in the InGaAsN layers accompanied to the incorporation of N. Even higher N composition is necessary because the cutoff wavelength of the InGaAsN absorption layer should be extended further. However, it would cause still more dark current. It is thought that applying InGaAsN to sensor absorption layer is extremely difficult because the dark current should be reduced by several orders of magnitude.

3.4 Summary

The results in this chapter are summarized below;

• It was experimentally confirmed that band gap of thick InGaAsN layers decreased with higher N composition.

• Thick InGaAsN layers were grown by MBE method on InP substrates. The N composition in an InGaAsN layer was confirmed to be uniform.

• The crystalline quality of thick InGaAsN layer can be improved by post-growth annealing in a proper temperature.

• Using As_2 instead of As_4 during growth also improves the crystalline quality of InGaAsN layer.

• Adding Sb flux improved the crystallographic quality and surface morphology of InGaAsN layers. PL wavelength became longer by adding Sb flux.

• By optimizing growth temperature and As/III flux ratio, the author obtained the thick InGaAsN layer which show PL emission with wavelength as long as 2.03μm at room temperature.

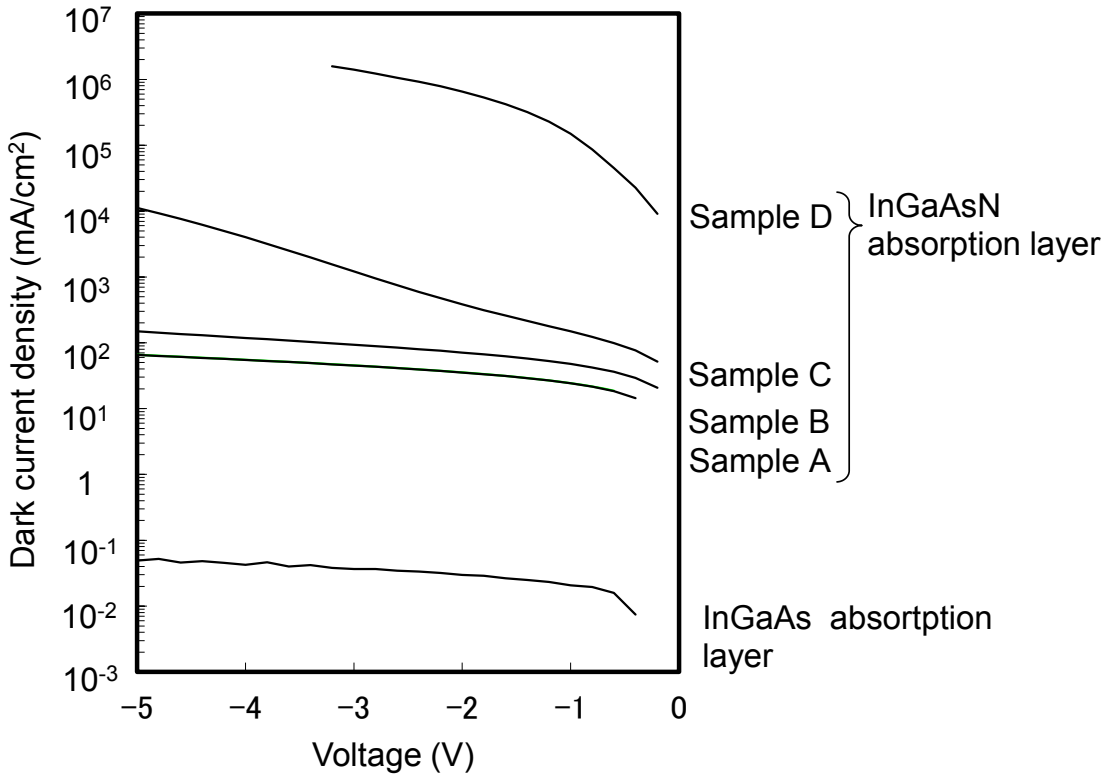

Fig.3.21 Current-voltage characteristics of the discrete NIR sensors with InGaAsN absorption layers

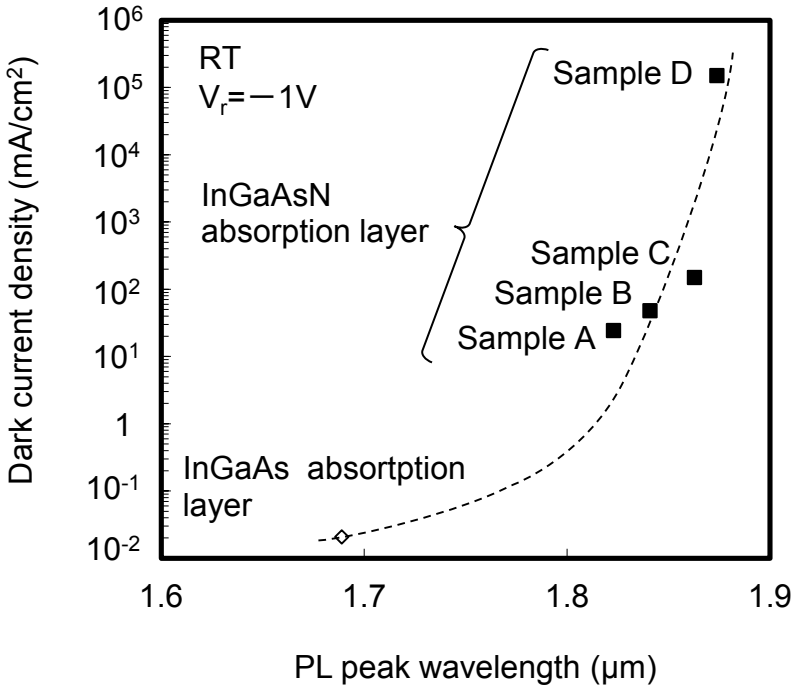

Fig.3.22 Dependence of dark current on PL wavelength of the discrete NIR sensors with InGaAsN absorption layers

• Sensors with InGaAsN absorption layers with PL wavelength of ~1.9μm exhibited much higher dark current compared with that with an InGaAs absorption layers. Moreover, the dark current tended to increase with increasing PL wavelength of the absorption layer.

The author concludes that utilizing InGaAsN for NIR sensors is difficult, although several academic discoveries have been achieved.

References

[1] Y. Kawamura, T. Nakagawa, N. Inoue, Jpn. J. of Appl. Phys., Vol. 44, No. 8, 6000 (2005)

[2] Y. Kawamura, T. Nakagawa, N. Inoue, Jpn. J. of Appl. Phys., Vol. 44, No. 35, L1112 (2005)

[3] Y. Kawamura, T. Nakagawa, N. Inoue, Jpn. J. of Appl. Phys., Vol. 45, No 4B, 3453 (2006)

[4] Y. Kawamura, N. Inoue, Jpn. J. of Appl. Phys., Vol. 46, 3380 (2007)

[5] R. J. Molnar, T. D. Moustakas, J. of Appl. Phys., Vol. 76, 4587 (1994)

[6] K.Miura, Y.Nagai, Y.Iguchi, M. Tsubokura, H.Okada, Y.Kawamura, Proc. of International Conference on Indium Phosphide and Related Materials, 376 (2007)

[7] M. Yoshikawa, K.Miura, Y.Iguchi, Y.Kawamura, J. of Cryst. Growth, Vol. 311, 1745 (2009)

[8] T. Yamada, T. Ishizuka, A. Sawamura, T. Iguchi, T. Saito, T. Katsuyama, S. Takagishi, K. Nomura, M. Nakayama, Proc. of International Conference on Indium Phosphide and Related Materials, 36 (2004)

[9] D. Litvinof, D. Gerthsen, A. Rosenauer, M. Hetterich, A. Grau, Ph. Gilet, and Grenouillet, Appl. Phys. Lett., Vol. 85, 3743 (2004)

[10] H. A. McKay, R. M. Feenstra, T. Schmidtling, U. W. Pohl, and J. F. Geisz, J. Vac. Sci. Technol. B, Vol. 19, 1644 (2001)

[11] A. Ubukata, J. Dong, K. Matsumoto, Y. Ishihara, Jpn. J. Appl. Phys., Vol. 39, 5962 (2000)

[12] K.Miura, Y.Nagai, Y.Iguchi, H.Okada, Y.Kawamura, Proc. of International Conference on Indium Phosphide and Related Materials, 420 (2006)

[13] D. Heut, M. Lambert, D. Bonnevie, D. Dufresne, J. Vac. Sci. Technol. B, Vol. 3, 823 (1985)

[14] X. Yang, J.B. He´roux, L.F. Mei, W.I. Wang, Appl. Phys. Lett., Vol. 78, 4068 (2001)

[15] Y. Kawamura, T. Nakagawa, N. Inoue, Jpn. J. Appl. Phys., Vol. 44, 6000 (2005)

[16] K. Miura, Y. Nagai, Y. Iguchi, H. Okada, Y. Kawamura, J. of Cryst. Growth, Vol. 301-302, 575 (2007)

[17] M. Yoshikawa, K. Miura, Y. Iguchi and Y. Kawamura, Physica Status Solidi C, Vol. 8, 390 (2011)

[18] H.B. Yuen, S.R. Bank, M.A. Wistey, J.S. Harris, J. Appl. Phys., Vol. 96, 6375 (2004)

[19] J.C. Harmand, G. Ungaro, L. Largeau, G.L. Roux, Appl. Phys. Lett., Vol. 77, 2482 (2000)

[20] K. Volz, V. Gambin, W. Ha, M.A. Wistey, H. Yuen, S. Bank, J.S. Harris, J. Crystal Growth, Vol. 251, 360 (2003)

[21] J. Miguel-Sanchez, M. Hopkinson, M. Gutierrez, P. Navaretti, H.Y. Liu, A. Guzman, J.M. Ulloa, A. Hierro, E. Munoz, J. Crystal Growth, Vol. 62, 270 (2004)

[22] T. Kitatani, M. Kondow, K. Nakahara, M.C. Larson, Y. Yazawa, M. Okai, K. Uomi, J. Crystal Growth, Vol. 201/202, 351 (1999)

[23] L. Geelhaar, M. Galluppi, G. Jaschke, R. Averbeck, H. Riechert, T. Remmele, M. Albrecht, M. Dworzak, R. Hildebrant, and A. Hoffmann, Appl. Phys. Lett., Vol. 88, 011903 (2006)

[24] J.-M. Chauveau, A. Trampert, K. H. Ploog, M.-A. Pinault, and E. Tournié, Appl. Phys. Lett., Vol. 82, 3451 (2003)

[25] A. Hierro, J. -M. Ulloa, J.-M. Chauveau, A. Trampert, A. Trampert, M.-A. Pinault, E. Tournié, A. Guzmán, J. L. Sánchez-Rojas, and E. Calleja, J. Appl. Phys., Vol. 94, 2319 (2003)

Chapter 4 Growth and characterization of type-II InGaAs/GaAsSb superlattices for near-infrared sensors

4.1 Introduction

In this chapter, the growth technology of type-II InGaAs/GaAsSb SLs is described. The study was processed as follows;

• Optimization of GaAsSb growth condition

As described in Chapter 1, growth technology of GaAsSb is not matured yet. So the author focused on growth condition of GaAsSb firstly. GaAsSb single layers grown at different conditions were characterized [1].

• Fabrication of sensors with GaAsSb absorption layer

To confirm the advantage of optimized GaAsSb for absorption layer, discrete sensors with GaAsSb absorption layers grown at different conditions were fabricated. The mechanism of the dark currents of the sensors were compared by investigating dependence on temperature [2].

• Growth of type-II InGaAs/GaAsSb SL

Type-II InGaAs/GaAsSb SLs were grown using GaAsSb grown at the optimum condition. Detailed PL measurements were performed to investigate radiative transition process [1].

• Fabrication of NIR discrete sensors with type-II InGaAs/GaAsSb SL absorption layers

NIR discrete sensors with type-II InGaAs/GaAsSb SL absorption layers were fabricated. Electrical properties (current-voltage characteristics and responsivity spectra) of the sensors were evaluated [3].

• Demonstration of NIR FPA with type-II InGaAs/GaAsSb SL absorption layers

Finally, FPA using type-II InGaAs/GaAsSb SL absorption layer was fabricated and demonstrated

[3].

• Growth and characterization of strain-compensated type-II InGaAs/GaAsSb SL

In order to confirm the further potential of type-II InGaAs/GaAsSb SL, strain-compensated type-II InGaAs/GaAsSb SL was grown and characterized. It was experimentally tested whether the band gap can be reduced without deterioration of crystalline quality [4].

4.2 Optimization of GaAsSb growth condition

4.2.1 Growth condition

The author focused on growth temperature and V/III flux ratio. GaAsSb single layers lattice-matched to InP substrates were grown and characterized. As and Sb sources were controlled by needle-valve cracking cells, and As_4 and Sb_1 were used for growth. After Fe-doped (100) InP substrates were thermally cleaned, 0.2μm-thick $Al_{0.48}In_{0.52}As$ buffer layers and 1μm-thick $GaAs_{0.51}Sb_{0.49}$ layers were grown. The growth rates were 1.5 and 0.8μm/h for AlInAs and GaAsSb layers, respectively. The growth temperature was changed in the range from 450 to 520˚C. The V/III flux ratio for GaAsSb growth was changed between 12 and 42. Sb composition is affected by growth temperature and V/III flux ratio as Chang et al. previously reported [5]. Therefore, the Sb/As flux ratio was adjusted in the range from 0.06 to 0.24 in order to obtain GaAsSb lattice-matched to the InP substrate at each growth condition.

4.2.2 XRCs of GaAsSb layers

Results of ω-2θ XRD measurement of GaAsSb layers grown at different conditions are shown in Fig. 4.1. All of the GaAsSb layers grown at 480˚C showed single diffraction peaks, indicating uniform distribution of As and Sb. On the contrary, at least one specimen grown at 450˚C showed a split peak, indicating that the GaAsSb layers are separated into two phases, slightly Sb-rich and As-rich regions. The GaAsSb layer grown at the higher growth temperature (520˚C) also showed a split diffraction peak, which is consistent with the previous report [6]. Phase separation seems to occur out of narrow growth temperature window. Miyoshi et al have previously reported phase separation in InAsSb layer consisting of two alternating plates of InAs-rich and InSb-rich regions grown at low temperature by MBE [6]. Similar phenomenon might occur in the GaAsSb grown at low temperature (450˚C). These

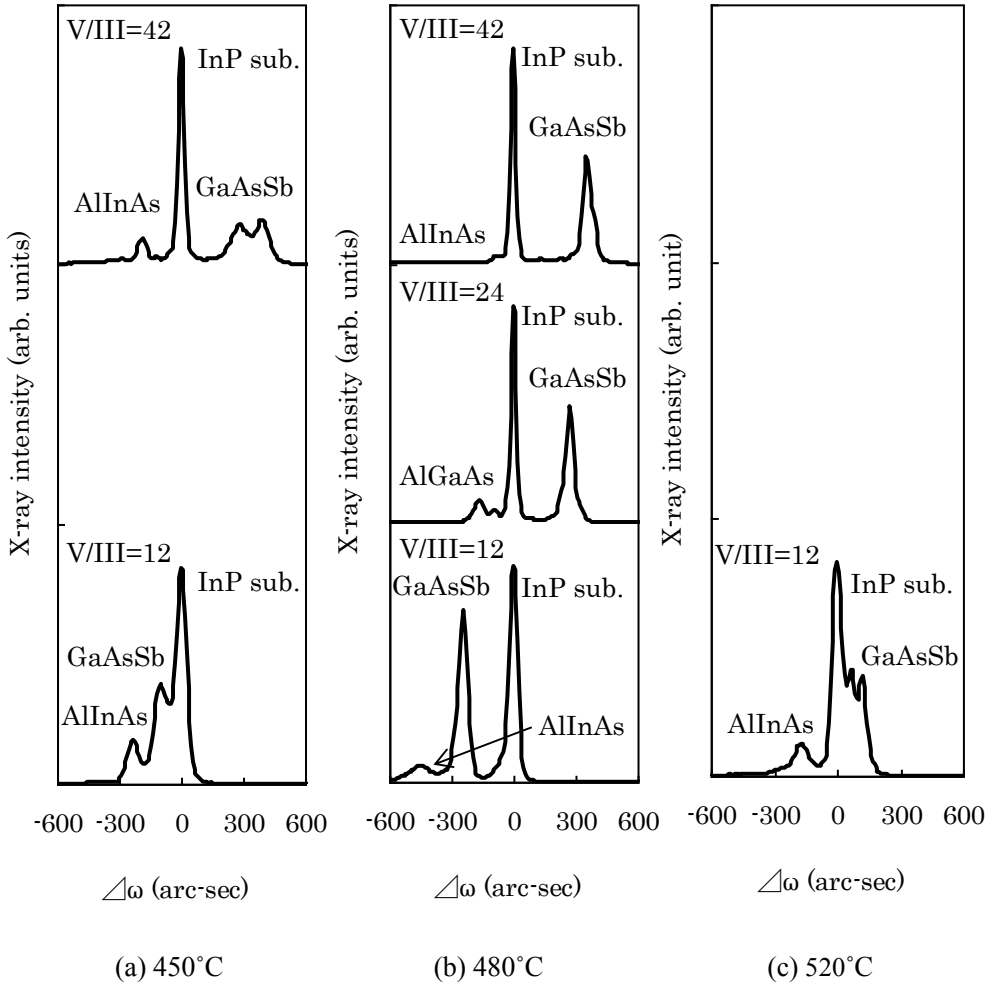

Fig. 4.1 XRCs of GaAsSb layers grown at different temperature

results indicate that growth temperature influences distribution of As and Sb in GaAsSb layer. It was found that GaAsSb layers with single peaks in XRD can be obtained within the narrow growth temperature even if the layers are as thick as 1μm.

Influence of V/III flux ratio on crystalline quality was also examined. The GaAsSb grown at V/III flux ratio 24 showed the narrowest diffraction peak in XRD measurement, suggesting good crystalline quality (Fig. 4.2).

4.2.3 PL measurement of GaAsSb layers

PL measurements at room temperature of GaAsSb layers grown at 480˚C were performed. A typical PL spectrum is shown in Fig. 4.3. Fig. 4.4 shows dependence of PL intensity and FWHM of GaAsSb layers on V/III flux ratio. As Inada et al. reported previously, PL intensity seems to saturate in the region of V/III flux ratio more than 24 [1, 2]. Defects which act as non-radiative recombination centers might be suppressed under sufficient V/III flux ratio. Moreover, the PL peak of the GaAsSb layer grown at V/III flux ratio 24 showed the narrowest FWHM.

From the results of XRD and PL, V/III flux ratio of 24 seems to be optimum. Nakata et al previously reported that lower V/III flux ratio was preferable [8], which is not consistent to our result. The contradiction might be derived from difference of Sb species used for growth.

4.3 Discrete sensors with GaAsSb absorption layers

4.3.1 Fabrication of sensors

Discrete sensors with GaAsSb absorption layers were fabricated to evaluate the crystalline quality of GaAsSb. Si-doped InGaAs buffer layer (1.5μm), undoped GaAsSb absorption layer (2.5μm) and undoped InGaAs cap layer (1.5μm) were grown on S-doped InP (100). The growth rate of InGaAs layer was 1.8μm/h and the V/III flux ratio of it was 10.

Two kinds of GaAsSb absorption layers were compared. One GaAsSb absorption layer was grown at 480˚C and V/III flux ratio 24, which is the optimized condition. The other was grown at 480˚C and V/III flux ratio 12, which is lower than the optimized value.

Details of device process are described in Chapter 2. The structure of the sensors is same as that shown in Fig. 2.10, except for the absence of InP window layers.

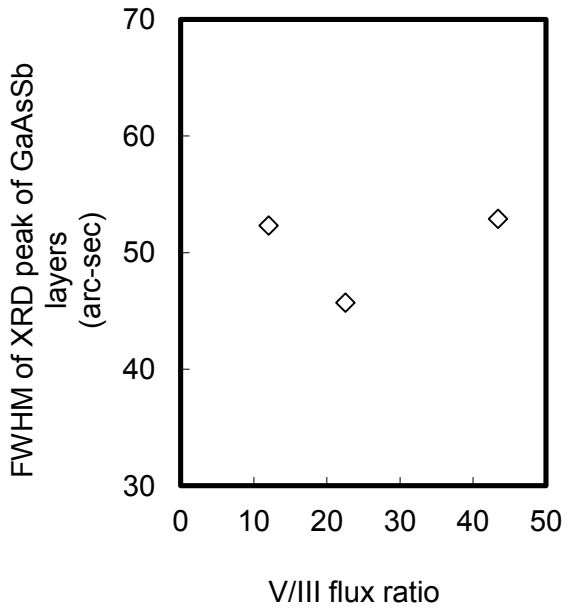

Fig. 4.2 Dependence of FWHM of ω-2θ XRD peaks of GaAsSb layers grown at 480˚C on V/III flux ratio

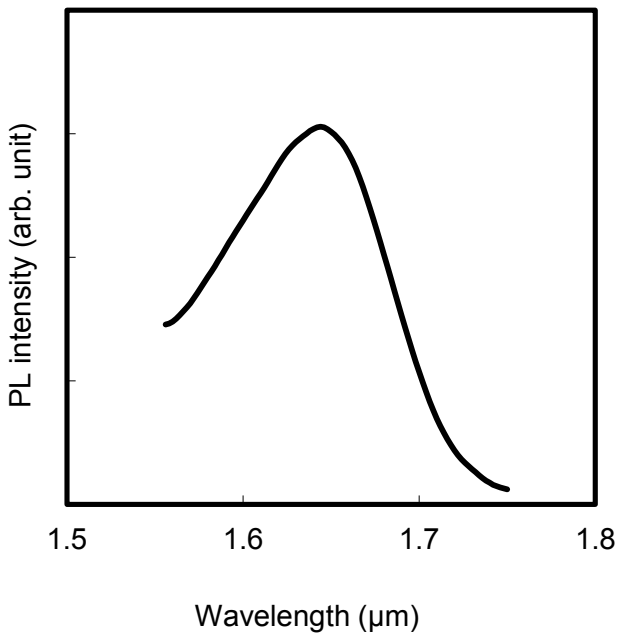

Fig. 4.3 Typical PL spectrum of GaAsSb single layer

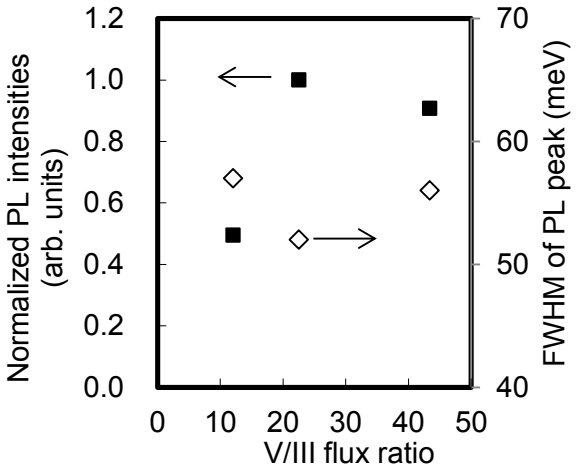

Fig. 4.4 Dependence of PL intensites and FWHM of GaAsSb layers on V/III flux ratio

4.3.2 Temperature dependence of dark currents

Temperature dependence of dark current of the sensors measured at reverse voltage of -1V is shown in Fig.4.5. By growing GaAsSb at higher V/III flux ratio, the dark current was suppressed by approximately two orders compared to the sensor with GaAsSb grown at lower V/III flux ratio, suggesting that V/III flux ratio of GaAsSb layers affects electrical characteristics of sensors seriously. The factor n of the sensors was calculated from the temperature dependence of dark current following the equation below [3];

$$I_{\mathrm{d}} \propto \exp\left(-\frac{E_{\mathrm{g}}}{nkT}\right) \tag{4.1}$$

where E_{g}, k and T stand for band gap of the absorption layer, Boltzmann constant, temperature, respectively. As the factor n approaches unity, the generation-recombination process is suppressed [3]. The factors n were 2.8 and 1.3 for the samples grown at V/III flux ratio 12 and 24, respectively. Decreasing dark current and the reduction of factor n mean better crystalline quality of GaAsSb.

4.4 Growth of type-II InGaAs/GaAsSb SLs

In this section, results of growth and characterization of type-II InGaAs/GaAsSb SLs are described.

4.4.1 Growth condition

A type-II InGaAs/GaAsSb SL lattice-matched to InP was grown using GaAsSb at the optimized condition (growth temperature of 480˚C and V/III flux ratio of 24) on a S-doped (100) InP substrate and characterized. InGaAs was grown with the V/III flux ratio of 10 at the same temperature of GaAsSb growth. The V/III flux ratio of InGaAs was optimized in the past and it was experimentally confirmed that the growth temperature affected the crystalline quality of InGaAs little within the range in this study. The growth rate was 1.7μm/h. The SL consisted of 30 pairs of 5nm-thick InGaAs and 5nm-thick GaAsSb.

4.4.2 Optical property of type-II InGaAs/GaAsSb SL

The PL spectra of the SL measured at 4K with several excitation power densities are shown in Fig. 4.6 Slight blueshift was observed at higher excitation power density. This is derived from Coulomb

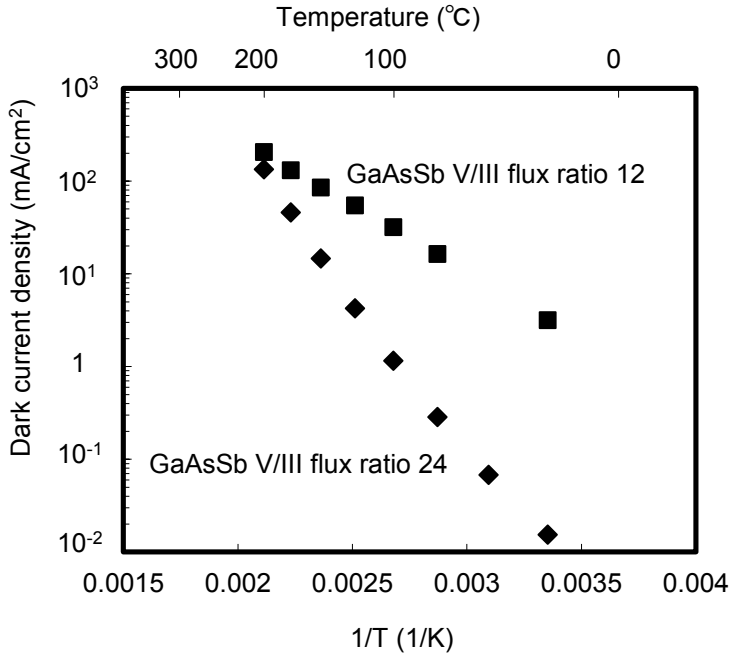

Fig. 4.5 Temperature dependence of dark current densities of sensors with GaAsSb absorption layers measured at room temperature

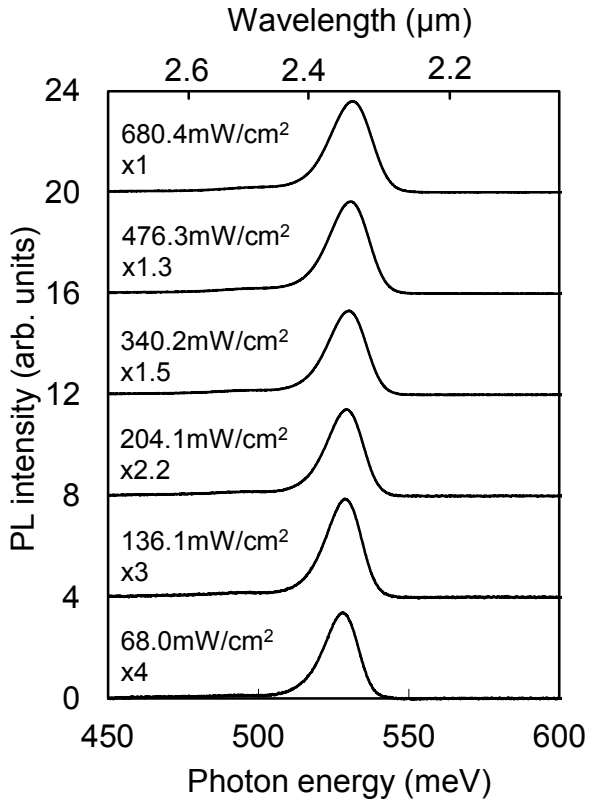

Fig. 4.6 PL spectra at different excitation power densities

interaction between photo-generated electrons and holes spatially separated, which has been discussed in other type-II material systems, GaAs/GaSb and GaAs/GaAsSb [9, 10]. Attracted carriers form approximately triangular wells near the interfaces (Fig. 4.7). The electron density n_{W} and hole density p_{W} generated in the thin layer region by a photon flux I are expressed by the relation;

$$n_{\mathrm{W}} p_{\mathrm{W}} = {n_{\mathrm{W}}}^2 = \frac{\alpha I (L + l)}{\gamma} \tag{4.2}$$

where α, L, l and γ denote the absorption coefficient, the width of GaAsSb, the width of InGaAs and the radiative recombination coefficient. The strongly localized electrons near the InGaAs/GaAsSb interface form a charged plane and, correspondingly, produce an approximately triangular well with an electric-field strength of

$$\epsilon_e = \frac{2\pi e n_{\mathrm{W}}}{\varepsilon_{\mathrm{InGaAs}}} \propto \sqrt{I} \tag{4.3}$$

where $\varepsilon_{\mathrm{InGaAs}}$ stands for dielectric constant of InGaAs layer. The ground electron state in such a well is given by

$$E_{\mathrm{e}} = b_{\mathrm{e}} I^{1/3} \tag{4.4}$$

with

$$b_{\mathrm{e}} = \left(\frac{9\pi}{8}\right)^{\frac{2}{3}} \left(\frac{h^2}{8\pi^2 m_{\mathrm{e}}}\right)^{\frac{1}{3}} \left(\frac{2\pi e^2}{\varepsilon_{\mathrm{InGaAs}}}\right)^{\frac{2}{3}} \left(\frac{\alpha (L + l)^2}{\gamma}\right)^{\frac{1}{3}} \tag{4.5}$$

where h and m_{e} stand for Planck coefficient and effective mass of electron, respectively. Similarly, the ground hole state can be expressed as;

$$E_{\mathrm{h}} = b_{\mathrm{h}} I^{1/3} \tag{4.6}$$

with

$$b_{\mathrm{h}} = \left(\frac{9\pi}{8}\right)^{\frac{2}{3}} \left(\frac{h^2}{8\pi^2 m_{\mathrm{h}}}\right)^{\frac{1}{3}} \left(\frac{2\pi e^2}{\varepsilon_{\mathrm{GaAsSb}}}\right)^{\frac{2}{3}} \left(\frac{\alpha (L + l)^2}{\gamma}\right)^{\frac{1}{3}} \tag{4.7}$$

where m_{h} and $\varepsilon_{\mathrm{GaAsSb}}$ stand for effective mass of hole and dielectric constant of GaAsSb layer, respectively. From these equations, the PL peak energy shift by photo-generated carriers should be proportional to the cubic root of excitation power density. As shown in Fig. 4.8, the PL peak energy shift is obviously proportional to the cubic root of excitation power density, which suggests formation of triangular wells at the interfaces between InGaAs and GaAsSb, peculiar to type-II

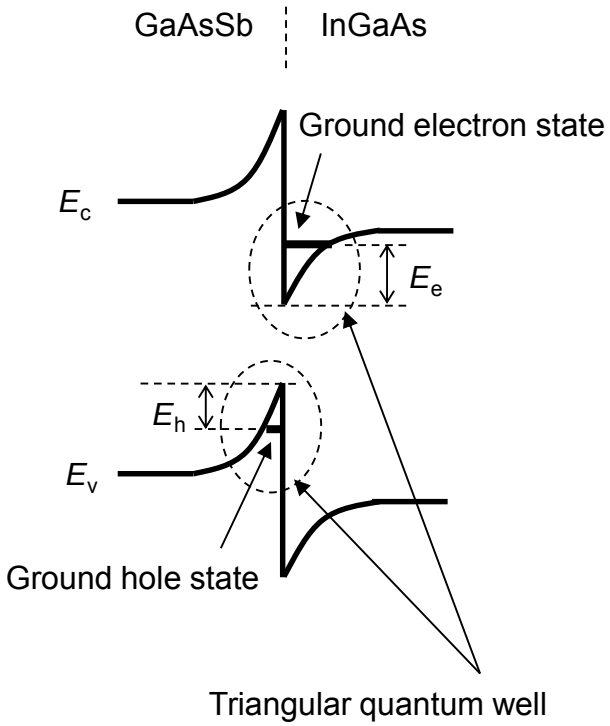

Fig. 4.7 Schematics of band structure of type-II SL with excited carriers

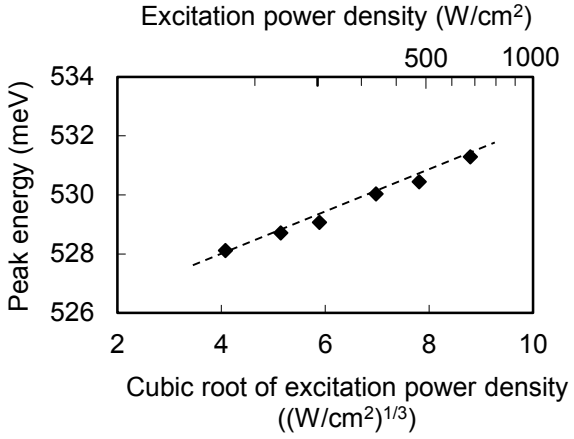

Fig. 4.8 Dependence of PL peak position on cubic root of excitation power density

material system.

The PL spectra of the SL measured in the temperature range from 4 to 300K are shown in Fig. 4.9. Even at 300K, the PL peak of the SL can be clearly seen at wavelength around 2.5μm. Dependence of PL peak energy on temperature is shown in Fig. 4.10. Generally, the band gap of semiconductor is expressed in Varshni's equation [11];

$$E_{\mathrm{g}}(T) = E_0 - \frac{\alpha T^2}{T + \beta} \tag{4.6}$$

where E_0 stands for band gap at 0K, and α and β are constants. The equation indicates that the band gap decreases monotonically as the temperature increases. However, the PL peak energy of the SL increased gradually as the temperature increased in the low temperature region, similar to the previous reports related to GaAs/GaSb, InAs/GaSb and InGaAs [9, 12, 4]. This phenomenon is derived from the particular joint density of states of type II SLs with the band-to-band absorption coefficient proportional to $(h\nu - E_{\mathrm{g}}^*(T))^{3/2}$ near the effective band gap $E_{\mathrm{g}}^*(T)$ [9, 12]. In that case, radiative recombination of electrons and holes of high-k values increase as the temperature increases. Assuming the Boltzmann distribution of non-equilibrium carriers and the band-to-band origin of radiative recombination, the PL peak energy should follow the $E_{\mathrm{g}}^*(T)+3/2kT$ dependence. $E_{\mathrm{g}}^*(T)$ of type-II InGaAs/GaAsSb SL is not clear. However, in the previous report, the dependence of PL peak energy of InAs/GaSb QWs on temperature was compared with InAs band gap [12]. We compared the PL peak energy of the InGaAs/GaAsSb SL with the band gap of $In_{0.53}Ga_{0.47}As$ and $GaAs_{0.51}Sb_{0.49}$, which are illustrated in Fig. 4.10. The band gaps were calculated using constants (E_0, α and β) of GaAs, InAs and GaSb, and the bowing parameter of $In_xGa_{1-x}As$ and $GaAs_xSb_{1-x}$ [13]. The temperature dependence of the difference between the PL peak position of the SL and the band gap of $In_{0.53}Ga_{0.47}As$ and $GaAs_{0.51}Sb_{0.49}$ is shown in Fig. 4.11. A dashed line with a slope of $3/2k$ is also illustrated. The temperature dependence of energy difference exhibited a slope of near $3/2k$. This suggests that the optical transition takes place between the conduction band of InGaAs and the valence band of GaAsSb. It was deduced that the type-II InGaAs/GaAsSb SL with GaAsSb grown at the optimized growth condition seems to have an excellent optical property.

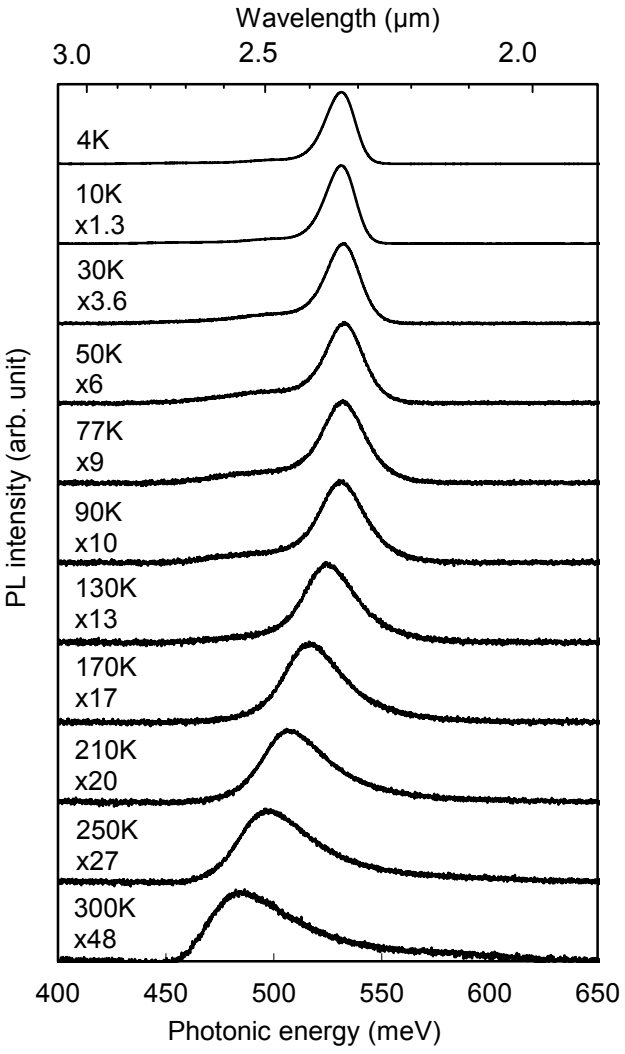

Fig. 4.9 PL spectra at different temperatures

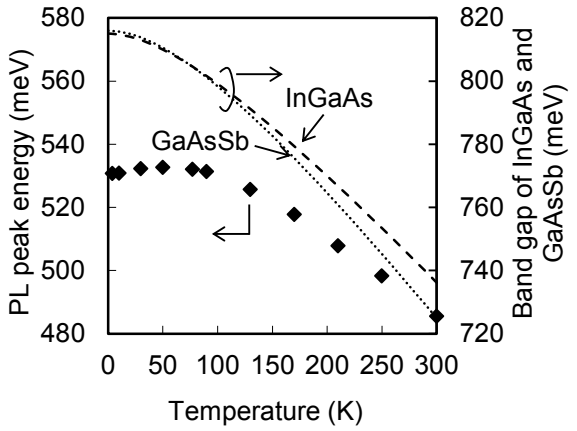

Fig. 4.10 Temperature dependence of the PL peak position and band gaps of $In_{0.53}Ga_{0.47}As$ $GaAs_{0.51}Sb_{0.49}$

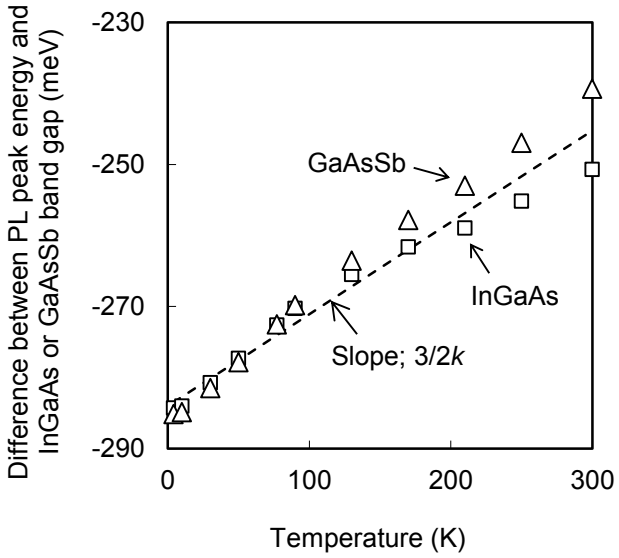

Fig. 4.11 Temperature dependence of the difference between the PL peak position and band gaps of $In_{0.53}Ga_{0.47}As$ $GaAs_{0.51}Sb_{0.49}$

4.5 Discrete NIR sensors with type-II InGaAs/GaAsSb SL absorption layers

4.5.1 Fabrication of sensors

Discrete NIR sensors were fabricated using 250 pairs of InGaAs (5nm)/ GaAsSb (5nm) SL absorption layers grown on S-doped InP (100) substrates at the optimized condition. The structure is the same as the sensors with GaAsSb absorption layers described in 4.3.1.

4.5.2 Electrical property

Current-voltage characteristics of the sensor at room temperature are shown in Fig. 4.12. The dark current density was 0.92mA/cm^2 at 1 V reverse bias, which is lower than those of conventional HgCdTe sensors by more than one order of magnitude [2].

4.5.3 Optical property

The responsivity spectrum of the sensor is shown in Fig. 4.13. The measurement was carried out at room temperature without a reverse bias voltage. Responsibility was recognized up to 2.5μm at room temperature. The maximum response was approximately 0.6A/W.

It was found that type-II InGaAs/GaAsSb SL is promising for absorption layer of NIR sensors with cutoff wavelength longer than 2μm for uncooled operation.

4.6 FPA with type-II InGaAs/GaAsSb SL absorption layer

A FPA with 320×256 pixels was fabricated by the process described in Chapter 2. The epi-wafer used for fabrication of PD array was equipped with the 250-pairs of InGaAs (5nm)/GaAsSb (5nm) SL absorption layer mentioned in 4.5.1 and InP window layer (0.8μm) re-grown by MOVPE method. Each pixel of PD array was 15μm diameter and 30μm pitch. Assembled FPA in ceramic package is shown in Fig. 4.14. The FPA was sealed with a silicon lid when the image was taken. Only infrared

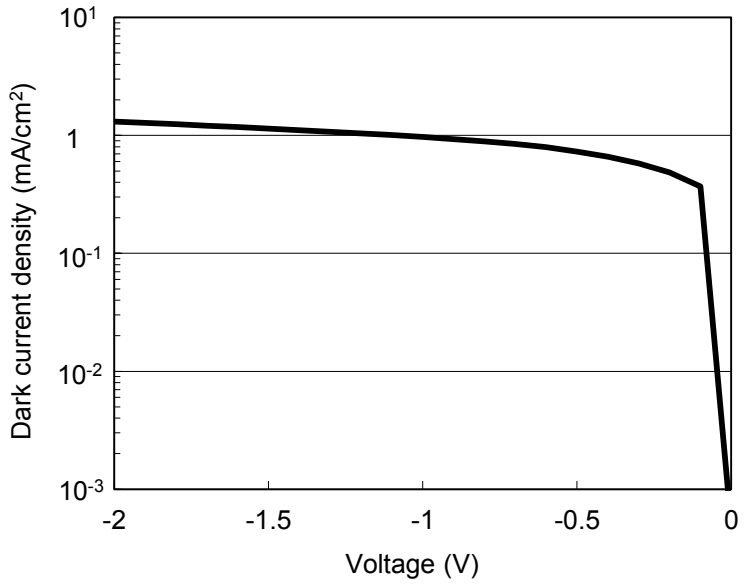

Fig. 4.12 Current-voltage characteristics of the NIR discrete sensor with type-II InGaAs/GaAsSb SL absorption layers measured at room temperature

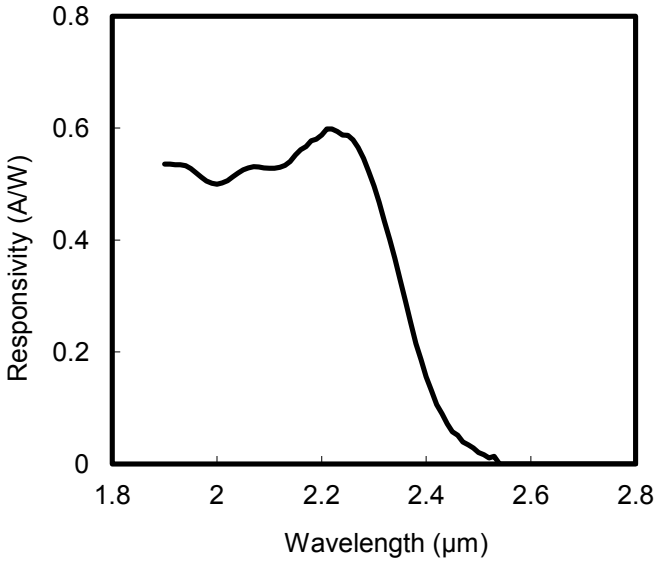

Fig. 4.13 Responsivity spectrum of the NIR discrete sensor with type-II InGaAs/GaAsSb SL absorption layer

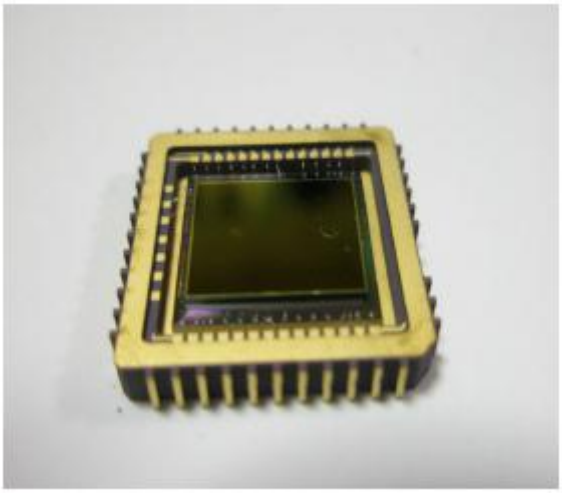

Fig. 4.14 FPA assembled in a ceramic package (without Si lid)

light reach the PD array because the silicon lid absorbs visible light. No cooler such as peltier cooler was included in the package. The output signal of ROIC was transferred to the NTSC signal by the electronics with FPGA.

320×256 SWIR imaging based on type-II InGaAs/GaAsSb SL PD was demonstrated. Figure 4.15 is an example of image taken at room temperature under illumination with the halogen lamp. A man's face can be recognized. More than 90% of the pixels were operated.

4.7 Strain-compensated type-II InGaAs/GaAsSb SL

In this section, result of growth and characterization of strain-compensated type-II InGaAs/GaAsSb SL is described.

4.7.1 Growth condition

Two kinds of type-II InGaAs(5nm)/GaAsSb(5nm) type-II SL were grown on Fe-doped(100) InP substrates. The one is strain-compensated, where InGaAs layers with -0.6% lattice-mismatch and GaAsSb layers with +0.6% lattice-mismatch were used. The other is lattice-matched where lattice-matched InGaAs and GaAsSb layers were used. The growth temperature was 480˚C. The growth rates of InGaAs and GaAsSb layers were 1.5 and 0.7 μm/h, respectively. 0.15μm-thick InAlAs buffer layers were grown for all the samples. All the epitaxial layers were intentionally un-doped. The As was supplied by a needle-valve cracking cell, where the cracking zone temperature is set at 600˚C, so that tetramer As_4 was supplied in this study. The tetramer Sb_4 was supplied by a conventional effusion cell.

4.7.2 Optical property

Fig. 4.16 shows the PL spectra at 300K of the lattice-matched SL and the strain-compensated SL. It is clearly seen that the peak wavelength of the strain-compensated SL is longer than that of the lattice-matched SL. The observed peak energy shift is 43meV at 300K. On the other hand, the calculated energy shift of 31meV using the model solid theory [14]. The energy difference between the experimental value and the calculated value is 12meV. The Ga composition of the InGaAs is 0.47 and the Sb composition of the GaAsSb is 0.49 for the lattice-matched SL, while the Ga composition of the

Fig. 4.15 Infrared image captured by the FPA with type-II InGaAs/GaAsSb SL absorption layer

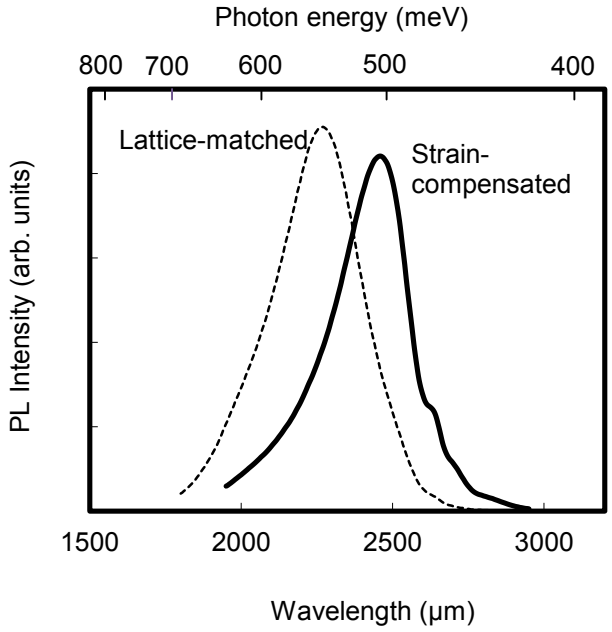

Fig. 4.16 PL spectra of the strain-compensated and lattice-matched InGaAs/GaAsSb SLs

InGaAs is 0.54 and the Sb composition of the GaAsSb is 0.56 for the strain-compensated SL. In the calculation, the change of the effective band gap at the InGaAs/GaAsSb hetero-interface was neglected because the composition changes of Ga and Sb are the same (0.07). Probably, this assumption caused the difference between the experimental energy shift and the calculated energy shift. The PL peak intensity of the strain-compensated SL is almost the same as that of the lattice-matched SL, suggesting that the crystalline quality of the strain-compensated SL is comparable to that of the lattice-matched SL.

4.7.3 Electrical property

Electrical properties were studied using Hall measurements. Table 4.1 summarizes the carrier concentration and the mobility for both samples at 77K. It is clearly seen that the electron concentration and the electron mobility are comparable for both samples. These results suggest that impurity and/or defect densities of the strain-compensated SL is the same level as that of the lattice-matched SL, indicating that the strain-compensated structure is very effective to realize longer wavelength operation of the NIR sensors with type-II InGaAs/GaAsSb SL absorption layers.

Table. 4.1 Electrical properties of the strain-compensated and lattice-matched InGaAs/GaAsSb SLs

	Electron concentration (cm^{-3})	Mobility (cm^2/Vs)
Lattice-matched	2.60×10^{15}	3720
Strain-compensated	1.78×10^{15}	4900

4.8 Summary

The author summarizes this chapter below;

• Growth condition of GaAsSb was optimized. It was found that growth temperature affects uniformity of As and Sb distribution. 1μm-thick GaAsSb layers with single X-ray diffraction peak were obtained within narrow growth temperature window. V/III flux ratio has optimum value in the sense of crystalline quality as well.

• Measurement of electrical characteristics of sensors with GaAsSb absorption layers evidenced that growth condition of GaAsSb influences dark current of sensors. The sensor with GaAsSb absorption layer grown at the optimum condition showed lower dark current than the sensor with GaAsSb absorption layer grown at lower V/III flux ratio. Temperature dependence of the dark current suggested that generation-recombination process was suppressed in the GaAsSb absorption layer grown at the optimum condition.

• By using optimized GaAsSb, type-II InGaAs/GaAsSb SL with excellent optical quality was obtained. PL peak with wavelength around 2.5μm was clearly observed at room temperature. From the dependence of PL peak energy on excitation power density, triangular quantum well at the InGaAs/GaAsSb interface peculiar to type-II material systems. Temperature dependence of PL peak energy indicated that the PL peak was derived from optical transition between the conduction band of InGaAs and the valance band of GaAsSb.

• NIR sensor with cutoff wavelength of 2.5μm was obtained by utilizing type-II InGaAs/GaAsSb SL absorption layer with optimized GaAsSb. It exhibited maximum response of 0.6A/W and dark current lower than those of conventional HgCdTe sensors by more than one order of magnitude.

• An FPA with type-II InGaAs/GaAsSb SL absorption layer was demonstrated. An infrared image was successfully captured without cooling.

• A strain-compensated type-II InGaAs/GaAsSb SL was experimentally proved to realize longer PL wavelength compared to lattice-matched SL without deterioration of crystalline quality. It is expected that the strain-compensated type-II SL can be applied to NIR sensors with longer cuttoff wavelength.

The author concludes that type-II InGaAs/GaAsSb SL is a predominant candidate for absorption layer material of NIR sensor, provided the growth condition of GaAsSb is carefully optimized.

Reference

[1] K. Miura, Y. Iguchi, M. Tsubokura, Y. Kawamura, J. of Appl. Phys. (submitted)

[2] H. Inada, K. Miura, Y. Nagai, M. Tsubokura, A. Moto, Y. Iguchi, Y. Kawamura, Proc. IPRM, Vol. 21, 149 (2009)

[3] H. Inada, K. Miura, H. Mori, Y. Nagai, Y. Iguchi, Y. Kawamura, Proc. of SPIE, Vol. 7660, 76603N

(2010)

[4] Y. Yonezawa, R. Hiraike, K. Miura, Y. Iguchi, Y. Kawamura, Physica E, Vol.42 2781 (2010)

[5] C. –A. Chang, R. Ludeke, L. L. Chang, L. Esaki, Appl. Phys. Lett., Vol. 31, 759 (1977)

[6] B.-R. Wu, C. Xu, K.-L. Chang, K.-C. Hsieh, K. Y. Cheng, J. Vac. Sci. Technol. B, Vol. 23, 1641 (2005)

[7] H. Miyoshi, R. Suzuki, H. Amano, Y. Horikoshi, J. of Cryst. Growth, Vol. 237-239, 1519 (2002)

[8] Y. Nakata, T. Fujii, A. Sandhu, Y. Sugiyama, E. Miyauchi, J. of Cryst. Growth, Vol. 91, 655 (1988)

[9] N. N. Ledentsov, J. Böhrer, M. Beer, F. Heinrichsdorff, M. Grundmann, D. Bimberg, Phys. Rev. B, Vol. 52, No. 19, 14058 (1995)

[10] Y. S. Chiu, M. H. Ya, W. S. Su, Y. F. Chen, J. of Appl. Phys., Vol. 92, 5810 (2002)

[11] Y. P. Varshni, Physica, Vol. 34, 149 (1967)

[12] N. Bertru, A. N. Baranov, Y. Cuminal, G. Boissier, C.Alibert, A. Joullie, B. Lambert, J. of Appl. Phys., Vol. 85, 1989 (1999)

[13] I. Vurgaftman, J. R. Meyer, L. R. Ram-Mohan, J. of Appl. Phys., Vol. 89, 5815 (2001)

[14] C. G. Van de Walle, Phys. Rev. B, Vol. 39, 1871 (1989)

Chapter 5 Growth and characterization of type-II InAs/GaSb superlattices on InP substrates for mid-infrared sensors

In this chapter, growth technology of type-II InAs/GaSb SLs on InP substrates for MIR sensors is described. This study was advanced in the following procedure;

• Transparency spectra of InP substrates were measured in order to test the feasibility.

• Growth of GaSb layers on InP substrates was discussed.

• InAs/GaSb SLs were grown on InP substrates to compare the crystalline quality to that of SLs on GaSb.

• Sensors with InAs/GaSb SLs absorption layers on InP substrates were fabricated. Characteristics of sensors on InP substrates and GaSb substrates were compared.

5.1 Feasibility of InP substrates

Transmission spectra of InP substrates were measured in order to choose substrates with high transparency in MIR region. Two kinds of InP substrates widely available, semi-insulating InP:Fe and n-type InP:S, were tested by FT-IR. The thicknesses are 320~350μm. As a reference, a transparency spectrum of an undoped GaSb substrate was also measured. The thickness is 500μm. The spectra are shown in Fig. 5.1. The InP:Fe substrate showed high transparency at wavelength longer than 3μm, where the InP:S and undoped GaSb substrates have low transparency. It is reported that calculated transparency of GaAs substrate is higher with lower carrier concentration [1]. Therefore,

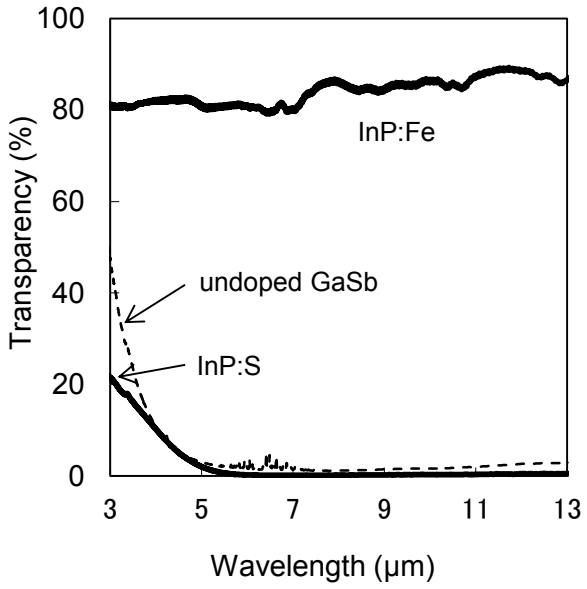

Fig. 5.1 Transparency spectra of InP and GaSb sublstrates

semi-insulating substrates might be preferable. In this study, InP:Fe substrates were used.

5.2 Growth of GaSb layers on InP substrates

5.2.1 Growth condition

The growth condition of GaSb layers on InP substrates is described below; As and Sb fluxes were controlled by needle-valve cracking cells. The cracking temperatures were kept at 600ºC and 800ºC for As and Sb, respectively. Prior to growth, the InP:Fe(100) substrates were thermally cleaned in the growth chamber under As flux. 0.15μm-thick $In_{0.53}Ga_{0.47}As$ layers were grown in order to smoothen the surfaces of the substrates. The growth rate was 1.17μm/h. Finally, GaSb layers were grown. The growth temperature was 480ºC. The growth rate of GaSb was 0.55μm/h.

5.2.2 Characterization of crystalline quality

Two GaSb layers with different thickness were grown; 0.5μm and 2μm. In the XRC of the GaSb layers, the diffraction peaks of GaSb (400) were broad but single as shown in Fig. 5.2. Calculated diffraction peak positions of bulk GaSb are also shown as the dotted lines. The GaSb layers are inferred to be almost fully relaxed from the peak positions. However, no crosshatch was observed on the surfaces (Fig. 5.3). The thicker GaSb showed a diffraction peak with narrower FWHM, indicating crystalline quality is improved by growing thicker layer.

5.3 Growth and characterization of type-II SLs on InP substrates

5.3.1 Growth condition

Type-II InAs/GaSb SLs were grown following GaSb buffer layers described in 5.2.1. The SLs consisted of 50 pairs of 3.5nm-thick InAs and 2.1nm-thick GaSb. The growth temperature of the SL was 450ºC. As a reference, a SL on a GaSb substrate was also grown using a 0.5μm-thick GaSb buffer layer. The SL has the same periodic structure with the SLs on InP substrates mentioned above. First,

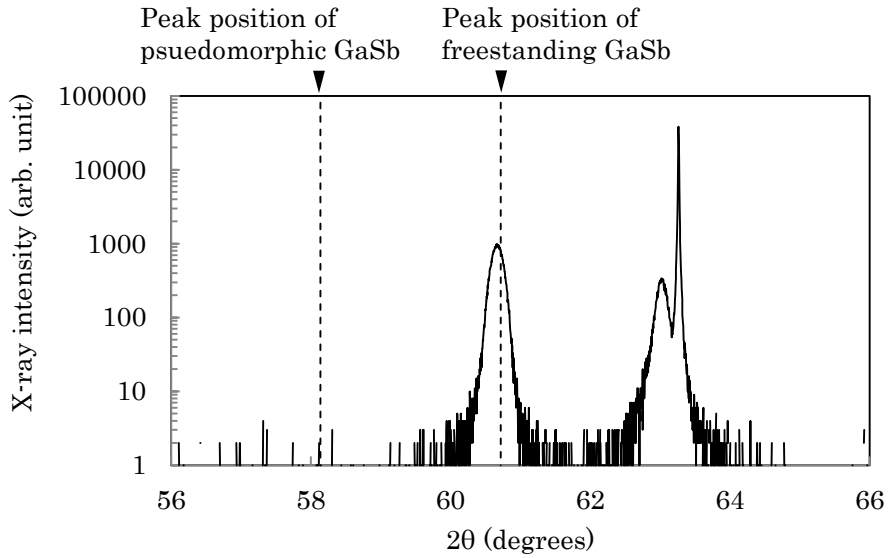

(a) 0.5μm-thick

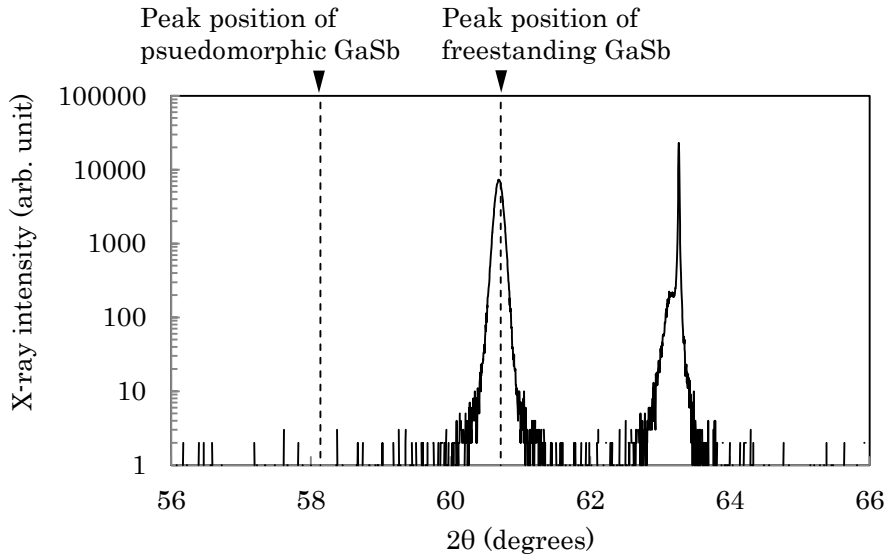

(b) 2μm-thick

Fig. 5.2 XRCs of the GaSb layers grown on InP substrates using InGaAs buffer layers

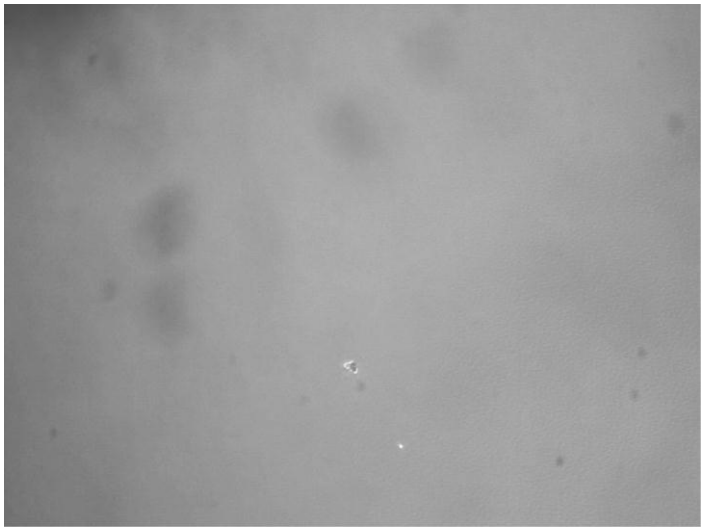

(b) 0.5μm-thick

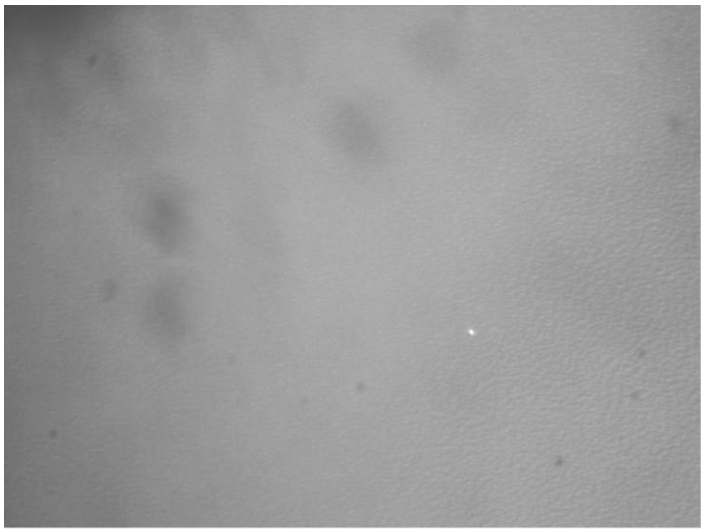

(b) 2μm-thick

Fig. 5.3 Images of the surfaces of the GaSb layer layers grown on InP substrates

undoped GaSb (100) substrates were cleaned thermally in the growth chamber as described in Chapter 2. Then a 0.15μm-thick undoped GaSb buffer layer and SL were grown. The SLs on the InP substrate and the GaSb substrate were not grown simultaneously.

5.3.2 Characterization of crystalline quality

Several SLs were grown on InP substrates using GaSb buffer layers with different thickness. On the surfaces of the SLs, no crosshatch was observed (Fig. 5.4).

XRCs of the SLs are shown in Fig. 5.5. Satellite peaks are clearly seen in the 2θ/ω XRCs of the SLs, indicating periodic structures. From the results of fitting, the periods of the SLs on 0.5μm-thick buffer layer and 2.5μm-thick buffer layer were proved to be 5.6nm and 5.72nm, respectively. In both XRCs, the peak positions of the SLs seem to coincide with those of GaSb buffer layers, probably due to the incorporation of Sb in the InAs layers. The SL on 2.5μm-thick buffer layer exhibited narrower satellite peaks than the SL on 0.5μm-thick buffer layer. The crystalline quality of the SL seems to be improved by increasing GaSb buffer layer thickness.

In a cross sectional TEM bright-field image of the SL on 0.5μm-thick buffer layer, five threading dislocations can be clearly seen in the region of 0.8μm wide in the SL as shown in Fig. 5.6(a). The linear density of the threading dislocations is approximately $6.3\times10^{4}cm^{-1}$. The dislocations were generated at the initial stage of GaSb growth to propagate to the SL. Merckling et al have reported a TEM image of GaSb grown on InP substrate without obvious threading dislocations [2]. Further optimization of GaSb growth condition is needed in order to reduce threading dislocations. The dislocations in upper region of the GaSb buffer layer are reduced, suggesting that the threading dislocations annihilated one another as the growth proceeded, similar to GaSb grown on GaAs [3]. It is expected that using thicker GaSb buffer layer reduces threading dislocation in the SL. TEM observation of a SL on 4.5μm-thick GaSb buffer layer was performed on several positions. One of the TEM images is shown in Fig. 5.6 (b). Two threading dislocations were seen in the region of 40μm wide in total. The linear density of the threading dislocations is $5.0\times10^{2}cm^{-1}$, which is lower by two orders of magnitude than that in the SL on 0.5μm-thick buffer layer. Thick GaSb buffer layers are preferable for growth of SLs because threading dislocations decrease during buffer layer growth, resulting in fewer dislocations propagating to SL. This result agrees with the FWHMs of X-ray diffraction peaks of GaSb layers.

PL measurements were performed on the SLs on the InP substrates with 0.5μm-thick and 2.5μm-thick GaSb buffer layers. The SL grown on a GaSb substrate was also characterized. PL spectra of the SLs measured at 4K are illustrated in Fig. 5.7. PL peaks were distributed in the range of

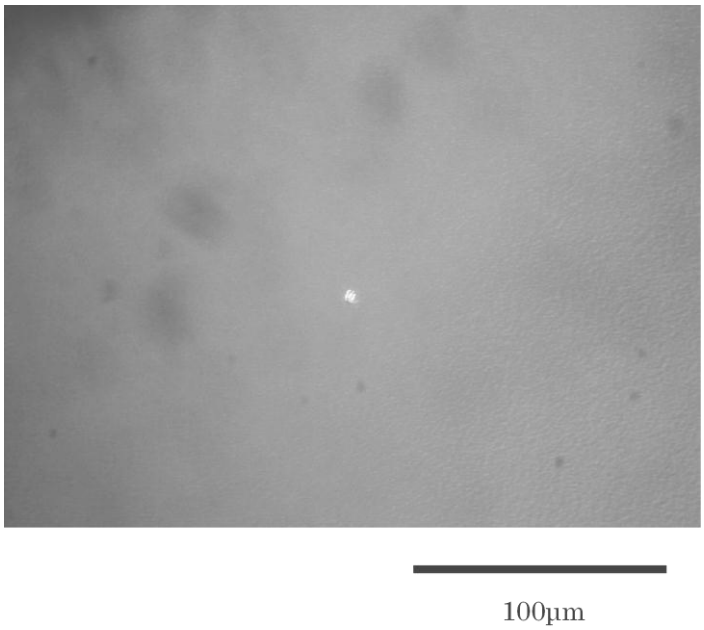

(a) SL with 0.5μm-thick GaSb buffer layer

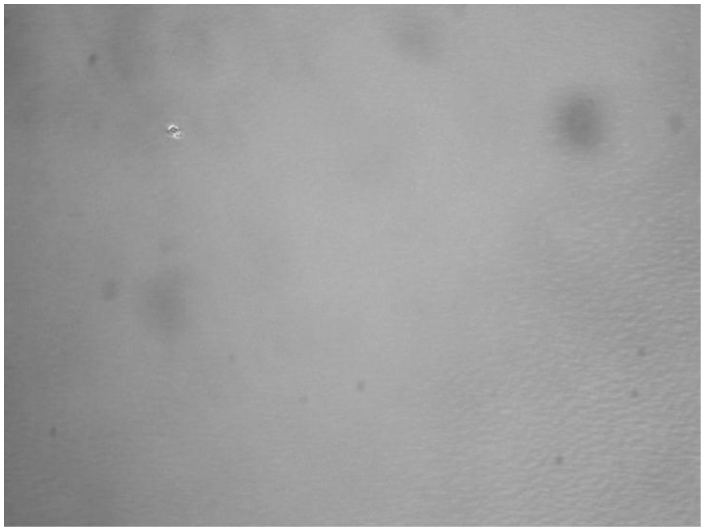

(b) SL with 2.5μm-thick GaSb buffer layer

Fig. 5.4 Images of the surface of the type-II InAs/GaSb SLs grown on InP by optical microscopy

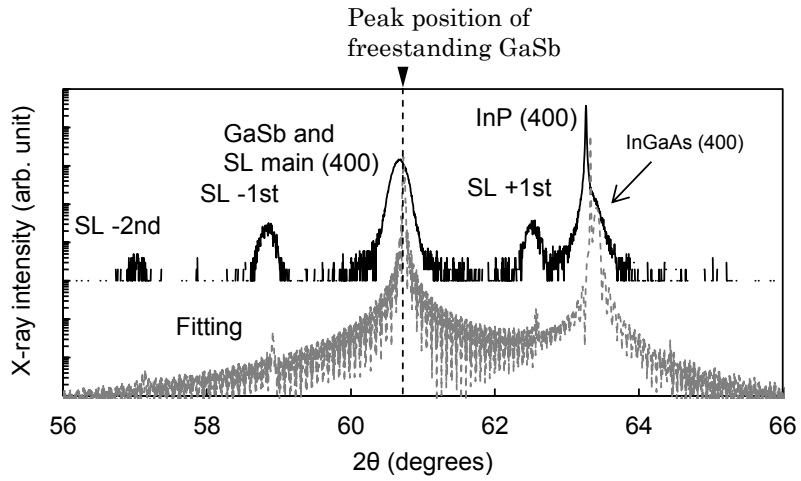

(a) SL on InP substrate with 0.5μm-thick GaSb buffer layer

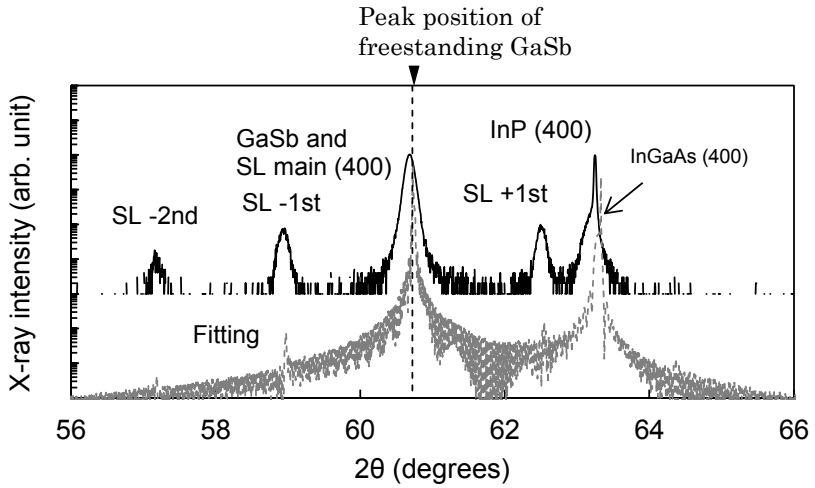

(b) SL on InP substrate with 2.5μm-thick GaSb buffer layer

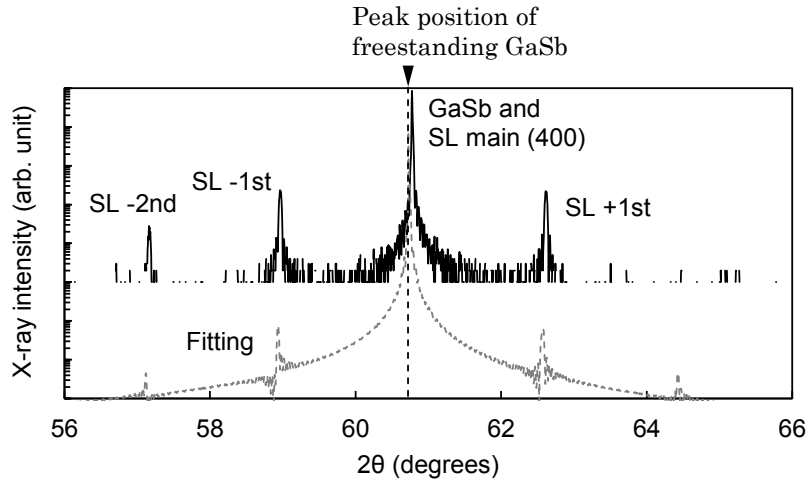

(c) SL on GaSb substrate

Fig. 5.5 XRCs of the type-II InAs/GaSb SLs grown on InP substrates

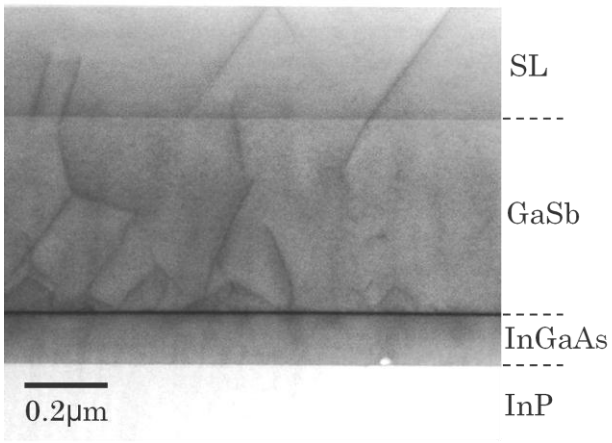

(a) 0.5μm-thick GaSb buffer layer

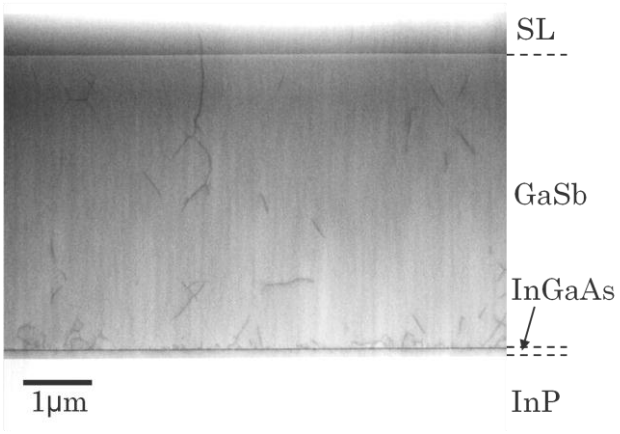

(b) 4.5μm-thick GaSb buffer layer

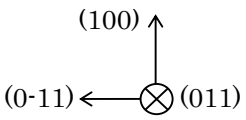

Fig.5.6 Cross sectional TEM image of SLs grown on an InP substrates

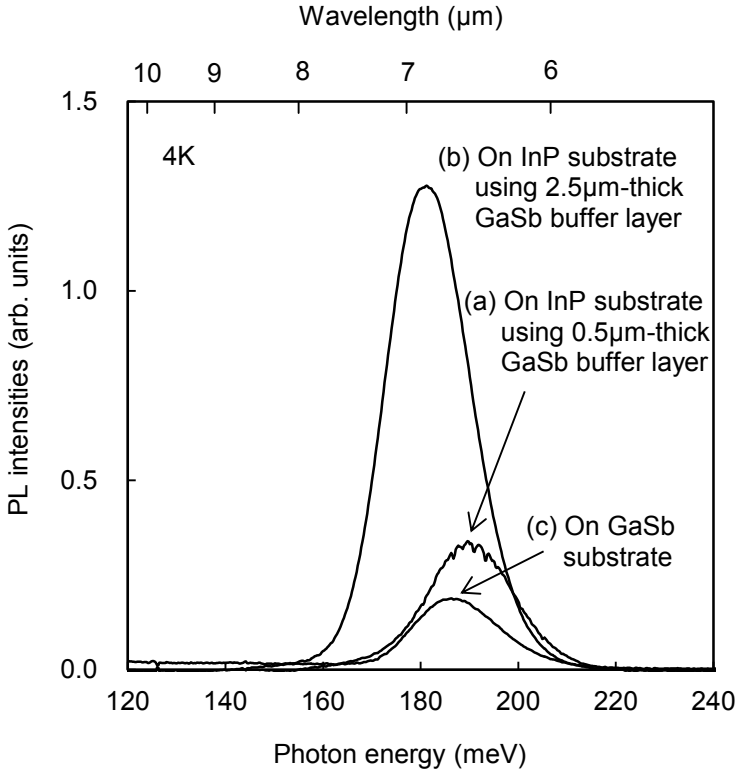

Fig. 5.7 PL spectra of SLs grown on an InP substrates

wavelength from 6.6μm to 6.9μm. The fluctuation of the PL wavelengths seems to be derived from fluctuation of the SL periods. Both SLs on the InP substrates showed stronger PL peak intensities than the SL on the GaSb substrate. Especially, the SL on 2.5μm-thick GaSb buffer layer showed PL peak intensity approximately three times stronger than the SL on 0.5μm-thick buffer layer. This might be because of reduced threading dislocation density in the SL. The reason why the PL intensities of SLs on InP substrates are stronger than that of the SL on GaSb substrate is unknown yet. However, it can be said that SLs with good optical quality were obtained on InP substrates.

5.4 Discrete MIR sensors with InAs/GaSb SL absorption layers on InP substrates

MIR sensors with type-II InAs/GaSb SL absorption layers were fabricated on InP substrates. The property of the sensors was compared to that of sensors on GaSb substrate.

5.4.1 Fabrication of sensors

The epitaxial wafer for MIR sensors with InAs/GaSb SL absorption layer was grown on InP substrate in the following procedure; After an InP:Fe(100) substrate was thermally cleaned in the growth chamber under As flux, a 0.15μm-thick $In_{0.53}Ga_{0.47}As$ layer was grown in order to smoothen the surface of the substrate. The growth rate was 1.17μm/h. Next, 4.5μm-thick GaSb:Be buffer layer was grown, since thick GaSb buffer layer is found to reduce threading dislocation propagating into the SL as mentioned in 5.3.2. The growth temperature was 480ºC. Type-II InAs/GaSb SLs, which consist of 100 pairs of 3.6nm-thick InAs and 2.1nm-thick GaSb, were grown. Be is doped in the GaSb layers in the bottom 30 pairs. Si is doped in the InAs layers in upper 30 pairs. The middle 40-pair region is non-intentionally doped. The growth temperature of the SL was 450ºC. Finally, 20nm-thick InAs:Si cap layer was grown. The growth rates of GaSb and InAs were both 0.55μm/h.

As a reference, an epitaxial wafer for MIR sensors on GaSb substrate was also grown. A 0.5μm-thick GaSb:Be buffer layer and a SL with the same structure with that on InP substrate were grown.

The MIR sensors were fabricated by the process mentioned in 2.3.1.

5.4.2 Electrical property

Current-voltage characteristics of the sensors on InP and GaSb substrates at several temperatures were compared (Fig.5.8). The dependences of dark current densities of the sensors on temperature are shown in Fig. 5.9. At higher temperature, the dark current of the sensor on InP substrate is comparable to that on GaSb substrate. However, the separation of the dark current densities becomes more noticeable at lower temperature. Similar to the sensors with GaAsSb absorption layers described in Chapter 4, the factors n of the sensors on InP and GaSb substrates were calculated following the equation [4];

$$J \propto \exp\left(-\frac{E_g}{nkT}\right) \tag{5.1}$$

where J, E_g, k and T stand for dark current density, band gap of the absorption layer, Boltzmann constant, temperature, respectively. The factors n were 1.78 and 1.34 for the sensors on InP and GaSb substrates, respectively. It is inferred that the dark current of the sensor on InP substrate is generated by the threading dislocations. Suppression of threading dislocation in the SL is necessary.

5.4.3 Optical property

The sensor on InP substrate showed external quantum efficiency of 10% around wavelength of 5μm (Fig. 5.10). As mentioned in 5.4.1, the SL absorption layer consists of 100 pairs of InAs/GaSb. It is reported that the quantum efficiency increases proportionally to the thickness of the SL absorption layer [5]. It is expected that thicker absorption layer would improve quantum efficiency.

5.5 Summary

The author summarizes this chapter below;

• InAs/GaSb SLs grown on InP substrates were characterized. High quality SLs were successfully obtained on InP substrates. The crystalline quality of SL can be improved by using thick GaSb buffer layer because threading dislocations propagating to SL are reduced. SLs on InP substrates showed stronger PL intensity than a SL on GaSb substrate.

• Mid-infrared sensor with InAs/GaSb SL absorption layer grown on InP substrate was

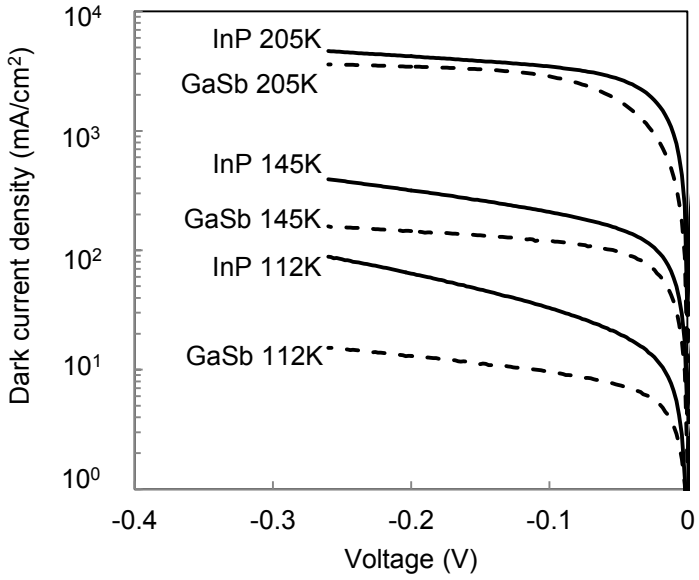

Fig. 5.8 Current-voltage characteristics of the MIR sensor with type-II InAs/GaSb absorption layers grown on the InP substrate and the GaSb substrate

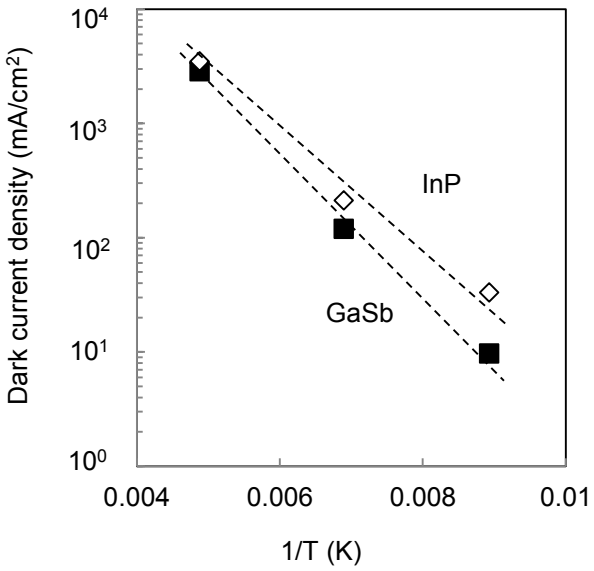

Fig. 5.9Dependence of the dark current densities on temperature

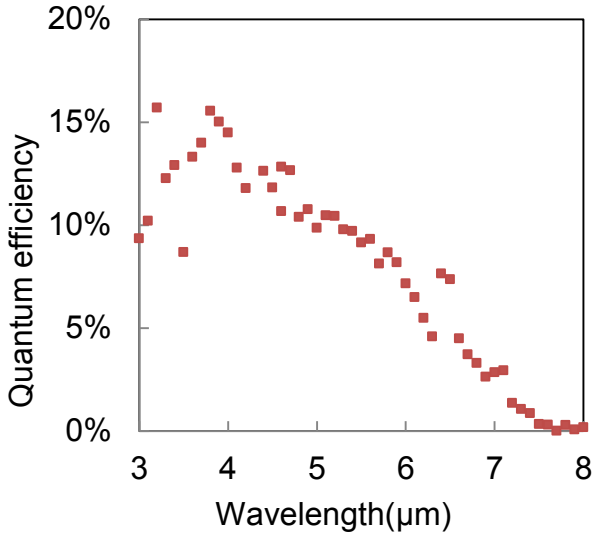

Fig. 5.10External quantum efficiency spectrum of the MIR sensor on InP substrate

demonstrated for the first time. Although the dark current is higher than the sensor on GaSb substrate, the sensor on InP substrate exhibited external quantum efficiency of 10%, which is expected to be improved by using a thicker absorption layer.

Although improvement of crystalline quality is needed, InAs/GaSb SL grown on InP substrate is promising for the absorption layer of mid-infrared FPAs.

References

[1] K. Miura, Y. Iguchi, Y. Kawamura, J. of Cryst. Growth (revised)

[2] A. Khoshakhlagh, E. Plis, S. Myers, Y. D. Sharma, L. R. Dawson, S. Krishna, J. of Cryst. Growth, Vol. 311 1901 (2009)

[3] C. Merckling, X. Sun, A Alian, G. Brammertz, V. V. Afanas ’ev, T. Y. Hoffman, M. Heyns, M. Caymax, J. Dekoster, J. of Appl. Phys. Vol. 109, 073719 (2011)

[4] P. M. Thibado, B. R. Bennett, M. E. Twigg, B.V. Shanabrook, L. J. Whitman, J. of Vac. Sci. Technol. A Vol. 14 885 (1996)

[5] H. Inada, K. Miura, H. Mori, Y. Nagai, Y. Iguchi, Y. Kawamura, Proc. of SPIE, Vol. 7660, 76603N (2010)

[6] A. Hood, D. Hoffman, B.-M. Nguyen, P.-Y. Delaunay, E. Michel, and M. Razeghi, Appl. Phys. Lett., Vol. 89, 093506 (2006)

Chapter 6 Conclusion

6.1 Conclusion

In this thesis, three kinds of novel materials for infrared sensor absorption layers grown on InP substrates were studied; InGaAsN (for NIR sensor), InGaAs/GaAsSb SL (for NIR sensor) and InAs/GaSb SL (for MIR sensor). MBE growth method was utilized for growth techniques since MBE is advantageous to growth of InGaAsN with high In composition lattice-matched to InP substrate and growth of abrupt hetero-interfaces.

In Chapter 3, growth and characterization of thick InGaAsN layers lattice-matched to InP substrates were described. First, InGaAsN layers grown using ECR plasma cell were characterized. It was comfirmed that the band gap of InGaAsN became narrower with increase in N composition by PL and PR measurement. Depth profile of N composition in a 1μm-thick InGaAsN layer revealed the uniform distribution of N in the direction of growth. The crystalline quality of thick InGaAsN layer grown using As_4 can be improved by post-growth annealing in a proper temperature. Using As_2 instead of As_4 during growth also improves the crystalline quality of InGaAsN layer. Adding Sb flux improved the crystallographic quality and surface morphology of InGaAsN layers. PL wavelength became longer by adding Sb flux.

Next, InGaAsN with RF plasma cell was studied. By optimizing growth temperature and As/III flux ratio, the author obtained the thick InGaAsN layer which show PL peak with wavelength as long as 2.03μm at room temperature. However, sensors with InGaAsN absorption layers with PL wavelength of ~1.9μm exhibited much higher dark current compared with that with an InGaAs absorption layers. Moreover, the dark current tended to increase with increasing PL wavelength of the absorption layer. The author concluded that utilizing InGaAsN for NIR sensors is difficult, although several academic discoveries have been achieved.

In Chapter 4, growth and characterization of InGaAs/GaAsSb SLs were described. The author focused on growth condition of GaAsSb. It was found that growth temperature affects uniformity of As and Sb distribution considerably. 1μm-thick GaAsSb layers with single X-ray diffraction peak were obtained within narrow growth temperature window. V/III flux ratio has optimum value in the sense of crystalline quality as well.

The influence of GaAsSb growth condition on electrical characteristic of sensors was studied by fabricating sensors with GaAsSb absorption layers. It was revealed that V/III flux ratio of GaAsSb affects dark current of sensors significantly. Dependence of dark current on temperature suggested that generation-recombination process was suppressed in the optimized GaAsSb layer.

A type-II InGaAs/GaAsSb SL with the optimized GaAsSb was grown and characterized. PL peak with wavelength around 2.5μm was clearly observed at room temperature. From the dependence of PL peak energy on excitation power density and temperature, the PL peak was found to be derived from optical transition between the conduction band of InGaAs and the valance band of GaAsSb.

NIR sensor with 2.5μm cutoff wavelength was obtained by utilizing type-II InGaAs/GaAsSb SL absorption layer. The sensor exhibited lower dark current than those of conventional HgCdTe sensors by more than one order of magnitude. The maximum of response was approximately 0.6A/W. An FPA with type-II InGaAs/GaAsSb SL absorption layer successfully captured an infrared image without cooling. It was shown that type-II InGaAs/GaAsSb SL PDs have a potential of uncooled operation for imaging applications.

Strain-compensated type-II InGaAs/GaAsSb SL was grown and characterized. It was experimentally confirmed that the longer PL wavelength was obtained than lattice-matched SL without deterioration of crystalline quality.

These results evidence that type-II InGaAs/GaAsSb SL is a predominant candidate for absorption layer material of NIR sensor, provided the growth condition of GaAsSb is carefully optimized.

In Chapter 5, growth of type-II InAs/GaSb SLs on InP substrates for MIR sensor absorption layers were studied. Type-II InAs/GaSb SLs were grown on InP substrates using GaSb buffer layers. 2μm-thick GaSb buffer layer was grown on InP substrate without crosshatch. Many threading dislocations were generated at the initial stage of GaSb buffer layer growth and propagate in the InAs/GaSb SL grown on the buffer layer. However, the threading dislocations were reduced drastically by using thick GaSb buffer layer. The SLs on InP substrates exhibited stronger PL peaks compared to the SL on GaSb substrate.

An MIR sensor with type-II InAs/GaSb SL absorption layer on InP substrate was fabricated. The MIR sensor with on InP substrate showed higher dark current than sensor on GaSb substrate, probably due to threading dislocations in the SL absorption layer. However, the sensor on InP substrate exhibited 10% of external quantum efficiency at wavelength around 5μm. Although improvement of crystalline quality is needed, InAs/GaSb SL grown on InP substrate is promising for the absorption layer of mid-infrared FPAs.

6.2 For future work

Through this study, several technological discoveries about the materials were achieved. However, many problems are still left. The author summaries the problems for each material below;

6.2.1 InGaAsN

• N incorporation into InGaAsN

As described in Chapter 3, the N incorporation decreased at lower As/III ratio as well as high As/III ratio. It might due to N incorporation mechanism which is still unknown. The author expects elucidation of the mechanism would lead us to growth of InGaAsN layers with even larger N compositions and longer PL wavelengths.

6.2.2 InGaAs/GaAsSb SL

• Optimization of growth sequence of InGaAs/GaAsSb hetero-interface

As demonstrated in Chapter 4, the image captured by the FPA with the InGaAs/GaAsSb SL absorption layer is blurred yet. Further improvement of sensitivity is needed. It is inferred that quality of InGaAs/GaAsSb hetero-interfaces influences characterisitics of sensors as well as crystalline quality of GaAsSb, because a InGaAs/GaAsSb SL absorption layer contains hundreds of hetero-interface. Actually, many researchers have paid much attention to InAs/GaSb hetero-interface [1-4]. Although crystalline quality of GaAsSb was discussed in this study, quality of InGaAs/GaAsSb hetero-interface was not studied. However, quality of hetero-interface might deteriorate during the intervals between InGaAs and GaAsSb growth in this study. Discussion of growth sequence (duration of the intervals) might realize higher sensitivity of NIR sensors and clearer images of FPAs.

• Application of strain-compensated InGaAs/GaAsSb SL to FPA

To obtain FPA with longer cutoff wavelength, strain-compensated InGaAs/GaAsSb should be applied to absorption layers.

6.2.3 InAs/GaSb SL

• Reduction of threading dislocations in InAs/GaSb SL on InP substrate

It was inferred that threading dislocations in InAs/GaSb SL absorption layers deteriorate the characteristics of the sensors. The threading dislocations in the SLs have propagated from the GaSb buffer layers. Merckling et al have reported a TEM image of GaSb grown on InP substrate without obvious threading dislocations [5]. Further optimization of GaSb growth condition is needed in order to reduce threading dislocations.

• Further investigation of growth condition of InAs/GaSb SL

In this study, the growth condition of InAs/GaSb SL is not discussed. To improve the characteristics of sensors (such as dark current and external quantum efficiency), investigation of growth condition of InAs/GaSb SL is necessary. Similar to InGaAs/GaAsSb SL, optimization of growth sequence of InAs/GaSb hetero-interface is also required.

• Application of InAs/GaSb SL on InP substrate to FPA

Advantages of the InP substrates for MIR sensors, high transparency in infrared region and smaller difference of thermal expansion coefficient with that of Si, are expected to be the most effective in the case of being applied to FPAs. Demonstration of FPAs with InAs/GaSb SL absorption layers on InP substrates is necessary in order to prove the usefulness.

References

[1] M. E. Twigg, B. R. Bennett, B. V. Shanabrook, J. R. Waterman, J. L. Davis, and R. J. Wagner, Appl. Phys. Lett., Vol. 64, 3476 (1994)

[2] R. Kaspi, J. of Cryst. Growth, Vol. 201/202, 864 (1999)

[3] E. Luna, B. Satpati, J. B. Rodriguez, A. N. Baranov, E. Tournié, and A. Trampert, Appl. Phys. Lett, Vol. 96, 021904 (2010)

[4] Y. Ashuach, Y. Kauffmann, D. Isheim, Y. Amouyal, D. N. Seidman, and E. Zolotoyabko, Appl. Phys. Lett, Vol. 100, 241604 (2012)

[5] C. Merckling, X. Sun, A Alian, G. Brammertz, V. V. Afanas'ev, T. Y. Hoffman, M. Heyns, M. Caymax, J. Dekoster, J. of Appl. Phys. Vol. 109, 073719 (2011)

Acknowledgements

The author is truly in debt to Professor Yuichi Kawamura for his continuous guidance, supervision and encouragement throughout this work.

The author also wishes to express his sincere gratitude to Professor Hajime Ishihara and Professor Hiromichi Horinaka for providing the opportunity to accomplish this work and their critical reading of the manuscript and valuable suggestions. The author acknowledges Professor Norifumi Fujimura, Professor Seiji Akita, Professor Takekazu Isida, Professor Hiroyoshi Naito and Professor Yoshihiko Hirai for their fruitful advices and stimulating comments on this dissertation.

The author would like to express his deep appreciation to Dr. Yasuhiro Iguchi at Transmission Devices R&D Laboratories in Sumitomo Electric Industries for his understanding, helpful support and continuous encouragement. The author is very much indebted to Dr. Tsukuru Katsuyama at Transmission Devices R&D Laboratories in Sumitomo Electric Industries for his helpful advice on experiments and writing manuscripts. The author would express his gratitude to Mr. Tadashi Saito at Power Devices Development Division in Sumitomo Electric Industries for his his continuous guidance and encouragement. The author is very much obliged to Mr. Hiroshi Inada, Mr. Youichi Nagai (now at Power System R&D Laboratories in Sumitomo Electric Industries), Mr. Hiroki Mori and Mr. Ken-ichi Machinaga at Transmission Devices R&D Laboratories in Sumitomo Electric Industries for their helpful support in characterization and device process, stimulating comments and valuable suggestions. The author thanks Dr. Sundararajan Balasekaran at Transmission Devices R&D Laboratories in Sumitomo Electric Industries for proofreading the manuscript.

The author is very much obliged to Mr. Hiroshi Okada at Advanced Materials R&D Laboratories in Sumitomo Electric Industries for his continuous guidance concerning MBE growth, characterization, and management of the MBE growth system.

The author would like to express his gratitude to Mr. Mitsutaka Tsubokura at Analysis Technology Research Center in Sumitomo Electric Industries for his helpful cooperation in MBE growth and characterization.

The author would like to extend his appreciation to Dr. Katsushi Akita, Dr. Takashi Ishizuka and Mr. Kei Fujii at Semiconductor Technologies R&D Laboratories in Sumitomo Electric Industries for their generous cooperation in characterization and MOVPE-regrowth of InP window layer, and fruitful discussions. The author would like to thank Mr. Nobuhiro Saga at Semiconductor Technologies R&D

Laboratories in Sumitomo Electric Industries for his support and advices concerning MBE technology. The author is also very much indebted to Dr. Takashi Kyono at Semiconductor Technologies R&D Laboratories in Sumitomo Electric Industries for his kind encouragement and helpful advices about writing the manuscript.

The author wishes to express his gratitude to Mr. Akira Sato, Mr. Masakazu Takakumo, Mr. Takashi Okade, Mr. Masashi Yamashita, Mr. Tadashi Sasaki, Mr. Taro Higuchi, Mr. Seiichi Ida, Mr. Takeshi Doi and Mr. Takahiro Ueno at R&D General Planning Unit in Sumitomo Electric Industries for their helpful support of characterization and device process.

The author would like to thank his gratitude to Dr. Haruyoshi Katayama and Mr. Junpei Murooka in Japan Aerospace Exploration Agency (JAXA) for their kind support and fruitful discussion about characterization.

The author expresses his great gratitude to Professor Masaaki Kimata for his valuable discussion about the results of experiments. The author also thanks Mr. Shota Kanno and Ms. Tomoko Takekawa for their kind help with experiments.

Special thanks are also due to Mr. Mao Yoshikawa, Mr. Yasuhiro Yonezawa, Mr. Ryoma Hiraike, Mr. Kentaro Oomae, Mr. Kenta Mitsuyoshi and all the members of Professor Kawamura's laboratory for their kind support in characterization and management of the MBE growth system.

This work was partly supported by the Grant for Practical Application of Industrial Technology of New Energy and Industrial Technology Development Organization (NEDO).

Finally, the author would like to thank my parents, my wife, Mai, and my daughter, Natsuki, for their understanding, support and heartfelt encouragement.

Original articles regarding this thesis

No.	Title	Authors	Journal	Related section
1	MBE growth of thick InGaAsN layers with absorption edge at 1.95μm on InP substrates	K.Miura Y.Nagai Y.Iguchi H.Okada Y.Kawamura	International Conference on Indium Phosphide and Related Materials Conference Proceeding pp.420~423 (Princeton, United States of America, 2006)	Chapter 3
2	Improvement of crystal quality of thick InGaAsN layers grown on InP substrates by adding antimony	K. Miura, Y. Nagai, Y. Iguchi, H. Okada, Y. Kawamura	Journal of Crystal Growth Vol.301-302, pp.575~578 (2007)	Chapter 3
3	MBE growth of thick InGaAsN layers lattice-matched to InP substrates	K.Miura, Y.Nagai, Y.Iguchi, M. Tsubokura, H.Okada, Y.Kawamura	International Conference on Indium Phosphide and Related Materials Conference Proceeding pp.376~379 (Matsue, Japan, 2007)	Chapter 3
4	Optical characterization of InGaAsN layers grown on InP substrates	M. Yoshikawa, K. Miura, Y. Iguchi, Y. Kawamura	Journal of Crystal Growth Vol.311, pp.1745~1747 (2009)	Chapter 3
5	Characterization of InGaAsSbN layers grown on InP by MBE	M. Yoshikawa, K. Miura, Y. Iguchi, Y. Kawamura	Physica Status Solidi C8 No.2 pp.390~392 (2011)	Chapter 3

6	Low dark current SWIR photodiode with InGaAs/GaAsSb type II quantum wells grown on InP substrate	H.Inada, K.Miura, Y.Nagai, M.Tsubokura, A.Moto, Y.Iguchi, Y.Kawamura	International Conference on Indium Phosphide and Related Materials Conference Proceeding pp.149~152 (Newport, United States of America, 2009)	Chapter 4
7	Uncooled SWIR InGaAs/GaAsSb type II quantum wells focal plane array	H.Inada, K.Miura, H.Mori, Y.Nagai, Y.Iguchi, Y.Kawamura	International Society for Optical Engineering Proceeding Vol.7660 pp.76603N-1~7 (Orland, United States of America, 2010)	Chapter 4
8	The growth of high quality GaAsSb and type-II InGaAs/GaAsSb superlattice structure	K.Miura, Y.Iguchi, M. Tsubokura, Y.Kawamura	Journal of Applied Physics (Submitted)	Chapter 4
9	Growth and characterization of strain-compensated InGaAs/GaAsSb type II multiple quantum wells on InP	Y. Yonezawa, R. Hiraike, K. Miura, Y. Iguchi, Y. Kawamura	Physica E Vol.42 No.10 pp.2781~2783 (2010)	Chapter 4
10	Type-II InAs/GaSb superlattice grown on InP substrate	K. Miura, Y. Iguchi, Y. Kawamura	Journal of Crystal Growth (Accepted)	Chapter 5